TECHNISCHE
UNIVERSITÄT
WIEN

Diplomarbeit

Three-electrode measurements in solid oxide fuel cell research

zur Erlangung des akademischen Grades

Diplom-Ingenieur

im Rahmen des Studiums

Physikalische Energie- und Messtechnik

eingereicht von

Stefan Reuter
Matrikelnummer 01326528

ausgeführt an der Fakultät für Physik der Technischen Universität Wien
(in Zusammenarbeit mit dem Institut für Chemische Technologien und Analytik
der Fakultät für Technische Chemie)

Betreuung
Betreuer: Univ. Prof. Dr. Jürgen Fleig
Mitwirkung: Projektass. Dr. Andreas Nenning

Wien, 02.02.2020   _____   _____

                              (Unterschrift Verfasser)   (Unterschrift Betreuer)

Abstract

Fuel cells will play a key role in an energy system that does not rely on fossil fuels. Especially solid oxide fuel cells have the ability to convert chemical energy into electricity with very high efficiency. Commercial systems are already available, but research focuses on new materials with superior performance and durability. To investigate the properties of electrode materials, electrochemical impedance spectroscopy can be used. For open-circuit voltage (OCV) testing, measurements are typically conducted on symmetrical two-electrode model cells. However, measuring the impedance of a single porous electrode, while applying a bias voltage to the cell, is only possible with a three-electrode setup. Unfortunately, such measurements are prone to measurement artifacts.

In this thesis, three-electrode measurements were conducted on two different sample geometries ("wing design" and "pedestal design"). Different porous electrodes were characterized at OCV in oxidizing and reducing atmospheres, as well as with applied bias voltage. The measured spectra often contained artifacts, such as inductive features, but meaningful results were obtainable and comparable to defect model calculations nonetheless. High frequency artifacts were identified to result from the coupling capacitance of the reference electrodes measuring line to its shield and were partly compensated by establishing an active shielding. Asymmetric sample configurations (two different electrode materials) yielded more viable results than symmetric configurations, as artifacts originating from the counter electrode were well separated from the main electrode features due to differing characteristic frequencies. Generally, it was shown that best results are obtainable when the electrode resistance of the counter electrode is low and the peak frequencies of working and counter electrode differ by at least two orders of magnitude.

Kurzfassung

Brennstoffzellen werden eine Schlüsselrolle in einem Energiesystem spielen, das nicht von fossilen Brennstoffen abhängig ist. Insbesondere Festoxid-Brennstoffzellen sind in der Lage, chemische Energie mit sehr hohem Wirkungsgrad in Strom umzuwandeln. Kommerzielle Systeme sind bereits verfügbar, die Forschung konzentriert sich jedoch auf neue Materialien mit verbesserter Leistung und Haltbarkeit. Elektrochemische Impedanzspektroskopie kann eingesetzt werden, um die Eigenschaften von Elektrodenmaterialien zu untersuchen. Für Messungen ohne angelegter DC-Spannung (OCV) werden typischerweise symmetrische Modellzellen verwendet. Die Messung der Impedanz einer einzelnen porösen Elektrode mit angelegter Gleichstromspannung ist jedoch nur mit einem Drei - Elektrodenaufbau möglich, der anfällig für Messartefakte ist.

In dieser Arbeit wurden Drei - Elektrodenmessungen an zwei verschiedenen Probengeometrien ("Wing-Design" und "Sockel-Design") durchgeführt. Unterschiedliche poröse Elektroden wurden in oxidierender und reduzierender Atmosphäre sowie mit angelegter Gleichstromspannung charakterisiert. Die gemessenen Spektren enthielten oft Artefakte, wie z.B. induktive Merkmale. Dennoch konnten aussagekräftige Ergebnisse erzielt und mit Defektmodellrechnungen verglichen werden. Hochfrequenz-Artefakte wurden als Folge der Koppelkapazität der Referenzelektroden-Messleitung zu deren Abschirmung identifiziert und durch die Einrichtung einer aktiven Abschirmung teilweise kompensiert. Asymmetrische Probenkonfigurationen (zwei verschiedene Elektrodenmaterialien) lieferten bessere Ergebnisse als symmetrische Konfigurationen, da Artefakte, die von der Gegenelektrode herrührten, aufgrund von unterschiedlichen charakteristischen Frequenzen gut von den Hauptmerkmalen der Elektrode getrennt waren. Generell wurde gezeigt, dass die besten Ergebnisse erzielt werden können, wenn der Elektrodenwiderstand der Gegenelektrode niedrig ist und sich die Maximalfrequenzen von Arbeits- und Gegenelektrode um mindestens zwei Größenordnungen unterscheiden.

Contents

1 Introduction

The world is in the midst of a global climate crisis provoked by the abundantly anthropogenic emission of green house gases. As a consequence, the atmosphere heats up with increasing speed: the last five years were the hottest years ever recorded [1]. To tackle this situation, CO_2 emissions need to be reduced drastically. Renewable energy production plays a crucial role in this initiative. With an increasing amount of volatile power production, such as wind or solar, the capacity for storage of electricity needs to be enlarged. The combination of Solid Oxide Fuel and Electrolysis Cells (SOFC/SOEC) is a suitable option for the build up of large storage capacities in form of hydrogen that can be transformed into electricity with high efficiency [2].

Contrary to other forms of power generation, where multiple transformation steps are needed, fuel cells convert the chemical energy of the fuel directly into electrical energy. As a consequence, a very high efficiency of up to 60% [3] is possible which can be further increased when using the exhaust gases as a heat source for other processes or in a combined heat and power application.

Different types of fuel cells are available which are distinguished by the used electrolyte. SOFCs rely on a solid oxygen ion conducting electrolyte and have multiple advantages over other types due to the high operation temperature of 600 to 1000°C. They have no need for costly catalysts and offer a broad fuel flexibility. However, the high temperatures also impose problems such as fast degradation, long start-up time and complex fabrication processes [4].

State-of-the-art SOFCs use yttria-stabilized zirconia (YSZ) as electrolytes. For cathodes, a composite of YSZ with electronic conducting Sr-doped $LaMnO_3$ is the most used electrode material, whereas a ceramic-metal composite (cermet) of Ni and YSZ is the typical electrode material for anodes [5]. These materials, however, have some severe disadvantages. Ni/YSZ is prone to degradation due to Ni coarsening [6], has poor tolerance for sulfur impurities in the fuel [7] and limited redox-cycling stability [8]. LSM on the other hand has poor oxygen ion conductivity [9]. As a consequence, research is focused on different electrode materials, such as $(La,Sr)(Co,Fe)O_3$ [10] [11] [12] [13] or doped ceria [14] [15] [16].

To investigate the performance of electrodes, electrochemical impedance spectroscopy is the commonly used measurement technique. These measurements are usually conducted on samples consisting of two electrodes, referred to as working electrode (WE) and counter electrode (CE). The measured impedance corresponds

1

to a superposition of the processes taking place at both electrodes and the electrolyte. If the electrode processes have similar time constants, it is not possible to separate the impedance responses from WE and CE. A simple way to overcome this problem is to measure symmetrical samples with identical WE and CE and to attribute half of the measured impedance to one electrode. However, when measured with applied DC bias voltage the WE and CE are affected differently, resulting in different time constants of the nominally identical electrodes. A more practicable way of measuring only one electrode is the use of microelectrodes. By combining a very small WE with a considerably larger CE, the measured impedance is governed by the WE as the impedance of the CE is negligible due to its large area. As this technique is only applicable when measuring thin film electrodes, the only way to measure a half cell spectrum of kinetically fast porous electrodes is by conducting a three-electrode measurement. For that, a reference electrode (RE) is used to separate the potential of WE and CE. The impedance of a half cell (WE plus some of the electrolyte) is obtained by measuring the potential drop between WE and RE and the current between WE and CE. If the equipotential surface sensed by the RE is not influenced by the measurement (current and frequency changes) and located in the electrolyte between WE and CE, the half cell spectrum can be isolated correctly [17]. However, this assumption is often not true. Multiple studies showed that three-electrode measurements are prone to errors arising from capacitive coupling [18] and shifts of the probed equipotential surface with changing frequency caused by geometrical asymmetries or different WE/CE properties [19] [20] [21] [22]. Different cell designs have been proposed and tested [17] [19] [20] [21] [22] [23], a promising setup ("wing geometry") was simulated in Ref. [24].

In this thesis, three-electrode samples with the wing and pedestal design were produced and tested by electrochemical impedance spectroscopy. Samples with symmetric and asymmetric electrode configuration and different porous electrodes were produced. The measurements were conducted in different oxidizing and reducing atmospheres, as well as with applied bias voltage. The main goal was to evaluate the measured spectra and derive recommendations on achieving suitable three-electrode measurements.

2 Theoretical Background

2.1 Basics on fuel cells

Fuel cells are electrochemical devices that convert the chemical energy of the fuel to electricity and heat. In contrast to batteries, fuel cells are open systems that provide electricity continuously, as long as fuel is supplied. All electrochemical cells consist of two main components: the electron conducting electrodes, where the chemical reactions take place, and the ion conducting electrolyte, which spatially separates the electrodes. The typical fuel for fuel cells is hydrogen that reacts with oxygen according to

$$H_2 + \frac{1}{2}O_2 \rightleftharpoons H_2O. \tag{2.1}$$

This reaction is split in two half reactions, the oxidation of hydrogen and the reduction of oxygen. For SOFCs these reactions are:

$$Anode : H_2 + O^{2-} \rightleftharpoons H_2O + 2e^-, \tag{2.2}$$

$$Cathode : \frac{1}{2}O_2 + 2e^- \rightleftharpoons O^{2-}. \tag{2.3}$$
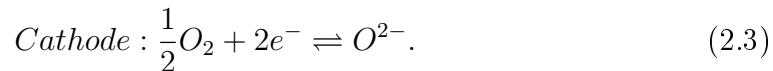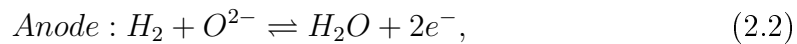
As these reactions occur at different electrodes (hydrogen oxidation at the anode and oxygen reduction at the cathode), the electrons need to be conducted through an external circuit where they deliver electrical power. The ions are conducted by the electrolyte, closing the circuit.

Different kinds of fuel cells differ mainly in operating temperature and ionic charge carrier. In SOFCs, the electrolyte needs to conduct oxygen ions, whereas in polymer electrolyte membrane fuel cells the ionic charge carriers are protons [5].

2.1.1 Thermodynamics

The defining thermodynamic potential of (electro-)chemical reactions with constant temperature and pressure is the Gibbs free energy G. The change of the Gibbs free energy of reaction Δ_rG determines, if a reaction proceeds spontaneously (Δ_rG < 0) or needs the input of work in order to proceed (Δ_rG > 0). The Gibbs free energy of reaction is calculated according to the following equation [4]:

$$\Delta_r G = \sum_{products} G_i - \sum_{educts} G_i. \tag{2.4}$$

It is directly linked to the theoretical cell voltage E (without considering any losses) of electrochemical cells by

$$E = \frac{-\Delta_r G}{zF} \tag{2.5}$$

with z denoting the number of electrons transferred and F denoting the Faraday constant. At standard conditions (25°C, atmospheric pressure) the theoretical cell voltage of a fuel cell that is operated with H_2 as fuel is 1.23 V [5].

Chemical potential and Nernst equation

The Gibbs free energy depends on three independent variables: temperature, pressure and number of atoms of each species. In the case of constant temperature and pressure, G can be written as

$$G = G(n_j) \Rightarrow dG = \sum_i \left(\frac{\partial G}{\partial n_i}\right)_{(T,p)} dn_i \tag{2.6}$$

$$\mu_i = \left(\frac{\partial G}{\partial n_i}\right)_{(T,p)} \tag{2.7}$$

with n_i denoting the number of atoms of species i and μ_i denoting the chemical potential of species i. The chemical potential defines, how the Gibbs free energy changes with infinitesimal variations of each species. It is associated with the activity a through:

$$\mu_i = \mu_i^0 + RT \, ln a_i \tag{2.8}$$

where μ_i^0 is the chemical potential at standard conditions, R the universal gas constant and T the temperature. If one combines Equation 2.6 with Equation 2.8 and considers a chemical reaction with stoichiometric coefficients ν_i, the change of the Gibbs free energy of reaction can be written as:

$$\Delta_r G = \sum_{products} \mu_i^0 \nu_i - \sum_{educts} \mu_j^0 \nu_j + RT \, ln \frac{\prod_{products} a_i^{\nu_i}}{\prod_{educts} a_j^{\nu_j}}$$

$$= \Delta_r G^0 + RT \, ln \frac{\prod_{products} a_i^{\nu_i}}{\prod_{educts} a_j^{\nu_j}} \tag{2.9}$$

where $\Delta_r G^0$ is the Gibbs free energy of reaction at standard conditions. Equation 2.9 describes how the activity (i.e. partial pressure or concentration) of the products and educts influences Δ_rG. By combining Equation 2.5 with Equation 2.9, one obtains the *Nernst equation*:

$$E = E^0 - \frac{RT}{zF} \, ln \frac{\prod_{products} a_i^{\nu_i}}{\prod_{educts} a_j^{\nu_j}} \tag{2.10}$$

where E^0 denotes the standard cell voltage. With the Nernst equation it is possible to calculate the theoretical cell voltage with changing partial pressures of the reacting species, making it the fundamental equation of fuel cell thermodynamics [4] [5].

2.1.2 Reaction kinetics

Even if a reaction is thermodynamically favorable, reaction rates are limited. The reason for this is an energy barrier (activation energy E_a) in the reaction path that needs to be overcome to trigger the reaction. The reaction rates are defined by the Arrhenius equation [25]

$$k = A\, e^{\frac{-E_a}{k_b T}} \tag{2.11}$$

where k denotes the reaction constant, A the pre-exponential factor and k_b the Boltzmann constant. Increasing the temperature leads to an increased reaction constant and therefore a higher reaction rate.

Even simple reactions (for example the reduction of oxygen) can consist of multiple basic steps that each have their own reaction rates. In that case the overall reaction rate is determined by the slowest step (rate-determining step, RDS). For example, in case of low oxygen partial pressure, the RDS might be the gas diffusion of oxygen to the electrode.

As electrochemical reactions always imply an exchange of charge, the involved current is directly linked to the reaction rate. At equilibrium, the forward reaction rate is identical to the reverse reaction rate, resulting in a net current of zero. To force the reaction in one direction, additional energy needs to be applied. As the reaction involves charged species, their free energy is sensitive to voltage changes. Therefore, by adapting the cell voltage, it is possible to shift the reaction in the forward direction and generate a net current. The difference between the theoretical cell voltage and the actual cell voltage associated with a net current is called overpotential η. For charge transfer reactions, the overpotential is linked to the current density j of the reaction by the Butler-Volmer equation

$$j = j_0 \left(e^{\frac{\alpha z F \eta}{RT}} - e^{\frac{-(1-\alpha) z F \eta}{RT}} \right) \tag{2.12}$$

where j_0 denotes the exchange current density (i.e. current density of forward and reverse reaction at equilibrium), α a charge transfer coefficient depending on the symmetry of the activation barrier and z the number of transferred electrons. Equation 2.12 is only valid, if mass transfer to and from the electrode is quick, resulting in reactant and product concentrations that are independent of the reaction rate. In that case, the RDS of the reaction is the electron charge transfer at the electrode. Figure 2.1 shows a plot of Equation 2.12. One can see the linear regime

for small overpotentials, which is used to perform impedance spectroscopy (see section 2.3). Notably, the Butler-Volmer equation was derived for reactions where a charge passes through the electrode-electrolyte interface. For surface kinetics of SOFCs, however, all charged species are in the oxide phase, and the development of kinetic models is a current topic of research [5] [25] [26].
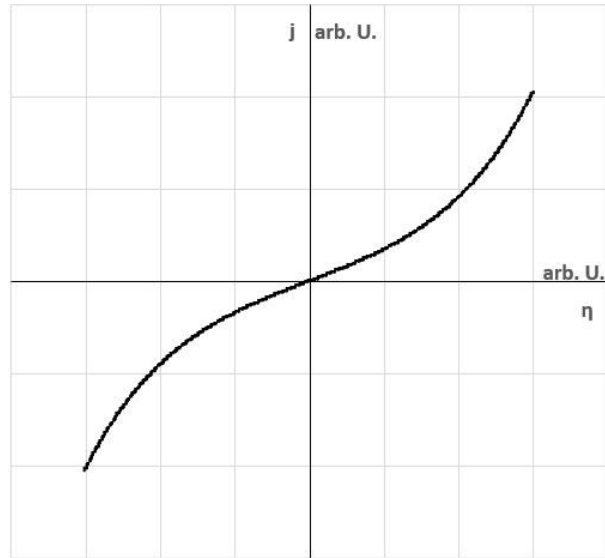

Figure 2.1: Plot of Bulter-Volmer equation with arbitrary units

2.1.3 Oxygen incorporation - Oxygen exchange reaction

The oxygen exchange reaction is fundamental for SOFCs and describes the exchange of oxygen between the crystal lattice and the gas phase. It can be written in Kröger-Vink notation as

$$\frac{1}{2}O_2 + 2e^{'} + V_O^{\bullet\bullet} \rightleftharpoons O_O^{\times}. \tag{2.13}$$

As Equation 2.13 contains electrons, oxygen ions and oxygen in the gas phase, it can only occur at active sites, where electrode, electrolyte and gas phase coincide. These are the so called triple-phase boundaries (TPB). Increasing the length of the TPB, for example by applying a porous electrode, leads to faster kinetics. If the electrode material itself is an ion conductor, the active area is increased to most parts of the electrode surface. These materials are called mixed ionic-electronic conductors (MIEC) and are promising candidates for SOFC cathodes [27].

6

2.2 Electrode materials

The electrodes of a SOFC have to have several properties. They need compatibility to other cell components, long-time stability, sufficient oxygen ion conductivity, high electronic conductivity, good catalytic behavior for fuel oxidation (anodes) or oxygen reduction (cathodes) and allow transport of gases to and from the reaction sites. The commercial standard materials currently used are ceramic-metal composites (cermet) of Ni and yttria-stabilized zirconia (YSZ) as anodes and a composite of YSZ and Sr-doped $LaMnO_3$ (LSM) oxides as cathodes. However, these materials are not without disadvantages. Ni cermet anodes have poor redox stability, low sulfur tolerance and limited fuel flexibility (only H_2 and CO). LSM cathodes show poor ion conductivity and limited catalytic behavior for oxygen reduction at intermediate temperatures. As a reason, research is conducted on other materials that allow increased performance and stability. [27] [28]

The following sections will briefly describe the different electrode materials that were investigated in the course of this thesis.

2.2.1 $La_{0.6}Sr_{0.4}FeO_{3-\delta}$ (LSF)

LSF is an oxide that crystallizes in the perovskite structure ABO_3. It can be seen as a solid solution of $LaFeO_3$ and $SrFeO_3$. The A-site is occupied by either La with a fixed valence of $+3$ or Sr with a fixed valence of $+2$. As the B-site is occupied by Fe^{3+}, there is a lack of positive charge. The inbalance of charge can either be compensated by the partial oxidation of Fe^{3+} to Fe^{4+} or the formation of oxygen vacancies in the lattice. This is expressed by the charge neutrality equation written in Kröger-Vink notation as [29]

$$[Sr'_{La}] + [Fe'_{Fe}] = [Fe^{\bullet}_{Fe}] + 2[V^{\bullet\bullet}_O] \tag{2.14}$$

The defect equilibrium between oxygen in the lattice $O^{\times}_O$ and the gas phase is described by

$$\frac{1}{2}O_2 + 2Fe^{\times}_{Fe} + V^{\bullet\bullet}_O \rightleftharpoons O^{\times}_O + 2Fe^{\bullet}_{Fe}. \tag{2.15}$$
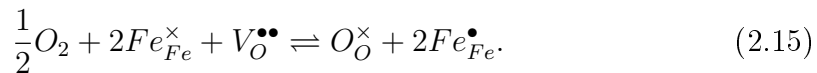
In oxidizing conditions (high oxygen partial pressure), the equilibrium of the oxygen exchange reaction (Equation 2.15) is shifted towards the right side. Therefore, the concentration of oxygen vacancies decreases, resulting in lower ionic conductivity. The electronic conductivity is in that case dominated by electron holes ($Fe^{\bullet}_{Fe}$) and the material becomes p-type conducting. Reducing conditions (lower oxygen partial pressure) shift the equilibrium of Equation 2.15 to the left side, leading to an increase in oxygen vacancies and higher ionic conductivity. Concurrently, the concentration of electron holes is decreased. However, reducing conditions also

imply a partial reduction of iron to Fe^{2+}, leading to an increase of electrons ($Fe^{'}_{Fe}$) as electronic charge carrier (n-type conduction). Electrons and electron holes are coupled by the disproportionation reaction of iron:

$$2Fe^{\times}_{Fe} \rightleftharpoons Fe^{\bullet}_{Fe} + Fe^{'}_{Fe}. \tag{2.16}$$
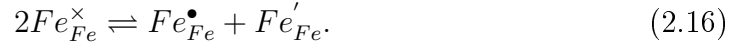
According to the defect model presented in [29], the concentrations of the charge carriers (electrons, holes and oxygen vacancies) depending on the oxygen partial pressure can be calculated with the corresponding equilibrium constants of Equation 2.15 and Equation 2.16, considering charge neutrality (Equation 2.14) and the balance of oxygen and iron sites in the lattice. Figure 2.2 depicts the resulting Brouwer diagram for LSF [10] [11] [13] [29] [30].
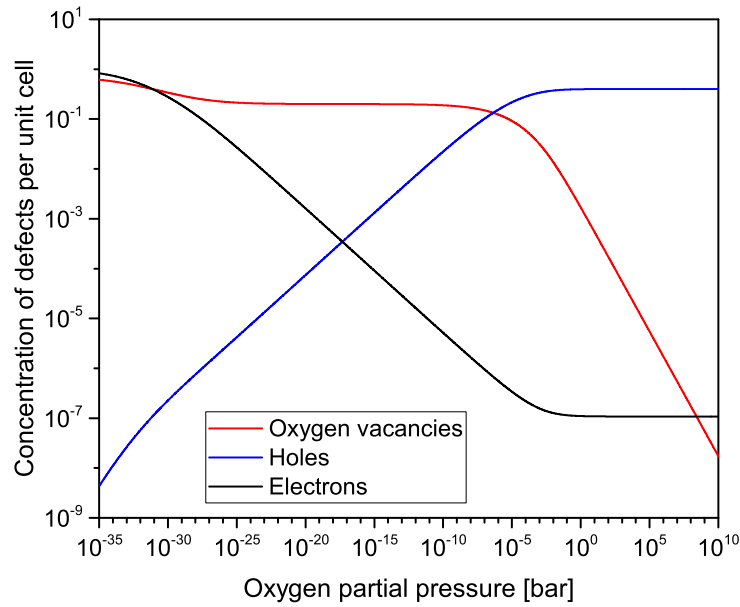

Figure 2.2: Brouwer diagram of LSF at 600°C, calculated with data from [29]

Chemical capacitance

The chemical capacitance is a property of MIECs, such as LSF, that undergo changes in their stoichiometry. It depends on the concentration of ionic (oxygen vacancies) and electronic (electrons or holes) charge carriers and is defined by the minority charge carrier. As the concentrations of the charge carriers are linked with

the electrochemical potential of oxygen, the chemical capacitance is influenced by changes in the oxygen partial pressure as well as the bias voltage.

Assuming ideal solution behavior and the presence of only one dominant electronic charge carrier, the chemical capacitance per volume is given by [31] [32]

$$C_{chem} = \frac{e^2}{k_b T} \left(\frac{1}{4c_{ion}} + \frac{1}{c_{eon}} \right)^{-1} \tag{2.17}$$

where e, k_b and T have their typical meaning (electron charge, Boltzmann constant and temperature, respectively); c_{ion} and c_{eon} denote the ionic and electronic defect concentrations, respectively.

2.2.2 Gadolinia-doped ceria (GDC)

Ceria (CeO_2) is an oxide with fluorite structure. Partly replacing Ce^{4+} with trivalent gadolinia ions leads to the formation of oxygen vacancies:

$$Gd_2O_3 + 2Ce_{Ce}^{\times} + O_O^{\times} \longrightarrow 2Gd_{Ce}^{'} + V_O^{\bullet\bullet} + 2CeO_2. \tag{2.18}$$
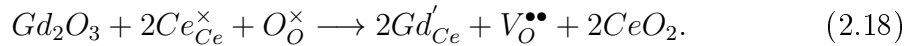
Thus, GDC is a good ion conductor. At very high temperatures and/or in reducing atmospheres Ce^{4+} is partly reduced to Ce^{3+}, leading to an increase in electronic charge carriers:

$$2Ce_{Ce}^{\times} + O_O^{\times} \rightleftharpoons V_O^{\bullet\bullet} + 2Ce_{Ce}^{'} + \frac{1}{2}O_2. \tag{2.19}$$
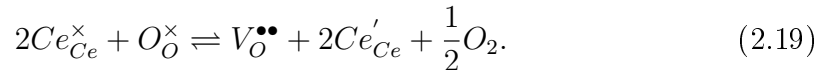
Therefore, GDC is a MIEC in reducing atmospheres and can possibly be used as SOFC anode material [14] [15] [28].

2.2.3 Cermet electrodes

The most commonly used anode material is a porous cermet of Ni and YSZ. The metal provides catalytic activity for hydrogen oxidation and electronic conductivity, the oxide provides ionic conductivity and prohibits the conglomeration of Ni particles. In contrast to the MIEC presented in the previous sections, the active areas of cermet electrodes are limited to the TPB. Therefore, the percolation of metal and the electrolyte phase within the porous electrode is essential for the preferable polarization of the whole electrode resulting in fast kinetics. Apart from YSZ, other ion conducting phases can be combined with nickel, for example doped ceria. A major disadvantage of Ni cermet anodes poses the redox stability (oxidation of Ni to NiO) which is associated with a volume expansion that can potentially damage the cell.

Another widely used electrode material is Pt/YSZ. In contrast to nickel, platinum is stable in oxidizing conditions and can be used as a catalyst for the oxygen exchange reaction. Therefore, it is commonly used as an electrode material in oxygen sensors [27] [28] [33] [34].

2.3 Impedance spectroscopy

Impedance spectroscopy is a powerful and well established measurement technique used in different areas of material research. It is based on a simple electrical and non-destructive measurement. Considering electrochemical systems, electrochemical impedance spectroscopy (EIS) allows the measurement of key processes, such as charge transport or reaction kinetics [35].

2.3.1 Basics

The principle of impedance spectroscopy is to measure the response of a system to a defined excitation over a wide frequency range. A single frequency sinusoidal AC signal (voltage or current) applied to a electrical system evokes a specific response (current or voltage) with the same frequency but a possible phase shift:

$$I(t) = I_0 \; sin(\omega t) \tag{2.20}$$

$$U(t) = U_0 \; sin(\omega t + \varphi) \tag{2.21}$$

Values with the index 0 are the amplitudes of the respective quantities, φ is the phase shift between voltage and current and ω the angular frequency. The impedance of the system is the ratio of voltage and current and can be written with the use of Euler's formula as

$$Z = \frac{U(t)}{I(t)} = \frac{U_0 \; sin(\omega t * \varphi)}{I_0 \; sin(\omega t)} = Z_0 \; e^{j\varphi(\omega)} \tag{2.22}$$

with Z denoting the complex impedance and j the imaginary unit. The real part Z' of the impedance is given by $Z_0 \; cos(\varphi)$ and the imaginary part Z" by $Z_0 \; sin(\varphi)$. A purely resistive system yields a real impedance with a phase shift of zero. Introducing capacitive or inductive elements results in a phase shift between voltage and current and therefore a complex impedance.

Impedance measurements are either executed in 2-point or 4-point configurations. With the 2-point measurement, only two cables are used for applying a current and measuring the corresponding voltage. Therefore, the impedance of the cables is always included in the signal. Using four cables (two for applying and measuring the current and two for sensing the voltage) allows more accurate measurements as the impedance of the cables is not included in the signal [35] [36] [37].

2.3.2 DC bias measurement

Normally, EIS measurements are performed with small AC signals to stay in the linear regime of the current–voltage characteristic, see Figure 2.1. Thus, only small

deviations from the equilibrium arise for the respective electrochemical reactions. By superimposing a DC bias voltage on the sample, the equilibrium of the reactions is shifted, resulting in a non-zero average reaction rate and a corresponding DC current. Therefore, the sample can be measured at different points in the current-voltage characteristic.

When applying bias to a sample, the oxygen partial pressure in the electrode, which defines defect equilibria and the oxygen vacancy concentration, is not identical to the gas phase any more. Therefore, parameters as ionic conductivity (through oxygen vacancy concentration) and electronic conductivity (through electronic defects) change. The oxygen partial pressure in the electrode can be calculated by introducing the chemical potential of oxygen in the electrode, which is defined by the electrochemical potentials of oxygen ions and electrons:

$$\mu_{O_2} = 2\tilde{\mu}_{O^{2-}} - 4\tilde{\mu}_{e^-}. \tag{2.23}$$

Applying a bias voltage U_{DC} changes the electrochemical potential of electrons between the electrodes:

$$\Delta\tilde{\mu}_{e^-} = -FU_{DC}. \tag{2.24}$$

The electrolyte has finite ionic conductivity, resulting in a difference in the electrochemical potential of oxygen ions between the electrodes:

$$\Delta\tilde{\mu}_{O^{2-}} = -2FIR_{electrolyte} = -2F\eta_{electrolyte} \tag{2.25}$$

with $R_{electrolyte}$ denoting the ionic transport resistance of the electrolyte and $\eta_{electrolyte}$ denoting the corresponding voltage drop of the electrolyte. If the counter electrode is either much larger than the working electrode or has considerably faster kinetics, it is not affected by the applied voltage and still in equilibrium with the atmosphere. Therefore, the chemical potential of oxygen of the counter electrode is identical to the atmosphere. Combining Equation 2.23 –Equation 2.25 results in

$$\Delta\mu_{O_2} = \mu_{O_2}^{WE} - \mu_{O_2}^{atm} = 2\Delta\tilde{\mu}_{O^{2-}} - 4\Delta\tilde{\mu}_{e^-} = 4F(U_{DC} - \eta_{electrolyte}) = 4F\eta \tag{2.26}$$

where η is the overpotential at the electrode, WE denotes the working electrode (the polarized electrode) and atm the atmosphere. The chemical potential of oxygen of the working electrode can also be related to the chemical potential of oxygen of the atmosphere and the ratio of the corresponding oxygen partial pressures, according to Equation 2.27. Combining Equation 2.27 with Equation 2.26, one yields an expression for the oxygen partial pressure of the electrode depending on the applied overpotential (Equation 2.28).

$$\Delta\mu_{O_2}^{WE} = \mu_{O_2}^{atm} + RTln\left(\frac{p_{O_2}^{WE}}{p_{O_2}^{atm}}\right) \tag{2.27}$$

$$p_{O_2}^{WE} = p_{O_2}^{atm}e^{\frac{4F\eta}{RT}} \tag{2.28}$$

As the properties of the electrodes change with bias, so does their impedance. This leads to problems when measuring a symmetrical cell, as the two electrodes are affected differently by the applied bias, resulting in complex impedance spectra that cannot be easily interpreted. The issue can be overcome by the three-electrode setup through placing a reference electrode between the working and counter electrode and measuring the voltage drop between either of the main electrodes and the reference electrode. That allows the sensing of a single electrode spectrum and measuring the influence of applied DC bias correctly [31] [38].

2.3.3 Equivalent circuits

Different phenomena in electrochemical cells evoke the impedance of the sample and are represented in the impedance spectrum. Finite electronic or ionic conduction as well as the reaction rate of electrochemical reactions cause resistive behavior. Apart from that, electrochemical cells often show interfacial resistances and capacitances. The changing of the stoichiometry of a material with the applied probing voltage also evokes a capacitance, the so called chemical capacitance.

To extract meaningful information from the impedance spectra, the data is fitted with equivalent circuits where the components are chosen in respect to physical processes. These circuits mainly consist of resistors, capacitors and inductances. However, samples often do not behave ideally (especially capacitances), resulting in the need for non-ideal circuit elements to obtain a satisfying fit. A non-ideal capacitance is fitted with a constant phase element (CPE). Its impedance is given by

$$Z = \frac{1}{T \ (j * \omega)^P} \tag{2.29}$$

with T and P being frequency independent CPE parameters. T resembles the capacitance and P quantifies the non-ideality [35].

R||CPE elements

An electrochemical cell is a series circuit of working electrode, electrolyte and counter electrode. The electrolyte typically causes a purely ohmic impedance, whereas the electrodes can often be described with a parallel connection of a resistance (reaction resistance, polarization resistance, etc.) and a CPE (chemical capacitance, etc.). If the electrodes are not identical or multiple phenomena influence the impedance, more than one R||CPE element is needed to describe the behavior of the cell. Each R||CPE element has an associated time constant $\tau = R * C$ which defines the frequency $f_{max} = 1/(2\pi\tau)$ where the imaginary part of the impedance reaches a maximum [35].

Plotting the imaginary part of the impedance over the real part (Nyquist plot) results in more or less depressed semicircles for each R||CPE element. Figure 2.3 depicts a Nyquist plot of the impedance of a resistor in series with an R||CPE element. The spectrum of an ideal R||C element is also included in the figure for comparison.

The T parameter of a CPE does not correspond to an actual capacitance value. However, it is possible to calculate an effective capacitance of a CPE parallel to a resistor R by [39]:

$$C = (TR^{1-P})^{1/P} \tag{2.30}$$

(a) Nyquist plot   (b) Associated circuits
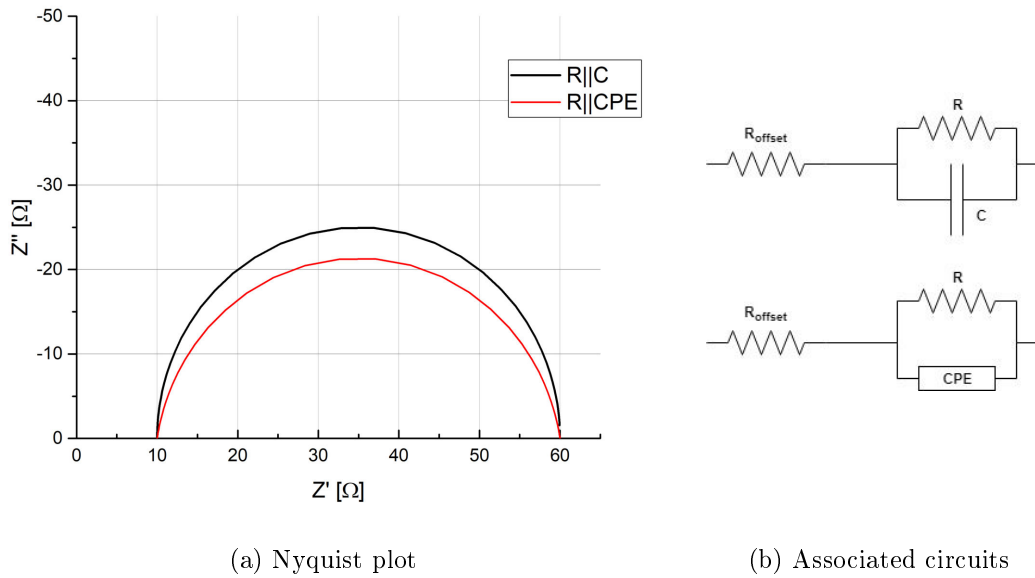
Figure 2.3: Inset (a) depicts the Nyquist plot of an R||C and an R||CPE element. The corresponding circuits are presented in inset (b). The values of used circuit elements are: $R_{\text{offset}} = 10$ Ω, R = 50 Ω, C = 1 mF, T = 0.001 and P = 0.9.

Transmission line model

Transmission line equivalent circuits are widely used to fit the impedance spectra of mixed conducting electrodes. As such models are not only valid for electrodes that consist of one mixed conducting material, but also for electrodes consisting of two phases (one for ionic and one for electronic conduction), they can be applied to many electrochemical systems. Figure 2.4a depicts the circuit of a general

transmission line. It consists of an ionic rail and an electronic rail that are connected via the reaction resistance and the chemical capacitance, as these processes convert ionic charge to electronic charge and vice versa. Current coming from the electrolyte is transported on the ionic rail and is fully converted to electronic current when it reaches the current collector. The involved parameters are the ionic transport resistance R_{ion}, the electronic transport resistance R_{eon}, the reaction resistance R_{react} and the chemical capacitance C_{chem}. In case of high electronic conductivity within the electrode, the electronic rail is short-circuited (R_{eon}=0) leading to an impedance of the transmission line circuit given by

$$Z = \lambda \ R_{ion} \ coth \left(\frac{L}{\lambda} \right) \tag{2.31}$$

with

$$\lambda = \sqrt{ \frac{1}{R_{ion} \left(\frac{1}{R_{react}} + j\omega C_{chem} \right)} } \tag{2.32}$$

where L is the thickness of the electrode and λ the electrochemically active length. The area specific resistance of the electrode ($ASR_{electrode}$) can be calculated from Equation 2.31 and Equation 2.32 by setting ω to zero, leading to:

$$ASR_{electrode} = \sqrt{R_{react} * R_{ion}} \ coth \left(L * \sqrt{ \frac{R_{ion}}{R_{react}} } \right) \tag{2.33}$$

The equivalent circuit used for fitting appropriate spectra in the course of this thesis is shown in Figure 2.4b. It includes a resistance for the ionic conduction losses in the electrolyte (R_{YSZ}) and also takes into account possible interfacial effects ($R_{interface}$ and $C_{interface}$) at the electrolyte-electrode interface. Fitting is done with the commercial software "ZView 2" that contains an extended equivalent circuit element respresenting a transmission line model (DX11-Bisquert 2). Within this element, all capacitances are described with CPEs instead of capacitors to account for non-ideal behavior. The equvialent circuit used for fitting in ZView is depicted in Figure 2.5. As this circuit is defined by 14 parameters with unintuitive names, an explanation of each parameter is provided in Table 2.1 [40] [41] [42].

2.3.4 Measurement artifacts with three-electrode measurements

Three-electrode measurements are commonly used when investigating the influence of DC bias on electrodes. However, these measurements are prone to errors leading to artifacts and distorted features in the impedance spectra. Some artifacts can

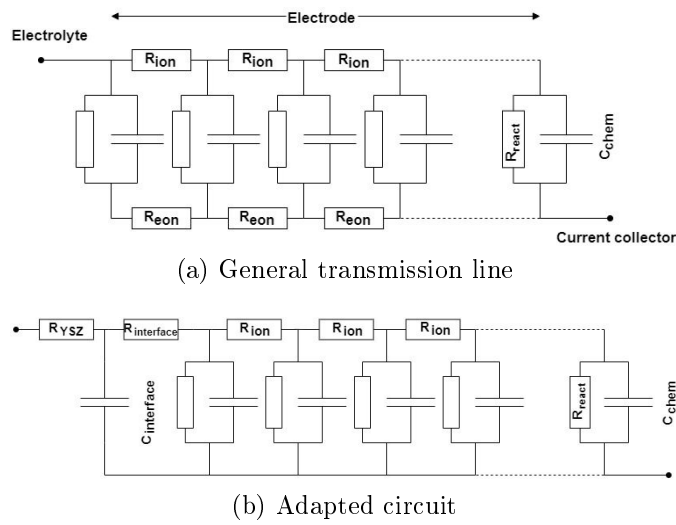(a) General transmission line

(b) Adapted circuit

Figure 2.4: Inset (a) depicts a schematic of a general transmission line equivalent circuit. The adapted circuit used for fitting the spectra of selected samples in the course of this thesis is presented in inset (b).
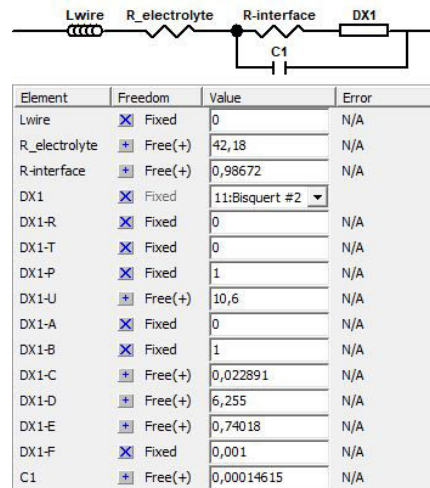

Figure 2.5: Transmission line equivalent circuit and associated parameters in ZView

be prevented with an improved geometry and reference electrode placing, while others even occur with a perfect setup. The main setup used in this thesis were plane-parallel electrodes on a thick electrolyte that had a protrusion on the side where the reference electrode was placed, see subsection 3.1.3. The main artifact sources for this advanced measurement setup are briefly described in the following [24].

15

ZView parameter	Name in equation/Explanation	fixed/free
Lwire	Inductance of wiring	may be fixed to 0
R_electrolyte	R_{YSZ}	free
R-interface	$R_{interface}$	may be fixed to 0
DX1-R	R_{eon}	fixed to 0
DX1-T	Capacitance on electronic rail	fixed to 0
DX1-P	Parameter describing non-ideal behavior of capacitance on electronic rail	fixed to 1
DX1-U	R_{ion}	free
DX1-A	Capacitance on ionic rail	fixed to 0
DX1-B	Parameter describing non-ideal behavior of capacitance on ionic rail	fixed to 1
DX1-C	R_{react}	free
DX1-D	C_{chem}	free
DX1-E	Parameter describing non-ideal behavior of chemical capacitance	free
DX1-F	Electrode thickness in cm	fixed to 0.001
C1	$C_{interface}$	may be fixed to 0

Table 2.1: Explanation of ZView transmission line equivalent circuit parameters

Misaligned working and counter electrodes

If the two electrodes are misaligned, the reference electrode may no longer be able to separate the potential from the working electrode from the rest of the sample. This is the case if the equipotential surface of the reference electrode ends on the counter electrode-electrolyte interface, resulting in parts of the measured impedance originating from the counter electrode (cross contamination). Hence, the features in the spectrum can be distorted and artifacts may arise, which possibly leads to wrong interpretations [20].

Frequency-dependent current distribution

The current distribution through an electrochemical cell changes with the frquency. At high frequencies the electrodes are short-circuited by their capacitances and the impedance of the sample solely arises from the electrolyte. Therefore, the current paths in the electrolyte expand over a wide area to minimize the resistance. At lower frequencies the electrodes also contribute to the impedance, resulting in current paths that are distributed closer underneath the electrode surface. In the

case of perfectly symmetric cells, this transition does not influence the reference potential as it is not shifted with frequency changes. However, when investigating asymmetric samples (misaligned electrodes, different electrode materials, etc.) the transition leads to a shift of the equipotential surface of the reference electrode during the measurement. That results in a measured electrolyte resistance that is frequency-dependent and therefore can again lead to distorted impedance features and (inductive) artifacts [19] [21].

Voltage divider on reference electrode measuring line

An ideal voltmeter has an infinitely high input impedance in order to not influence the measured signal. However, the impedance of a real voltmeter is finite and consists of a big resistor parallel to a small capacitance. This impedance Z_{input} is also influenced by the coupling capacitance of the reference electrode measuring line to its grounded shield. As this capacitance is parallel to the impedance of the voltmeter, it adds up to the effective input capacitance of the voltmeter, lowering the overall effective input impedance Z_{input}^{eff}.
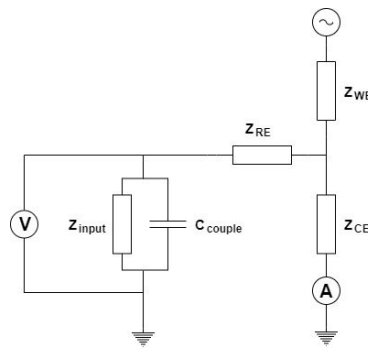
Figure 2.6: Schematic of voltage divider on reference electrode measuring line

The effective input impedance and the impedance of the reference electrode build a voltage divider that influences the measured voltage (Figure 2.6). The deviation of the measured voltage and the real voltage (with infinite effective input impedance) can be calculated with

$$\Delta U_{RE} = Z_{RE} * I_{RE} = \frac{Z_{RE}}{Z_{input}^{eff} + Z_{RE}} * U_{real}. \tag{2.34}$$

If Z_{input}^{eff} is in the same order of magnitude as Z_{RE}, the influence on the measured voltage is substantial. Considering an input capacitance of 10 pF of the voltmeter and a coupling capacitance of the measuring cable of 150 pF (100 pF per meter, 1.5 meter cable length), one can approximately calculate the absolute value of the

input impedance at 1 MHz (neglecting the input resistance) to about 1 kΩ. This value is comparable with typical impedances of reference electrodes used in the course of this thesis, leading to measuring artifacts in the high frequency region of the recorded spectra. By forcing the shield of the BNC cable of the measuring line to the same potential as the core, the coupling capacitance can be canceled out, decreasing the size of the artifacts [24].

3 Experimental

3.1 Sample preparation

In the course of this thesis, thin films as well as porous electrodes were investigated on electrolytes with different geometries. The electrolyte substrates were either YSZ single crystals or polycrystalline YSZ.

3.1.1 Thin films

Dense GDC thin films of about 350 nm thickness were deposited on 5 mm x 5 mm x 0.5 mm YSZ single crystals (9.5 mol% Y_2O_3, Crystec GmbH, Germany) by pulsed laser deposition. The substrates had [100] orientation and were polished on both sides. To ensure homogeneous polarization of the electrodes Pt current collector grids were predeposited on the substrates. Before the deposition of the current collectors the electrolytes were treated with an 1 kV Ar - ion beam for 20 minutes to create some defects for better adhesion of the current collector. Current collectors consisting of a 5 nm thick Ti layer followed by a 100 nm thick Pt layer were deposited on the substrate via Ar sputtering (MED 020 Coating System, BAL-TEC, Germany). The parameters of the sputtering process are given in Table 3.1.

	Titanium	Platinum
target distance	6 cm	6 cm
sputter curent	100 mA	100 mA
sputter time	56	161

Table 3.1: Parameters used for sputtering of current collectors

The current collectors were structured via ion beam etching lithography. A photoresist (N-1430 MicroResist Technology, Germany) was spin-coated (SCC-200 KLM, Germany) at 70 rps for 30 seconds, followed by 150 rpm for 10 seconds. Due to surface tension, the photoresist was thicker at the edges of the substrate. This effect was minimized by the short sequence with high rotational speed. To dry the photoresist, the substrate was put on a hot plate with a temperature of 110°C for two minutes. Afterwards, a mask with the desired pattern (grid with 5

µm strip and 10 µm hole) was aligned on the substrate and the photoresist was exposed to UV light (350W, USHIO 350DP Hg, Ushio, Japan) for 60 seconds. The sample was developed in a liquid developer solution (MicroResist Technology, Germany) for 60 seconds which removed the unexposed photoresist. The etching of the current collectors was done with an Ar ion beam. The remaining photoresist was removed by carefully brushing the electrode with a lint-free cloth soaked in ethanol p.a..

The electrode thin films were then deposited on top of the current collectors. A GDC 10 (10 % Gd_2O_3 doped CeO_2 from Treibacher Industrie AG, Austria) target was prepared by cold isostatic pressing with a pressure of 15 tons and sintering at 1400°C for 10 hours. The ablation was done by a KrF excimer laser (Complex Pro 201F) with a pulse energy of 400 mJ. The distance between the sample and the target was 6.7 cm and the sample was heated to approximately 650°C. The deposition was done in an oxygen atmosphere with a pressure of $4 * 10^{-2}$ mbar. For the desired thickness of 350 nm the laser was operated for 20 minutes with a firing rate of 5 Hz.

3.1.2 Porous electrodes

Porous electrodes were prepared by either screen printing or brushing of electrode paste on the electrolyte substrates (5 mm x 5 mm x 0.5 mm YSZ single crystals or round polycrystalline YSZ with a diameter of 15 mm). The pastes were produced by mixing commercially available electrode powder with an ink vehicle in a one-to-one weight ratio. The mixture was diluted with ethanol p.a. and homogenized in a ball mill (FRITSCH GmbH, Germany) for 30 minutes. In the end, the excess ethanol was evaporated on a hot plate until the paste had a suitable viscosity. Apart from that, also commercially available Pt/YSZ (Tanaka) and NiO/YSZ (Heraeus) pastes were directly used.

After applying the electrode material, the samples were dried at 125°C for several minutes. For materials with insufficient electric conductivity, either platinum paste (Tanaka TR-7907) or NiO (Heraeus) was brushed on the electrode as a current collector. Sintering was done in either a chamber furnace (HST12/300, Carbolite Gero GmbH, Germany) or a tube furnace (RHF 1600, Carbolite Gero GmbH, Germany). The sintering parameters for the different electrode materials are given in Table 3.2.

3.1.3 Three-electrode samples

The substrates used for the three-electrode measurements were 5 mm x 5 mm x 1 mm YSZ single crystals (Crystec GmbH, Germany) that had a protrusion (wing) carved out at one side of the substrate (Figure 3.1). The wing was placed

Electrode material	Temperature [°C]	Duration [h]	Heating / cooling rate [°C/min]
Pt/YSZ	1300	1	5
GDC 10	1150	3	3
LSF	1050	3	3
NiO/YSZ	1350	1	3
NiO/GDC	1150	3	3

Table 3.2: Parameters used for sintering porous electrodes

symmetrically on the front face, with a height of 0.5 mm and a width that varied from 0.4 mm to 0.6 mm, depending on the sample. Porous electrodes were either brushed or screen printed on the sample, as described in subsection 3.1.2. On the wing itself, the electrode material was brushed on with an extremely fine brush. After the subsequent drying, the neck of the wing was carefully cleaned with a lint-free cloth soaked in ethanol p.a..
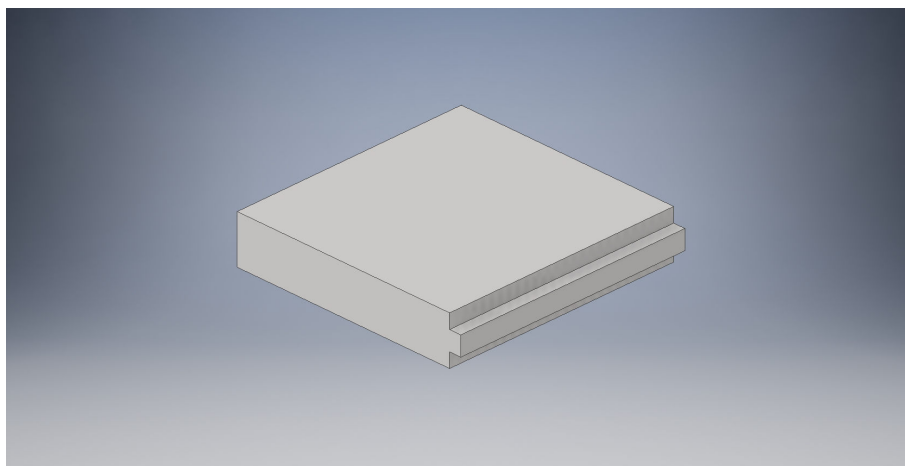
Figure 3.1: Wing sample

Samples with LSF electrodes needed special treatment, as LSF chemically reacts with YSZ during sintering by forming low conductive phases that lead to an increased polarization resistance [12] [43]. This can be prevented by applying a diffusion barrier directly on the YSZ before applying the LSF electrode [44]. These barriers were either dense GDC thin films that were deposited on the substrate by pulsed laser deposition, as described in subsection 3.1.1, or thin layers of porous GDC. As the diffusion barrier was not wanted on the neck of the wing, this part had to be covered with ZrO_2-paste during the deposition. A sketch of the whole preparation process of the three-electrode samples is given in Figure 3.2.

(a)

(b)
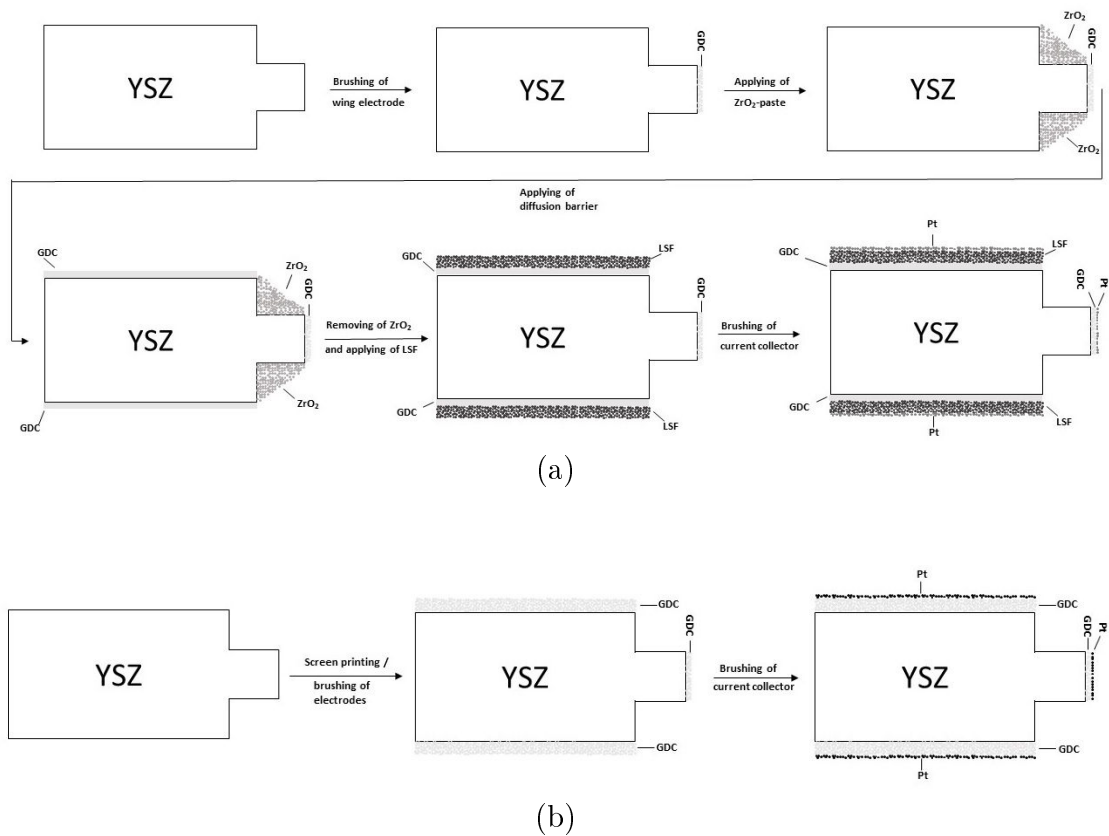
Figure 3.2: Sketches of the preparation of three-electrode samples with diffusion barrier (a) and without (b)

3.2 Experimental setup

The description of the experimental setup only covers the impedance measurements, as these were the main part of this thesis.

3.2.1 Measuring apparatus

The measuring apparatus consists of the sample holder (seen in Figure 3.3) and the measuring instruments.

Sample holder

The sample holder was specially designed for the measurement of three-electrode samples. However, also samples without reference electrode were measured with this sample holder. The tube of the holder is made of alumina and mounted to
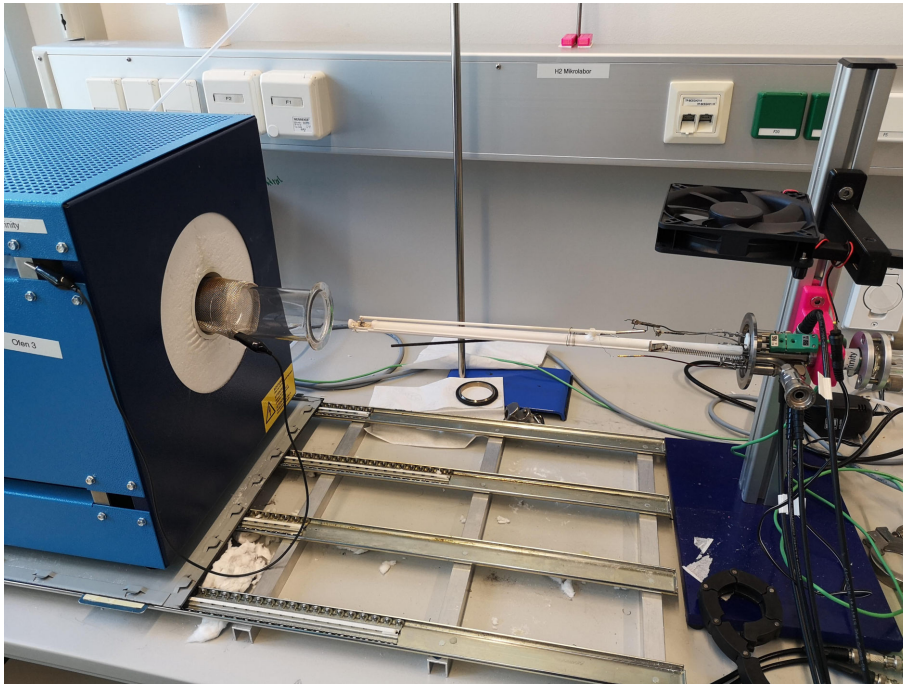
Figure 3.3: Sample holder

a steel flange housing the gas inlet and outlet and the cable connectors. A thermocouple is positioned in close proximity to the samples to accurately measure the temperature. The internal wiring is done completely with Pt-wires. To ensure sufficient gas flow to the electrodes, Pt meshes are used for contacting the electrodes (Figure 3.4). The wing electrode is contacted via a slightly convex bent Pt-wire mounted on an alumina cylinder. The measurements are performed in four-point configuration resulting in one of the main electrodes being contacted with two wires. When measuring samples without a wing, the contact for the wing electrode was placed on the Pt mesh of the electrode which is only contacted via a single wire. Therefore it was possible to perform 4 - point measurements with all samples.

Once the samples were fixed in the holder, the tube furnace was carefully moved over the sample holder and the glass tube was fixed to the flange.

Measuring instruments

Measurements were performed in various gas atmospheres, at different temperature levels and under DC bias. Mass flow controllers (Aera, ROD 4) were used to set and maintain the gas atmospheres. The sample holder was heated with a tube furnace (Carbolite Gero GmbH & Co. KG, Germany), which was controlled by
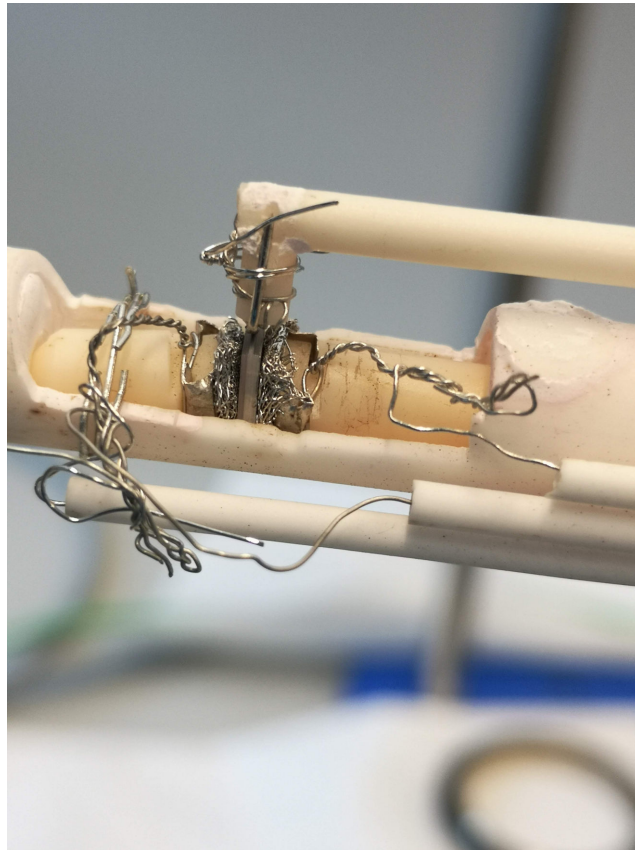
Figure 3.4: Tip of sample holder with mounted three-electrode sample

a temperature controller from Schneider Electric Systems Germany GmbH >EU-ROTHERM<, Germany. The measuring instrument used for impedance spectroscopy was a Novocontrol Alpha-A High Performance Frequency Analyzer. If DC bias was applied to the samples, the Frequency Analyzer was coupled with a Novocontrol electrochemical Test Station POT/GAL 30V/2A.

All instruments were controlled via a PC with the software "Javalab".

3.2.2 Trigger box

With the appropriate wiring of the sample holder and the impedance analyzer, it is possible to measure electrode 1 or electrode 2 against the reference or one electrode against the other (corresponding to a normal cell without reference electrode). As only four wires are connected to the sample, it was not possible to switch between the different measuring modes without rewiring the setup. To overcome this limitation, a trigger box was built that allowed switching between different modes without manual rewiring (Figure 3.5a). The trigger box consists of four

relays connected to a micro controller. That way it is possible to switch the relays with the Javalab software. The wiring of the box is depicted in Figure 3.5b. The four inlet ports are connected to the corresponding connectors of the impedance analyzer. Each inlet port is wired to a relay and therefore has two outlet ports. As only two relays are needed, six outlet ports are wired to the sample holder according to Figure 3.5b.

Figure 3.5 also indicates the connection of the CE port of the impedance analyzer with the WE port of the sample holder and vice versa. The reason for this is of an aesthetic nature. Due to the internal wiring of the impedance analyzer (Figure 3.6), voltage is applied at the CE port and current is measured at the WE port. Therefore, the CE terminal has positive polarity. As the more intuitive approach would be the other way around, the ports of the sample holder were relabeled.

(a) Illustration of different measure modes

(b) Drawing of the trigger box
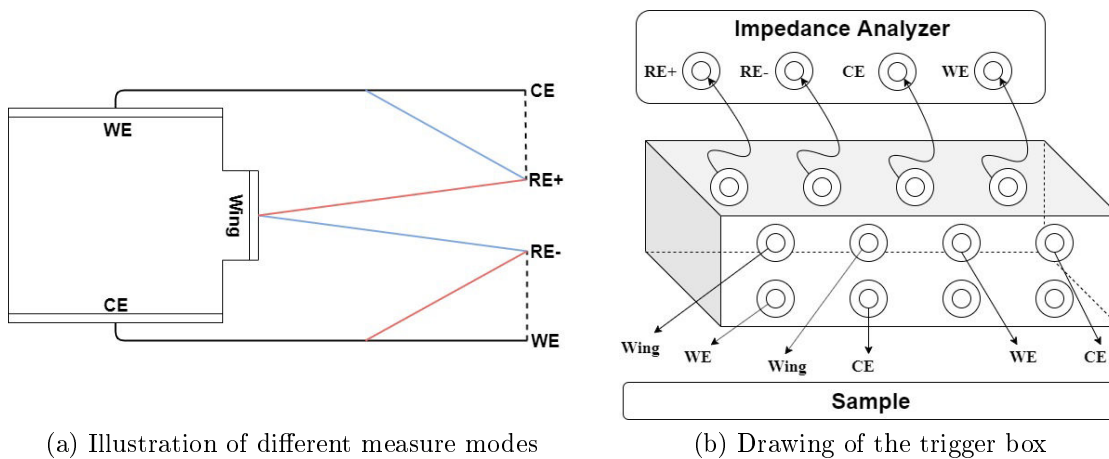
Figure 3.5: Inset (a) visualizes the contacting of the sample for the different measuring modes. The black lines are always connected, the blue lines represent the "WE vs. Wing" mode, the red lines represent the "Wing vs. CE" mode and the dotted lines represent the "WE vs. CE" mode. Inset (b) depicts the trigger box with four inlet ports connected to the impedance analyzer and six of the eight outlet ports connected to the sample.

3.2.3 Measurement procedure

Two-electrode samples

The first measurements were conducted on regular two-electrode samples to test the measurement setup and to identify materials suitable for the three-electrode
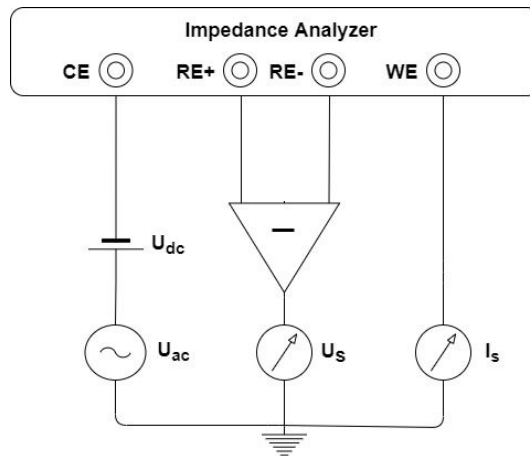
Figure 3.6: Schematic internal wiring of the impedance analyzer. Voltage (AC and possibly DC) is applied to the CE port and the current is measured at the WE port. The voltage drop is measured between the RE+ and the RE- ports.

measurements. The samples were mounted between the platinum meshes, followed by sealing the sample holder with a glass tube, as mentioned in subsection 3.2.1. Before heating up the furnace, the gas atmosphere was set. Measurements were conducted in humidified 2.5% H_2 in Argon or in 1% O_2 in nitrogen. The humidification was achieved by bubbling the gas through distilled water at room temperature, resulting in approx. 25 mbar H_2O in the gas (corresponding to the saturation pressure of water at room temperature [45]).

The measurement temperatures were cycled from 500°C in steps of 50°C to 800°C and back to 500°C. The typical frequency range of the measurement was from 1 MHz to 50 mHz and the applied voltage 20 mV.

Apart from temperature cycles, also cycles with different gas atmospheres were measured. The composition of the atmosphere was changed between a ratio of H_2 to H_2O from 20:1 to a ratio of 1:20. Before starting the next measurement after changing an atmosphere, there was a waiting time of 30 minutes to guarantee a full exchange of the atmospheres.

One sample was also measured under the influence of DC bias. The applied DC voltage was cycled from -300 mV to +300 mV in 50 mV steps.

Three-electrode samples

The three-electrode samples were mounted between the platinum meshes and the reference electrode was carefully contacted. Then the glass tube was placed over the sample holder and the whole apparatus was sealed. The measurements were

26

conducted at 650°C and 750°C in different gas mixtures. Oxidizing atmospheres ranged from 100% O_2 to 0.1% O_2 (remainder nitrogen), reducing atmospheres ranged from a ratio of H_2 to H_2O of 19:1 to 1:9. Bias measurements were performed at a fixed atmosphere with the magnitude of the applied DC voltage depending on the specific sample. Samples with small polarization resistances compared to the electrolyte resistance were measured with higher bias than those with rather high polarization resistances. The maximum applied bias values varied between ± 700 mV and ± 2000 mV.

The frequency range of the measurement was also adapted depending on the specific samples. Most measurements were carried out between 1 MHz and 20 mHz. Due to relatively high characteristic frequencies of some materials, selected measurements only reached down to 500 mHz. The applied measuring voltage was either 20 mV or 100 mV.

3.2.4 Active shielding

As mentioned in subsection 2.3.4, capacitive currents, flowing from the measuring line of the reference electrode through its shield, are a source of high frequency artifacts. To minimize these currents, the capacitive coupling between the signal conductor and its shield has to be reduced. This is done by actively shielding the BNC cable through setting the shield line on the same potential as the measuring line. When assuming a perfectly symmetric cell, the potential drop between the WE and the RE should be the same as the potential drop between RE and CE. This means that the potential of the reference electrode is half of the applied measuring voltage. The active shielding of the RE measuring line could in this case be easily done by a simple voltage divider with two identical resistances between the CE terminal of the impedance analyzer (through which the voltage is applied) and the shield line of the RE BNC cable.

Real samples, however, are not perfectly symmetric, even if the WE and CE are of the same material. Therefore, the potential of the reference electrode is not exactly half of the applied voltage and the active shielding is getting more difficult. To force the shield line on an adaptable potential, the voltage divider between the CE terminal and the shield has to be equipped with potentiometers instead of resistances with fixed values. That way the potential of the shield line can be adapted appropriately.

To ensure a compact measuring apparatus, the two potentiometers were included in the trigger box. Since only two of the relays are needed for cycling through the different measuring modes, one of the remaining two is used as a switch for turning the active shielding on and off. The wiring of the voltage divider is shown in Figure 3.7. As the wing is contacted with two cables (needed for cycling through measuring modes), also two shield lines have to be actively shielded. At the steel

flange, all BNC shields are grounded, which is why the shield lines of the two actively shielded BNC cables have to be interrupted close to the sample holder. Apart from that, all BNC connectors of the impedance analyzer are grounded. As a reason, short cables are used to connect the trigger box with the impedance analyzer. That way the length of not actively shielded wiring is minimized.
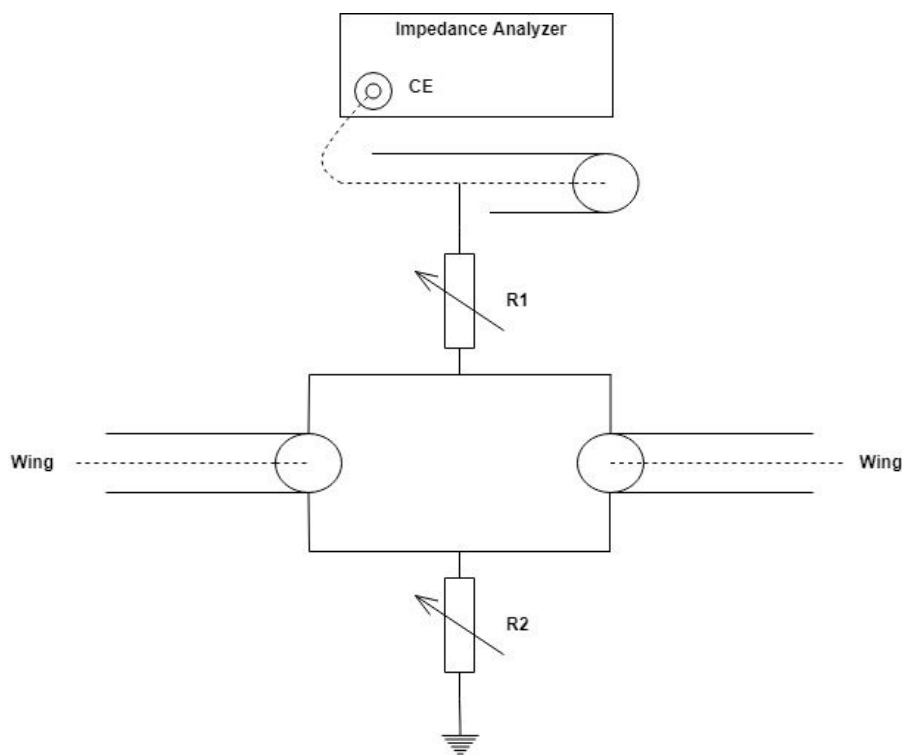

Figure 3.7: Schematics for the active shielding of the RE measuring line. As the measured samples are not perfectly symmetric, the voltage divider is equipped with two potentiometers R1 and R2. Two actively shielded coaxial cables contacting the wing electrode are needed to be able to cycle through different measuring modes.

3.2.5 Low pressure measurements

During the course of this thesis, some measurements were performed in a low pressure measuring setup to decrease the influence of gas diffusion (Figure 3.8). These measurements were conducted in a H_2/H_2O gas mixture at pressure levels below 100 mbar. The mixture is produced by bubbling pure H_2 through distilled water at room temperature.

The samples were inserted in the holder which was sealed by the glass tube and put in a split tube furnace (Carbolite Gero GmbH & Co. KG, Germany). The tube was then evacuated with a membrane pump and purged with 2.5% H_2 in Argon to flush out the remaining oxygen before applying the pure hydrogen. To ensure that no burnable gas mixtures were formed in the pump, gas sucked from the measuring setup was diluted with 2.5% H_2 before reaching the pump. The pressure in the tube was set by a needle valve that controlled the suction capacity. Different gas mixtures were set through a mass flow controller (Aera, ROD 4) controlling the hydrogen flow. The partial pressure of H_2 in the mixtures was calculated after subtracting the H_2O partial pressure (approx. 25 mbar) from the total measured pressure (CTR 100, Oerlikon Leybold Vacuum, Germany). Apart from that, the H_2 partial pressure could also be calculated from the recordings of a lambda sensor (Bosch AG, Germany). The impedance spectra were measured with the same instruments as mentioned in subsection 3.2.1.
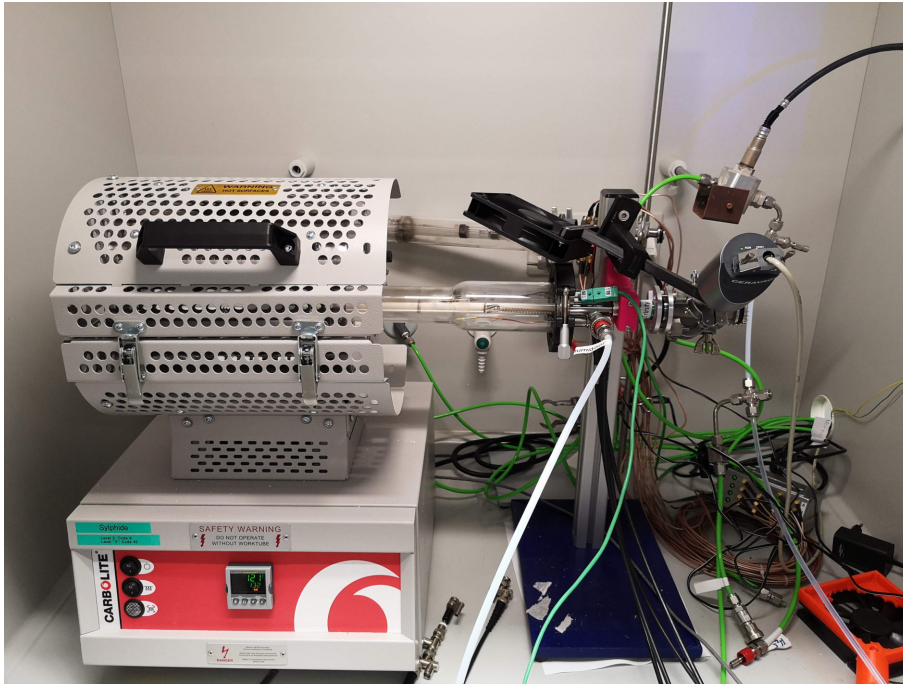
Figure 3.8: Low pressure measurement setup

4 Results

4.1 Measurements on two-electrode samples

To test and verify the measurement setup and to gain reference values, regular two-electrode samples were measured before conducting measurements on three-electrode samples. The investigated samples included porous and thin film electrodes made of different materials.

4.1.1 Porous GDC10

The approximately 12 μm thick porous GDC10 electrodes with a diameter of 10 mm were screen printed on a round polycrystalline YSZ substrate with a diameter of 15 mm. To ensure good electrical contact and complete polarization of the electrodes, Pt paste was brushed on both sides of the sample before sintering at 1150°C for three hours. The impedance measurement was conducted in the low pressure measuring setup at a total pressure of 70 mbar (25 mbar H_2O, remainder H_2) and in the temperature range of 500°C to 800°C. The corresponding spectra are depicted in Figure 4.1. All spectra consisted of an intermediate frequency shoulder and a dominant low frequency semicircle. The two spectra at low temperatures (500°C and 550°C) showed the beginning of a high frequency semicircle, whereas the other spectra showed inductive behavior at high frequencies.

All spectra were fitted with an equivalent circuit consisting of a serial connection of a resistor (accounting for the high frequency offset) and an R‖CPE element. The corresponding values for the area specific resistance and chemical capacitance are presented in Figure 4.2. As expected, the polarization resistance decreased significantly with increasing temperature, reaching a value of 0.18 Ωcm^2 at 800°C.

By plotting the logarithm of the resistance against the inverse temperature, one yields an Arrhenius plot which can be used to obtain the activation energy of the corresponding process (Figure 4.3):

$$R = A \; e^{\frac{E_a}{k_b T}} \longrightarrow log(R) = C + \frac{E_a log(e)}{k_b} \frac{1}{T} \tag{4.1}$$

The calculated activation energy for the electrode process was 0.948 eV.

(a) 500°C to 550°C

(b) 600°C to 650°C

(c) 700°C to 800°C
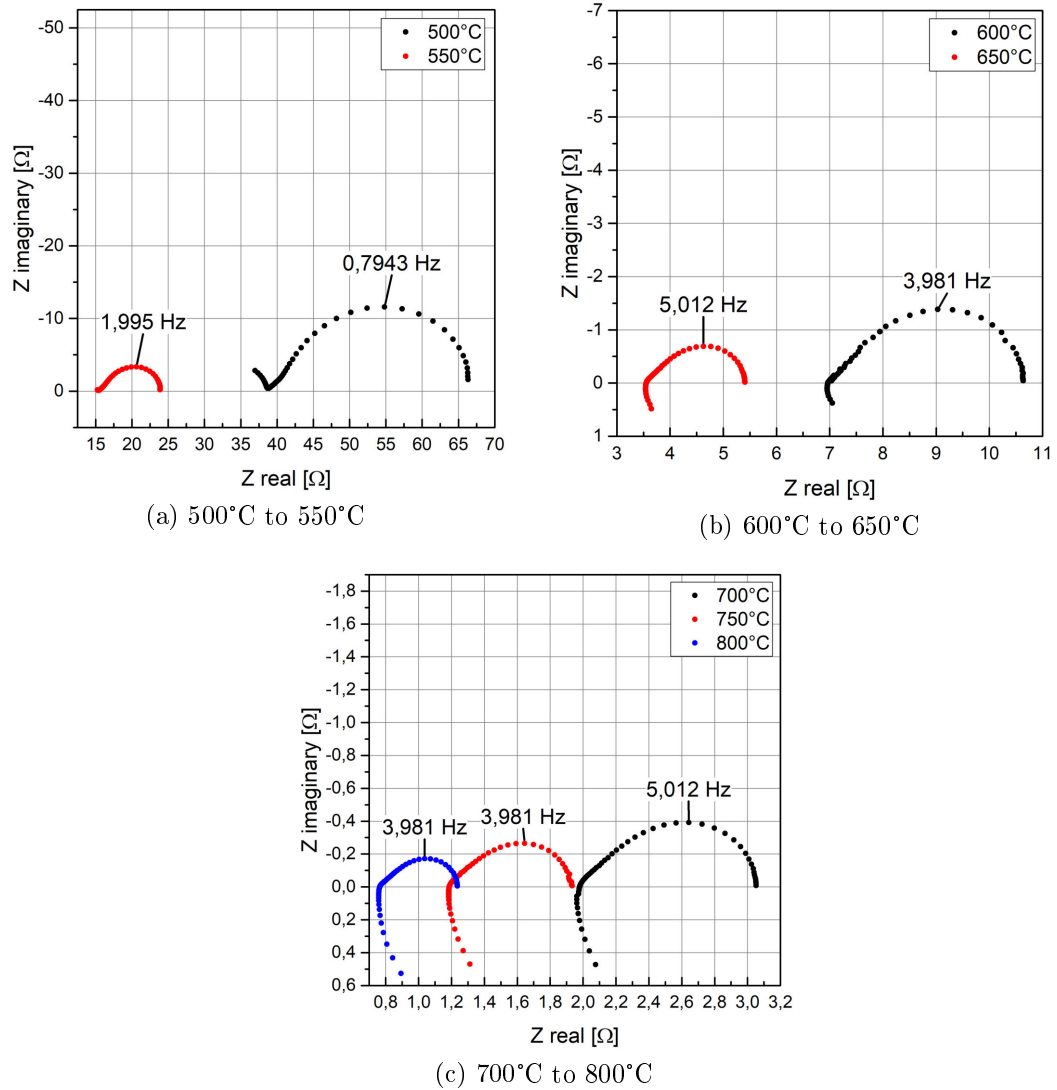
Figure 4.1: Impedance spectra of symmetric porous GDC sample with Pt current collector in 25 mbar H_2O and 45 mbar H_2 at different temperatures. The peak frequency of each spectrum is included in the plots.
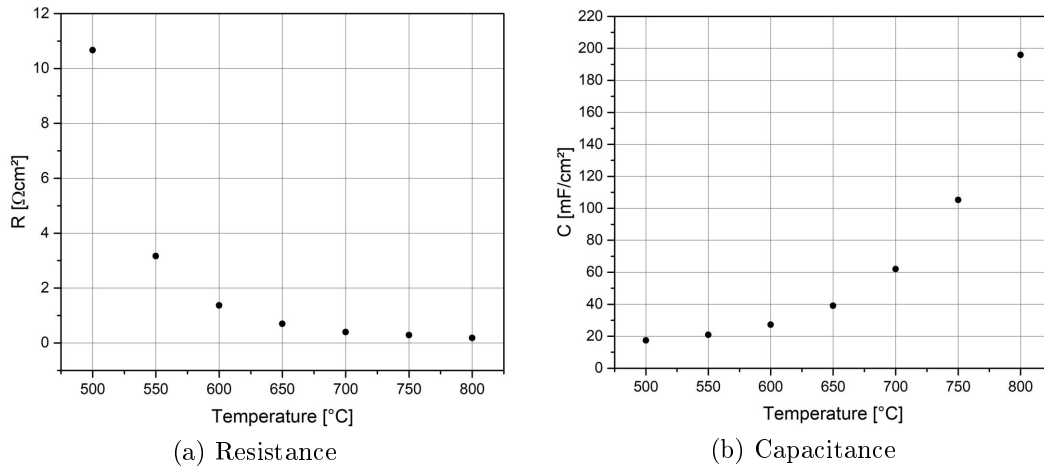
(a) Resistance

(b) Capacitance

Figure 4.2: Resistance and capacitance of one porous GDC10 electrode
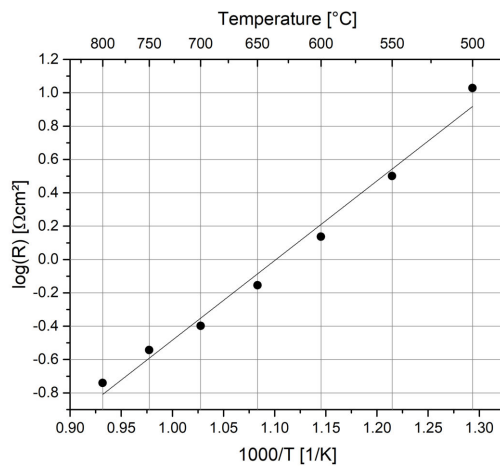
Figure 4.3: Arrhenius plot of the resistance of a porous GDC10 electrode including the linear fit

4.1.2 LSF porous

Two different LSF samples were tested. The first sample consisted of a round YSZ substrate with a diameter of 15 mm that had a GDC thin film deposited on both sides as a diffusion barrier. The electrode paste that was brushed on the substrate, was made from LSF powder produced by Pechini synthesis. Platinum paste was brushed on the electrodes as a current collector. The second sample consisted of a 5 mm x 5 mm x 0.5 mm YSZ single crystal and a thin layer of porous GDC as diffusion barrier on both sides. The electrodes were again brushed on the substrate, followed by the current collector. The electrode paste used for the second sample was made from commercial LSF powder. Both samples were sintered at 1050°C for three hours.

The samples were measured in oxidizing (1% O_2) and reducing (humidified hydrogen) atmospheres in the temperature range of 500°C to 850°C. Figure 4.4 displays some example spectra from the first sample. In reducing conditions the spectra showed a dominant low frequency feature that got more depressed and complex with increasing temperature, followed by an intermediate frequency shoulder. On the high frequency end, low temperature spectra showed the beginning of a second semicircle, whereas high temperature spectra had an inductive loop feature. In oxidizing conditions the low frequency feature is more pronounced and its peak frequency is outside the measuring range at low temperatures. Again, the spectra showed an intermediate frequency shoulder and a high frequency feature that is accompanied by an inductive loop at high temperatures.

The spectra of the second sample (Figure 4.5) showed the beginning of a high frequency semicircle followed by an intermediate frequency shoulder. The dominant low frequency feature was only slightly depressed in reducing conditions. In oxidizing conditions the feature was more depressed and not fully included in the spectra at low temperatures.

As the shape of the dominant feature of the first sample changed substantially with increasing temperature, a meaningful equivalent circuit fit was not possible. Therefore, the electrode resistances were directly extracted from the spectra. With the second sample fitting with a serial connection of a resistor and two R∥CPE elements, one for the intermediate frequency feature and one for the dominant low frequency feature, was possible. The electrode resistances of both samples are depicted in Figure 4.6 for a temperature cycle 500°C-850°C-500°C. Sample 1 showed significant hysteresis in reducing conditions with higher resistances while heating up. Sample 2 had considerably lower electrode resistances at higher temperatures in reducing conditions. For example, at 750°C set temperature the area specific resistance (ASR) of sample 1 was 1.10 Ωcm^2, whereas sample 2 only had an ASR of 0.53 Ωcm^2. At low temperatures, however, sample 1 had lower area specific resistances. In oxidizing conditions, extracting of meaningful electrode resistances
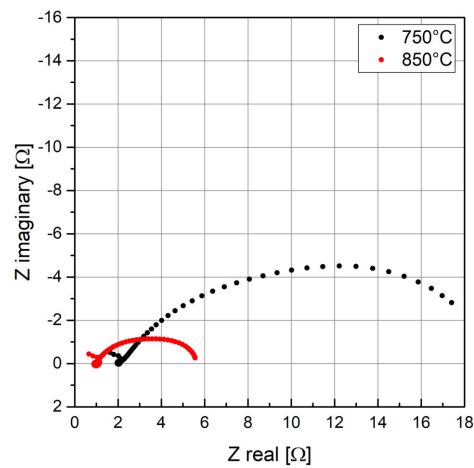
34
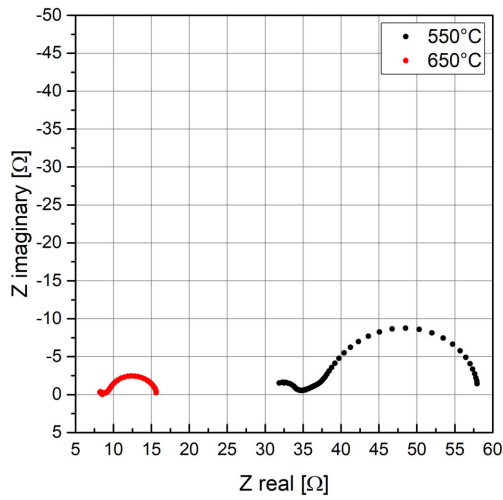
(a) 550°C and 650°C, reducing
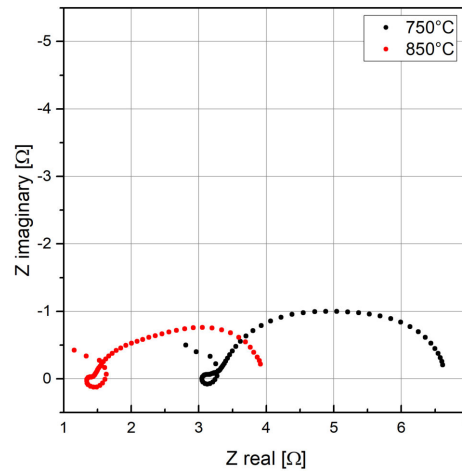
(b) 750°C and 850°C, reducing
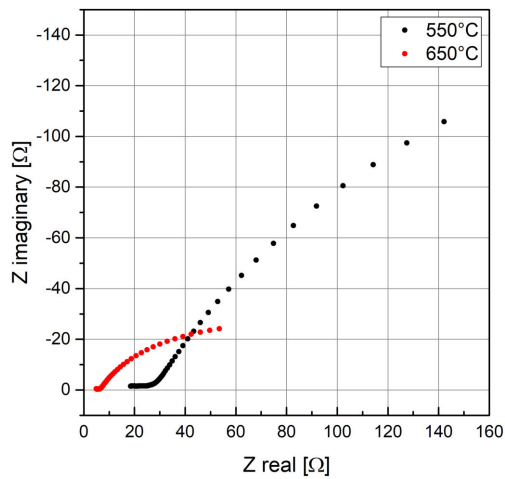
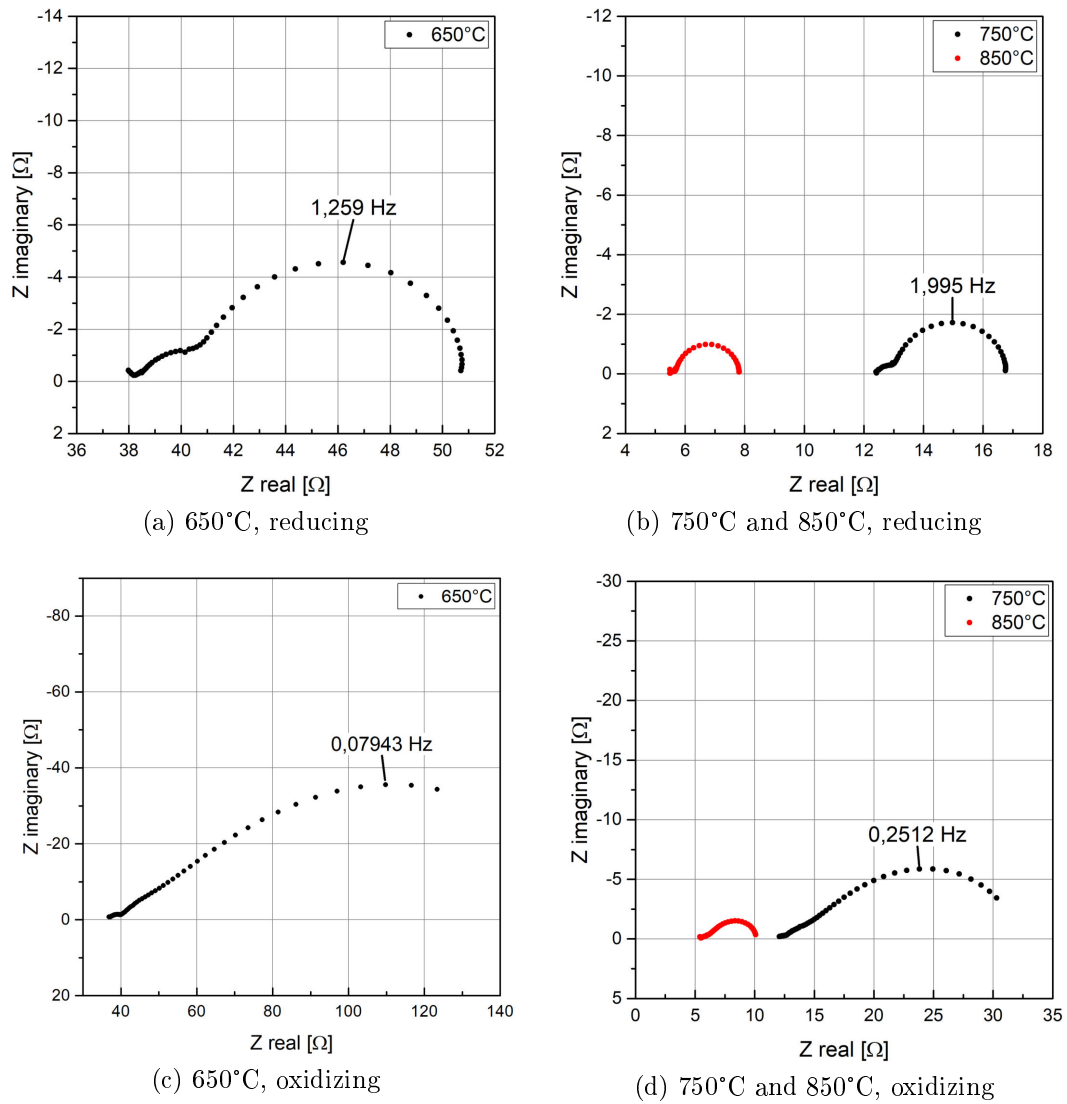(c) 550°C and 650°C, oxidizing

(d) 750°C and 850°C, oxidizing

Figure 4.4: Example impedance spectra of symmetric porous LSF sample made from Pechini synthesis LSF powder in reducing and oxidizing conditions

was only possible starting at a set temperature of 600°C. Again, sample 2 has lower ASRs than sample 1 (2.81 Ωcm^2 and 5.45 Ωcm^2 at 750°C set temperature, respectively). Figure 4.7 depicts the capacitance of the main feature from the second sample in oxidizing and reducing conditions.

Due to the lower electrode resistances and more significant spectra (clearer features, no loops) at higher temperatures, the LSF paste made from the commercial LSF powder was used for further measurements on LSF electrodes.

(a) 650°C, reducing

(b) 750°C and 850°C, reducing

(c) 650°C, oxidizing

(d) 750°C and 850°C, oxidizing

Figure 4.5: Example impedance spectra of symmetric porous LSF sample made from commercial LSF powder in reducing and oxidizing conditions. The peak frequencies of the spectra obtained at 650°C and 750°C are included in the plots.

(a) Reducing conditions

(b) Oxidizing conditions
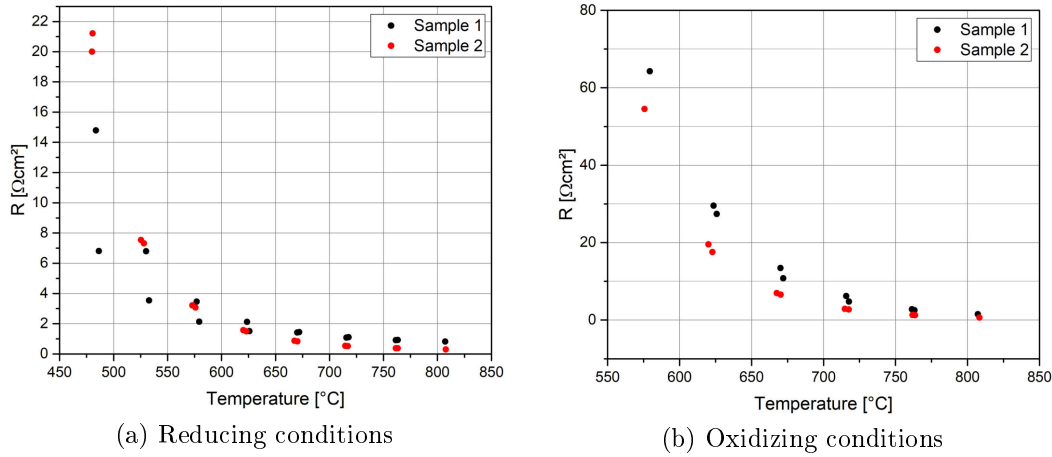
Figure 4.6: Electrode resistances of one electrode of the symmetric LSF samples in oxidizing and reducing conditions from a heating and cooling cycle. Sample 1 was made from Pechini synthesized LSF powder, sample 2 from commercially available LSF powder.
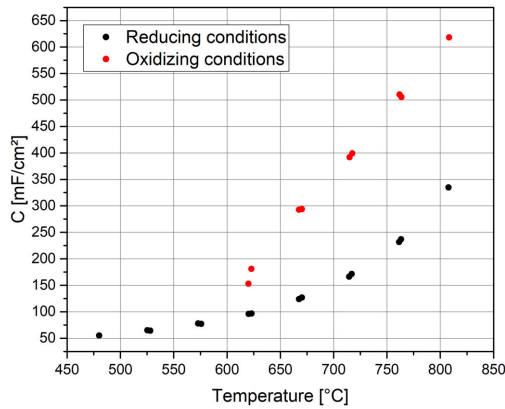
Figure 4.7: Capacitance of the main feature of a LSF electrode made from commercial LSF powder (sample 2) in oxidizing and reducing conditions.

4.1.3 Pt/YSZ porous

The sample consisted of a 5 mm x 5 mm x 0.5 mm YSZ single crystal substrate on which the electrodes were brushed and subsequently sintered at 1300°C for one hour. Measurements were conducted in oxidizing (1% O_2) and reducing (Ar + H_2/H_2O) atmospheres and in a temperature range from 500°C to 850°C. The spectra in reducing conditions showed a high frequency shoulder followed by a dominant low frequency semicircle. In oxidizing conditions, the spectra consisted of a single depressed semicircle. With increasing temperature, a second feature at low frequencies became apparent which was fully separated from the main semicircle at high temperatures. Some example spectra are depicted in Figure 4.8.

(a) 650°C and 750°C, reducing

(b) 650°C and 750°C, oxidizing
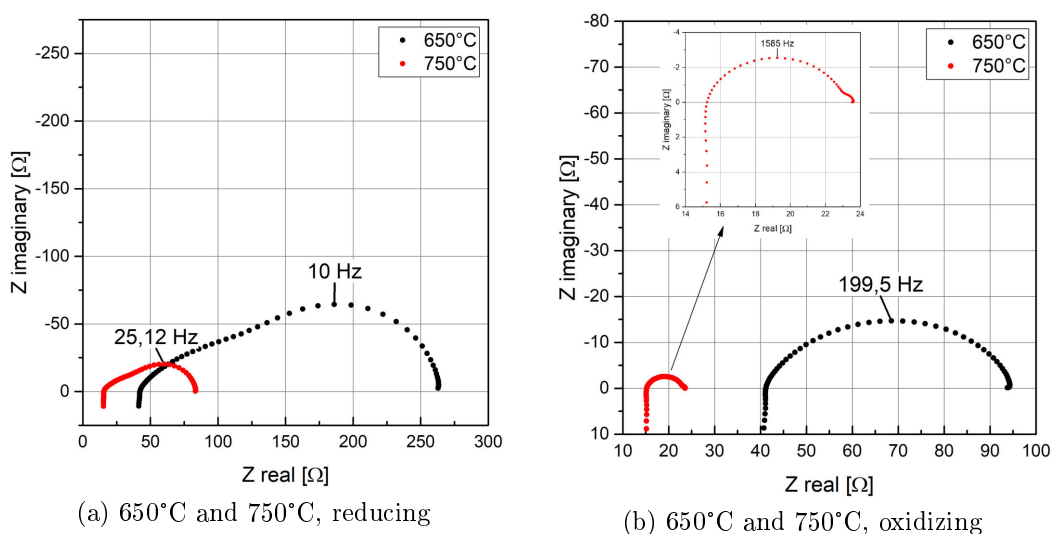
Figure 4.8: Example impedance spectra of symmetric porous Pt/YSZ sample in reducing and oxidizing atmospheres. Inset (b) includes a zoom-in of the spectrum measured at 750°C.

In a first step the spectra obtained in both atmospheric conditions were fitted with an equivalent circuit consisting of a serial connection of a resistor and two R‖CPE elements to extract the electrode resistance and capacitance. The values are presented in Figure 4.9. The ASR of one electrode at 750°C was 8.56 Ωcm^2 in reducing conditions and 0.99 Ωcm^2 in oxidizing conditions. The capacitance values were rather constant between 1.1 mF/cm^2 and 1.4 mF/cm^2 in reducing conditions, whereas they reached down to 0.08 mF/cm^2 in oxidizing atmosphere at 800°C.

In Figure 4.10 Arrhenius plots of the electrode resistances are depicted. The low frequency feature in oxidizing conditions, which was only visible at high tem-

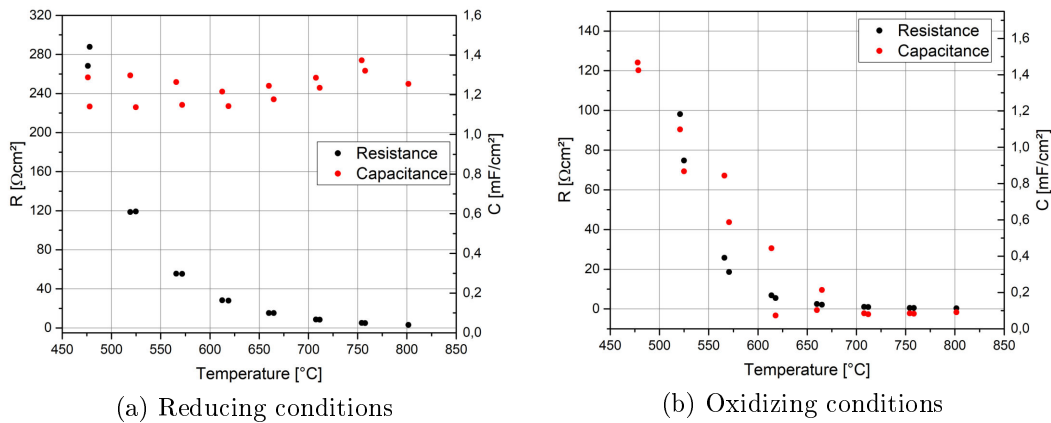(a) Reducing conditions

(b) Oxidizing conditions

Figure 4.9: Electrode resistances and capacitance values of a Pt/YSZ electrode in oxidizing and reducing conditions from a heating and cooling cycle

peratures, was not thermally activated. Besides, its peak frequency was constant at around 15 Hz. It was therefore attributed to limited gas diffusion to the active sites within the electrode [46] and excluded from the electrode resistance in oxidizing conditions. The calculated activation energies for the electrode processes were 0.958 eV (reducing) and 1.582 eV (oxidizing), respectively.

(a) Reducing conditions

(b) Oxidizing conditions
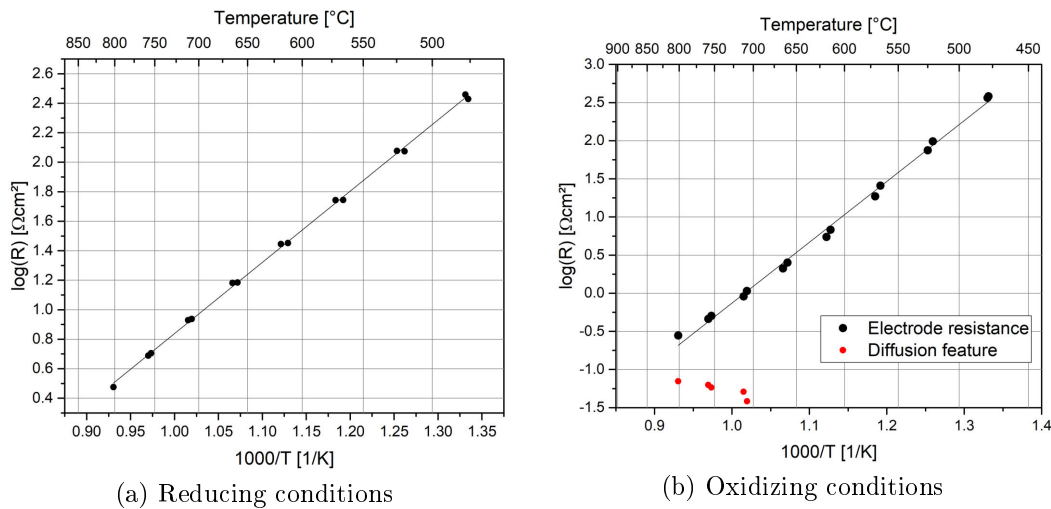
Figure 4.10: Arrhenius plot of the electrode resistance of Pt/YSZ including the linear fit. In inset (b) the resistance values of the high temperature and high frequency feature, which is attributed to limited gas diffusion, are included.

As a second step, the spectra in reducing atmosphere were fitted with the transmission line equivalent circuit described in section 2.3.3. Parameters representing interfacial effects and the inductance of the wiring were included in the fit. A comparison of the two fits revealed that the extracted values and activation energy for the ASR differed by less than 3 %. The effective ionic transport resistance R_{ion}, obtained from the transmission line fit, is linked to the bulk conductivity of the ion conducting phase by

$$\sigma_{eff} = \frac{1}{R_{ion}} = \sigma_{bulk} * \frac{\epsilon}{\tau} \tag{4.2}$$

where τ and ϵ are the tortuosity and volume fraction of the ionic conductor, respectively. These microstructural parameters can be obtained through tomographic methods but were not accessible for the sample. Therefore, the parameters were estimated to be 4 for the tortuosity and 0.35 for the volume fraction (based on Ref.[46]). The calculated bulk conductivity of the ion conducting YSZ phase at approximately 700°C ($1.28 * 10^{-3}$ S/cm) was one order of magnitude smaller than the actual bulk value taken from Ref.[47] ($2.51 * 10^{-2}$ S/cm). The low ionic conductivity of the electrode was presumed to originate from insufficient percolation of the YSZ particles. To increase the particle size and hence the percolation, the sample was sintered again at a higher temperature (1400°C for one hour). A comparison of the impedance spectra at 750°C set temperature from before and after the re-sintering is given in Figure 4.11a. One can clearly see the increased polarization resistance and the changed shape of the spectrum. As expected, the ionic conductivity of the electrode was enhanced due to larger YSZ particles. However, also the entire electrode resistance was drastically increased, see Figure 4.11b. This increase was notably larger than the expected increase originating from degradation of the electrode. It was therefore attributed to a decrease of active TPBs due to the larger particles. The activation energy of the ionic conductivity was 0.943 eV before re-sintering, 1.108 eV after re-sintering and 0.853 eV for the bulk data.

Due to the substantial increase of the electrode resistance resulting from the higher sintering temperature, all further Pt/YSZ samples were sintered at 1300°C, accepting the sub-optimal ionic conductivity. Notably, the exact composition and purity of the Pt/YSZ cermet is a trade secret, so the low ionic conductivity may be related to impurities as well as to sub-optimal microstructure.
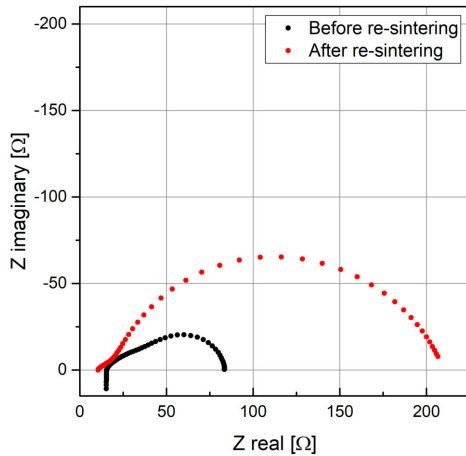
(a) Impedance spectra at 750°C, reducing
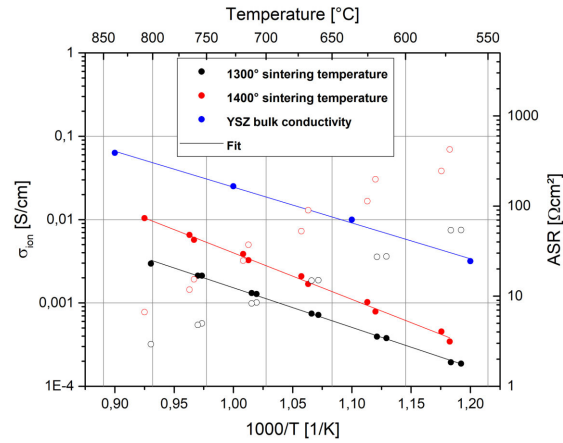
(b) Ionic bulk conductivity and ASR

Figure 4.11: Inset (a) depicts a comparison of the impedance spectra of the Pt/YSZ sample before and after the re-sintering at 1400°C. The spectra were both obtained in reducing atmospheres and at a set temperature of 750°C. Inset (b) shows the calculated ionic bulk conductivity of the sample before and after the re-sintering (full symbols), the bulk conductivity of YSZ, taken from Ref.[47], and the ASR of the sample (open symbols).

4.1.4 GDC thin film

Samples with GDC thin films as working electrodes were prepared on 5 mm x 5 mm x 0.5 mm YSZ single crystals following the procedure described in subsection 3.1.1. The counter electrodes were either porous Pt/YSZ or porous LSF. For these samples, the properties of the GDC thin films should be equal, while the CE properties differ, as shown in sections subsection 4.1.2 and subsection 4.1.3.

Cells with Pt/YSZ counter electrodes were measured in humidified 2.5% hydrogen in argon at temperatures ranging from 500°C to 800°C and with bias up to ± 300 mV. Figure 4.12 displays some example spectra at different temperatures and with anodic and cathodic bias. The spectra without bias showed an intermediate frequency shoulder followed by a dominant low frequency depressed semicircle. At higher temperatures, the dominant semicircle was stretched and a third feature appeared in the spectra. As the polarization resistance of the sample is about one order of magnitude larger than the resistances of porous samples, it was fully attributed to the thin film. Under cathodic bias the main feature separated into two distinct semicircles. The first feature decreased in size with increasing negative bias, whereas the second feature increased with increasing bias. The spectra with

41

(a) Open-circuit measurement
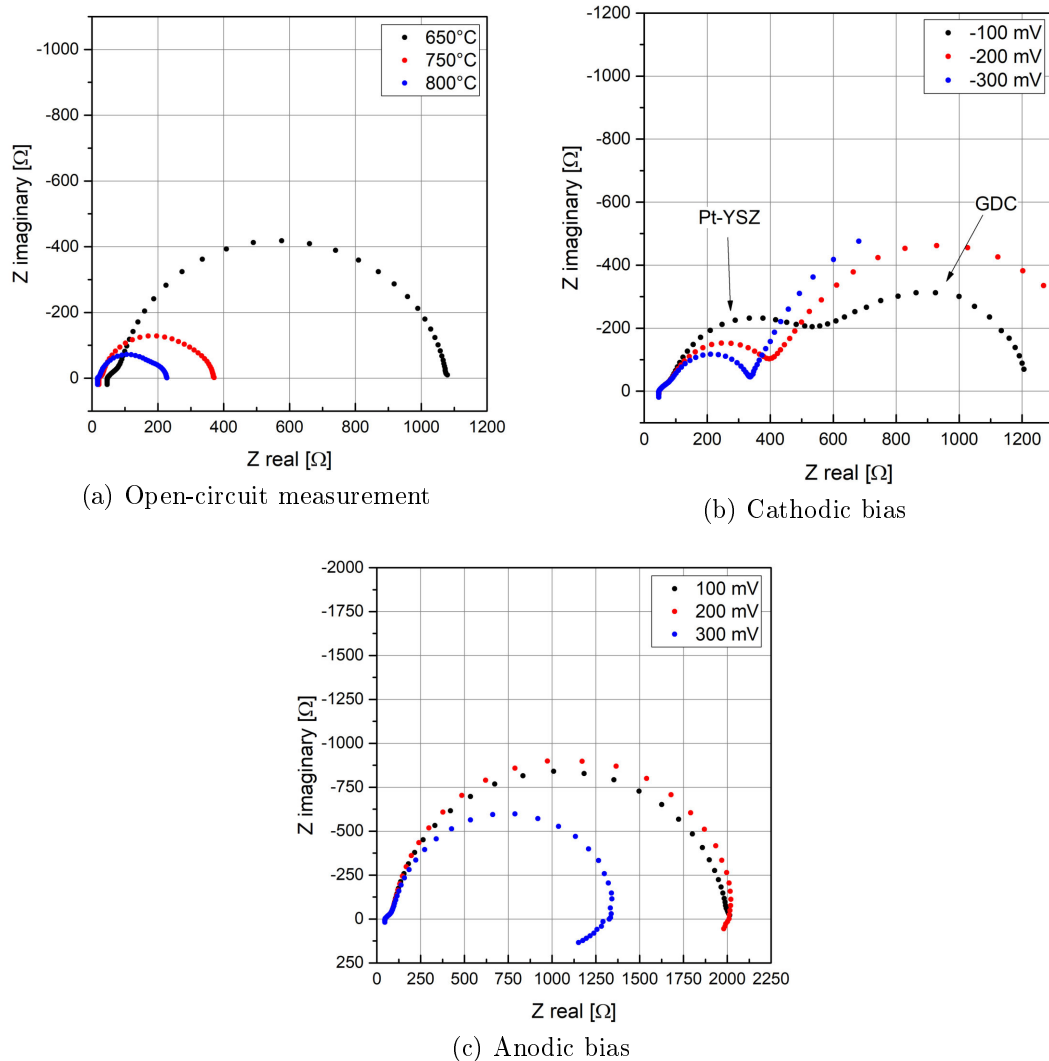
(b) Cathodic bias

(c) Anodic bias

Figure 4.12: Impedance spectra of the sample with a GDC thin film electrode and a porous Pt/YSZ counter electrode. Spectra under bias were measured at a set temperature of 650°C.

applied cathodic bias were fitted with an equivalent circuit consisting of a serial connection of a resistor and two R||CPE elements. The calculated resistances and capacitance values are shown in Figure 4.13. Due to the rather constant capacitance of the first feature at around 0.33 mF/cm^2 and the scaling of the capacitance of the second feature with increasing negative bias, the features were attributed to the Pt/YSZ counter electrode and to the GDC thin film, respectively. Under anodic bias, the spectra had similar shapes as spectra without bias but with an

added low frequency inductive feature at higher bias voltages. We could conclude that the Pt/YSZ CE has an ASR which is similar to the ASR of the GDC thin film and a clear separation of both features is not straight forward.
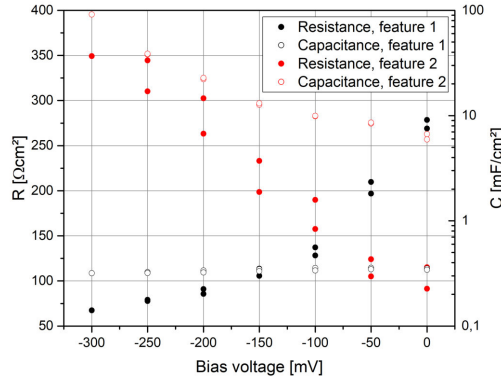
Figure 4.13: Resistances and capacitance values of both features of the sample with a GDC thin film electrode and a Pt/YSZ counter electrode at 650°C set temperature and varying cathodic bias voltage

The second GDC thin film sample had porous LSF brushed on the substrate as a counter electrode, with a porous GDC buffer layer underneath. Pt-paste was brushed on the electrode as a current collector. Previous characterization predicts a much lower ASR of about 2 Ωcm^2 at 600°C in reducing conditions for this type of CE.

The sample was first measured in reducing (humidified 2.5% hydrogen in argon) and oxidizing (1% O$_2$ in nitrogen) atmospheres at temperatures ranging from 500°C to 850°C. The spectra in reducing atmosphere showed an intermediate frequency shoulder and an only slightly depressed low frequency semicircle. At elevated temperatures, the semicircle was more pronounced and dominated the electrode impedance, see Figure 4.14. The spectra were fitted with an equivalent circuit consisting of a serial connection of a resistor and two R||CPE elements to parameterize the two features. An Arrhenius plot of the resistances revealed activation energies of 0.956 eV and 0.814 eV for feature 1 and feature 2, respectively (Figure 4.15a). Figure 4.15b shows the capacitance of the main feature. A comparison of this capacitance and capacitance of the dominant feature of the first GDC thin film sample at open-circuit voltage (Figure 4.13) revealed good accordance. These values were about 10 times smaller than the capacitance of the porous GDC electrode which is in agreement with the interpretation of the capacitance as chemical capacitance (scaling with electrode thickness).

Example spectra of the measurements in oxidizing atmosphere are depicted in Figure 4.16. These spectra did not show an intermediate frequency shoulder but a dominant low frequency semicircle and were therefore fitted with a resistor and

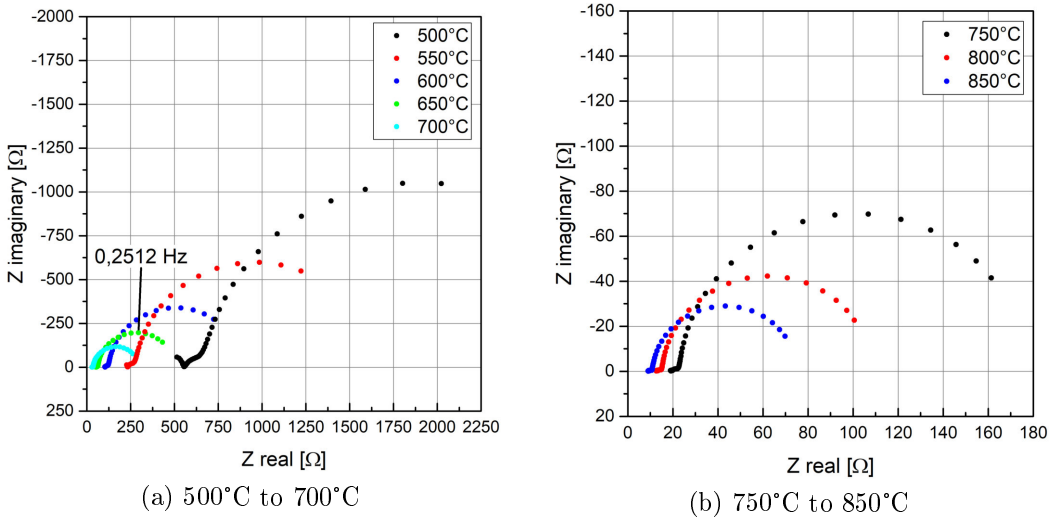(a) 500°C to 700°C

(b) 750°C to 850°C

Figure 4.14: Impedance spectra of the sample with a GDC thin film electrode and a porous LSF counter electrode in reducing atmosphere. The peak frequency of the spectrum measured at 650°C set temperature is included in inset (a).
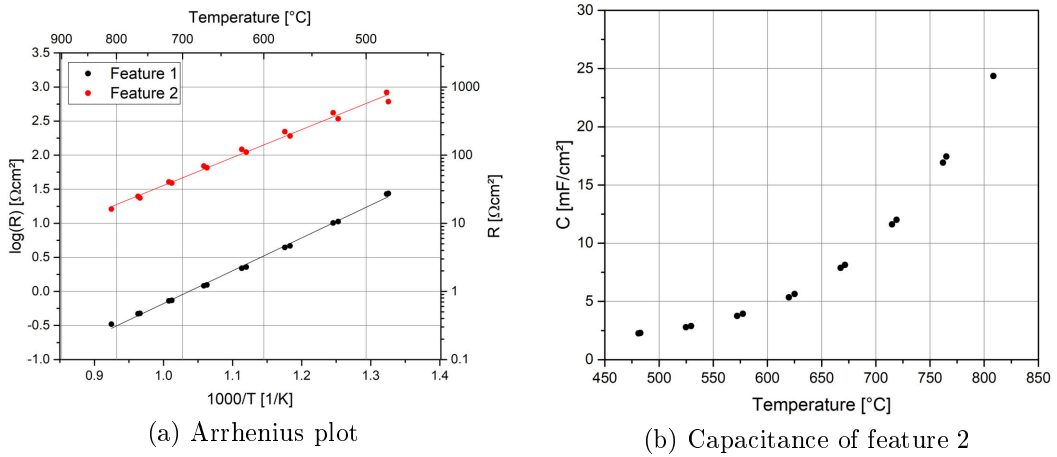

(a) Arrhenius plot

(b) Capacitance of feature 2

Figure 4.15: Inset (a) depicts an Arrhenius plot of the resistances of the sample with a GDC thin film electrode and a LSF counter electrode in reducing atmosphere, including a linear fit. Inset (b) shows the capacitance of feature 2.

a single R∥CPE element. Fitting was only possible starting with a temperature of 650°C, as below that the spectra did not close. Figure 4.17 depicts the capacitance

of the electrode and an Arrhenius plot of the electrode resistance. The calculated activation energy of the electrode resistance was 1.272 eV. As the capacitance was not thermally activated and was almost two order of magnitude smaller than in reducing conditions, it was interpreted as interfacial capacitance. This is in line with the defect chemistry of GDC, which predicts almost no oxygen non-stoichiometry from 10^{-10} to 1 bar oxygen partial pressure [48]. Interestingly, the ASR in oxidizing and reducing conditions is comparable, although GDC is considered as an electrolyte material in air.
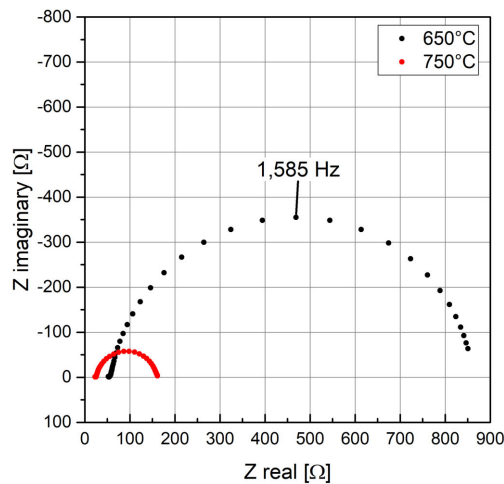
Figure 4.16: Example impedance spectra of the sample with a GDC thin film electrode and a LSF counter electrode in oxidizing atmosphere. The peak frequency of the spectrum measured at 650°C set temperature is included in the graphic.

Following the temperature cycles, measurements were conducted in changing reducing atmospheres and with applied bias voltage ($\pm$ 300 mV) at 650°C set temperature. The spectra in changing atmospheres all showed an intermediate frequency shoulder which grew into a separate semicircle under stronger reducing conditions. The main low frequency semicircle was included in the spectra depending on the conditions. In less reducing conditions a bigger part of the feature was in the measured frequency range than in more reducing conditions. Figure 4.18 shows some example spectra.

The spectra were again fitted with an equivalent circuit consisting of a serial connection of a resistor and two R||CPE elements to obtain resistances and capacitance values which are plotted against the oxygen partial pressure in Figure 4.19.

The oxygen partial pressure in reducing conditions is defined by the equilibrium
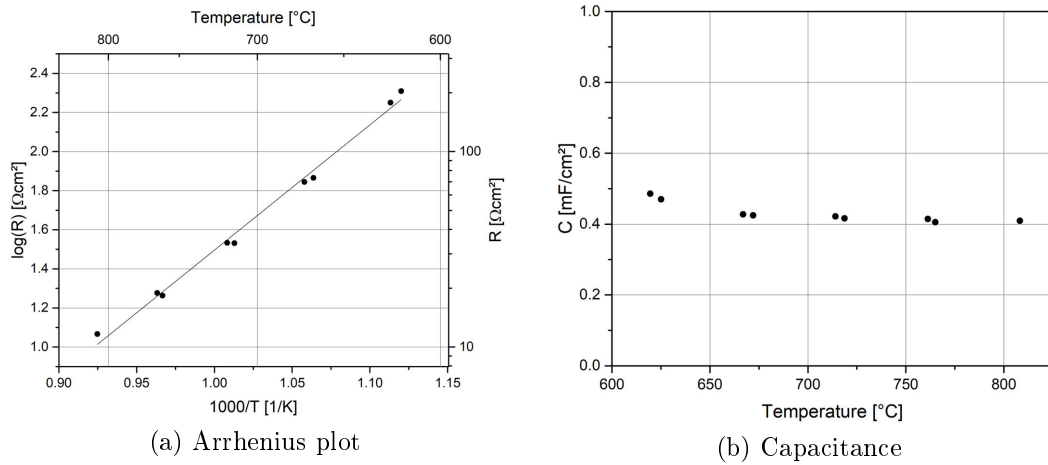
(a) Arrhenius plot

(b) Capacitance

Figure 4.17: Inset (a) depicts an Arrhenius plot of the resistance (dominant feature) of the sample with a GDC thin film electrode and a LSF counter electrode in oxidizing atmosphere, including a linear fit. Inset (b) shows the capacitance of the dominant feature.
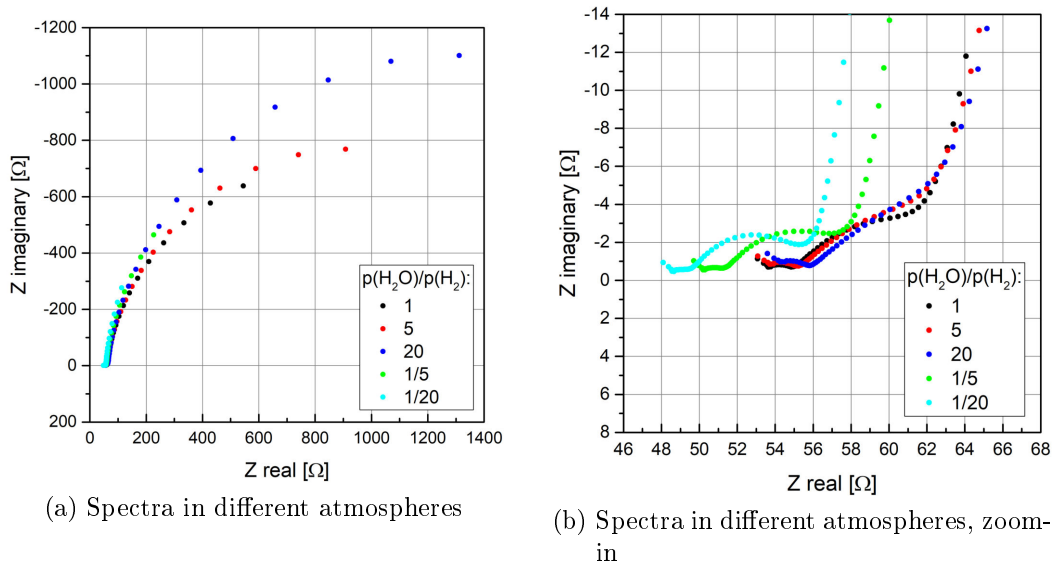

(a) Spectra in different atmospheres

(b) Spectra in different atmospheres, zoom-in
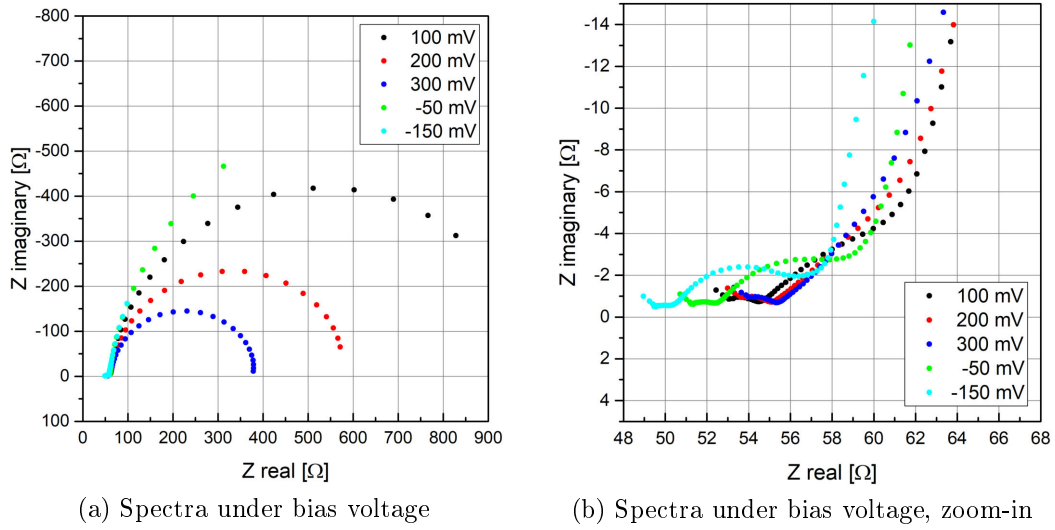
Figure 4.18: Impedance spectra of the sample with a GDC thin film electrode and a LSF counter electrode in different atmospheres at 650°C set temperature. Inset (b) shows an enlargement of the high frequency part of the spectra.

of the hydrogen oxidation equation and the mass action law:

$$H_2 + \frac{1}{2}O_2 \rightleftharpoons H_2O, \tag{4.3}$$

$$K = \frac{p(H_2O)}{\sqrt{p(O_2)} * p(H_2)}. \tag{4.4}$$

By calculating the equilibrium constant K from thermodynamic data [49] at the given temperature (620°C) and inserting the partial pressures of H_2 and H_2O, the oxygen partial pressure was calculated for every gas mixture.

(a) Electrode resistances

(b) Capacitance of feature 2
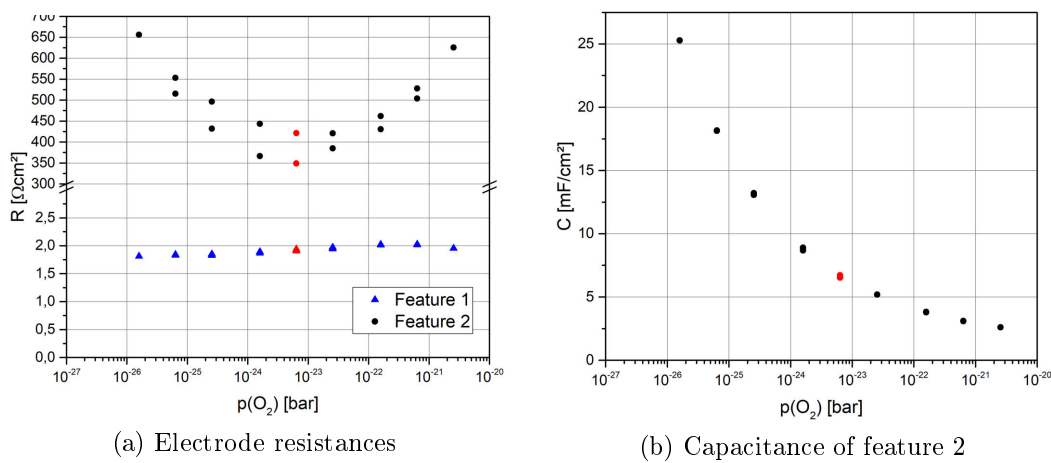
Figure 4.19: Inset (a) depicts the resistances of the sample with a GDC thin film electrode and a LSF counter electrode at different oxygen partial pressures and 620°C. Inset(b) shows the capacitance of feature 2. The measurements were conducted in cycles of high -> low -> high oxygen partial pressure. The data obtained at a one-to-one ratio of H_2 and H_2O is marked in red.

The resistance of feature 1 was only slightly affected by changing atmospheres. The resistance of the main feature had a minimum at a one-to-one ratio of water and hydrogen and increased with higher and lower oxygen partial pressure. As expected, the chemical capacitance of the sample increased with decreasing oxygen partial pressure.

The measurements under bias voltage were performed at 650°C oven temperature and at a one-to-one ratio of hydrogen and water. Some example spectra are presented in Figure 4.20. Again, the spectra showed an intermediate frequency shoulder and a dominant low frequency semicircle. Applying bias leads to a changing effective oxygen partial pressure in the working electrode, according

47

to Equation 2.28. Therefore, cathodic bias resulted in more reducing conditions, whereas anodic bias resulted in less reducing conditions. Comparing the spectra to the measurements in changing atmospheres revealed good accordance: Under cathodic bias the intermediate frequency shoulder was clearly separated from the dominant feature, which was not fully included in the spectra due to a low characteristic frequency. Fitting of the spectra was done with a resistor and two R‖CPE elements. However, spectra obtained at bias voltages of -200 mV and below could not be fitted as a too little part of the dominant feature was included in the measuring range.

(a) Spectra under bias voltage

(b) Spectra under bias voltage, zoom-in

Figure 4.20: Impedance spectra of the sample with a GDC thin film electrode and a LSF counter electrode under bias at 650°C set temperature. Inset (b) shows an enlargement of the high frequency part of the spectra.

The extracted resistances and capacitances are depicted in Figure 4.21a-b. The effective overpotential of the electrode is not identical with the applied bias voltage because of losses in the electrolyte and at interfaces (represented through the offset resistance in the equivalent circuit fits). When neglecting the influence of the counter electrode (which is reasonable as the ASR of the counter electrode is two orders of magnitude smaller) the effective overpotential of the working electrode η_{WE} can be calculated with

$$\eta_{WE} = U_{bias} - R_{offset} * I \qquad (4.5)$$

where U_{bias} denotes the applied bias voltage, R_{offset} the high frequency offset resistance and I the measured current.

48

The resistance of feature 1 showed only minor changes with applied bias voltage, whereas the main feature decreased with increasing bias. The scaling of the resistance with effective oxygen partial pressure differed between measurements in changing atmospheres and under bias voltage. This was expected as the electrode was measured far away from the equilibrium when applying bias voltage, contrary to the case with changing atmospheres were the electrode is measured in the vicinity of the equilibrium. Considering the chemical capacitance, one can see good agreement between the two different measuring cycles. As the chemical capacitance is a property of the electrode bulk and depending on the concentrations of charge carriers (which themselves depend on the chemical potential of oxygen in the electrode), it is influenced in an analogue way by changing atmospheres and applying bias voltage, as shown in Figure 4.21b. Fitting the logarithm of the chemical capacitance to the logarithm of the oxygen partial pressure revealed a scaling of $C_{chem} \propto p(O_2)^{-0.24}$, see Figure 4.21c. This exponent is very close to the scaling of $p(O_2)^{-0.25}$ which is expected from literature data [32].

Lastly, the current-voltage characteristic was recorded. Figure 4.22 depicts the measured current normalized to the electrode area over the effective overpotential of the working electrode. One can notice a linear regime between -100 mV and +100 mV effective overpotential. Higher or lower overpotential resulted in strong non-linear behavior. The anodic branch showed a steeper course and peaked at around 2 mA/cm^2, whereas the cathodic branch only reached around -1 mA/cm^2. This coincides with the observed electrode resistance (decrease under anodic bias and increase under cathodic bias) that is inversely proportional to the slope of the current-voltage characteristic.

While extracting the sample from the holder, once the measurement was completed, the current collector from the LSF counter electrode was completely delaminated. Due to the large contact surface between the current collector and the Pt meshes, combined with high measuring temperatures, the adhesion between the electrode and current collector is weaker than between current collector and Pt meshes. As it generally is not possible to know if the connection between electrode and current collector was already impaired during the measurement, and therefore influenced the measuring results, delaminating of the current collector is unfavorable. Unfortunately, at least parts of the current collectors from almost every sample delaminated upon extracting.

(a) Electrode resistances

(b) Capacitance of feature 2
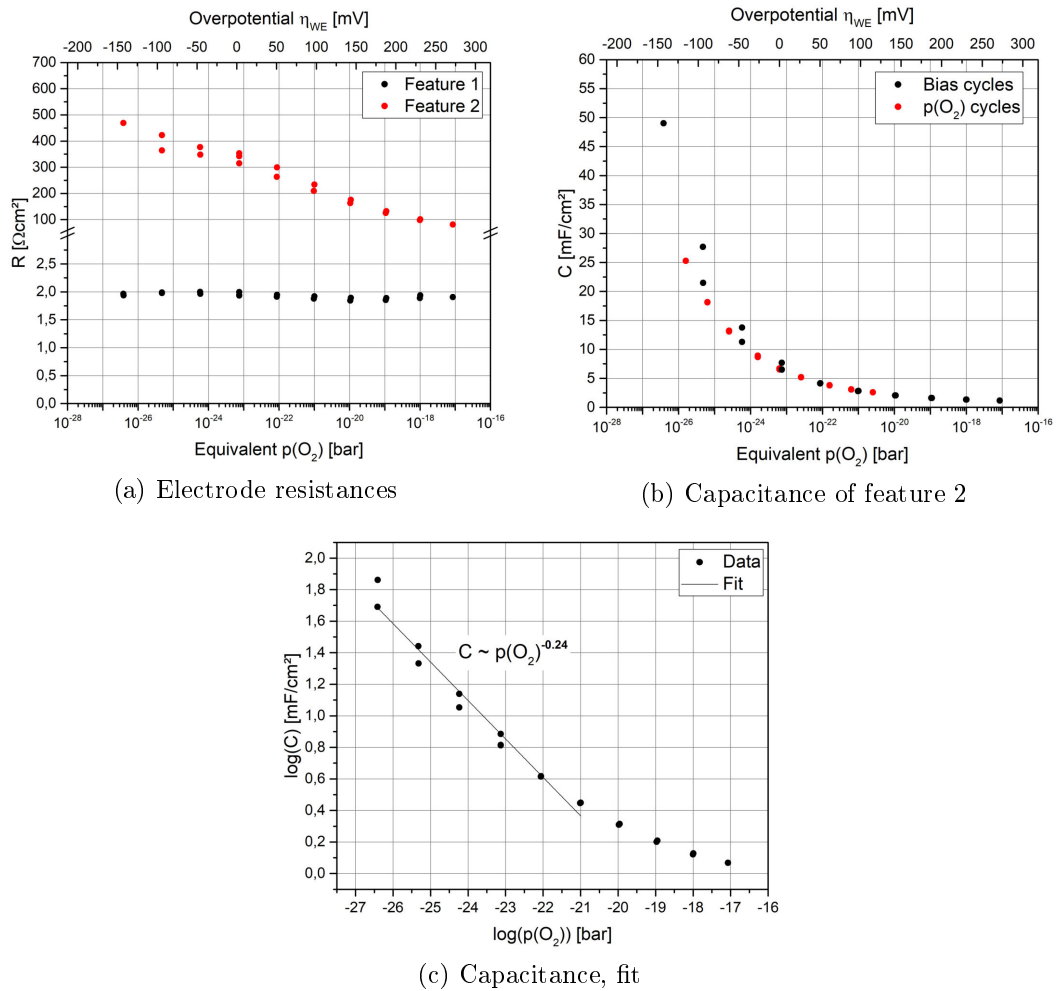

(c) Capacitance, fit

Figure 4.21: Inset (a) depicts the resistances of the sample with a GDC thin film electrode and a LSF counter electrode at different equivalent oxygen partial pressures and the corresponding overpotential at the working electrode. Inset (b) shows the capacitance of feature 2 in comparison to the results from the measurements with changing atmospheres. A fit of the chemical capacitance in the low oxygen partial pressure range is depicted in inset (c).
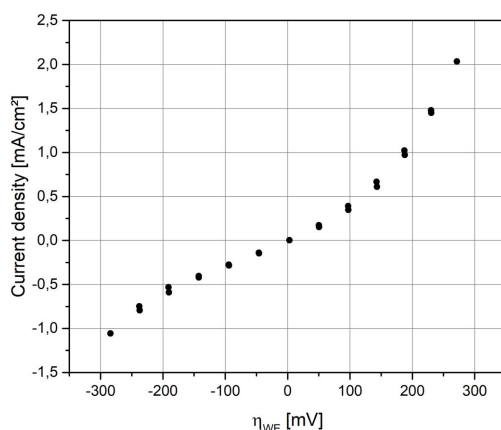
Figure 4.22: Current-voltage characteristic of the sample with a GDC thin film electrode and a LSF counter electrode measured at a one-to-one ratio of hydrogen and water and at 650°C set temperature

4.2 Measurements on three-electrode samples

With the experience gained from the two-electrode samples, three-electrode samples were produced. In the beginning, asymmetric samples were investigated on which WE and CE have very different peak frequencies. Therefore, artifacts in three-electrode measurements, arising from imperfect sample fabrication, should be separable from the actual measuring result. After that, also symmetric samples were investigated and the results were compared to the asymmetric samples.

4.2.1 LSF with Pt/YSZ

The sample was prepared following the procedure mentioned in subsection 3.1.3 with porous LSF as working electrode and porous Pt/YSZ as counter and reference electrode. Measurements were conducted in oxidizing and reducing conditions at different oxygen partial pressures and with applied bias voltage at 650°C and 750°C. Before the measurement was started, a plausibility check was performed. For this purpose, the spectra of both half cells, the spectrum of the full cell and of the wing electrode were measured and compared. Figure 4.23a shows the individual spectra of the two half cells. Both spectra contained high frequency artifacts and the spectrum of the Pt/YSZ half cell also showed a low frequency inductive artifact feature. The peak frequency of the low frequency artifact corresponded to the characteristic frequency of the main feature of the LSF spectrum. The cause of this artifact was most likely a frequency-dependent current distribution resulting from the asymmetric structure of the sample, leading to a cross contamination

from the counter electrode. However, as the peak frequencies of both electrodes were separated by orders of magnitude, the artifact did not interfere with the relevant parts of the spectra.

The spectrum of the wing electrode is presented in Figure 4.23b. It was measured by connecting the wing electrode to the CE port and the RE+ port of the impedance analyzer and the counter electrode to the WE port and the RE- port. The shape of the spectrum was similar to the shape of the Pt/YSZ half cell spectrum, except for the low and high frequency artifacts. Comparing the electrode resistances, the wing electrode had an about 30 times larger ASR than the regular Pt/YSZ electrode. Considering the different sizes of the electrodes, this result is as expected. A comparison between the sum of the half cells and the full cell (corresponding to a two-electrode measurement) is depicted in Figure 4.23c. One can see an offset of about 5 Ω between the two spectra and a more pronounced low frequency feature in the sum spectrum. As the spectra were measured while heating up the sample, the temperature was not identical for the three measurements. The full cell spectrum was measured at a slightly higher temperature than the half cells which explains the lower electrolyte resistance and the lower electrode resistance. Apart from that, the spectra coincided and the two electrode features were well separated, with the Pt/YSZ feature at about 400 Hz and the LSF feature at about 0.2 Hz. Also, the high frequency artifacts, which were visible in the half cell spectra, canceled out when adding up the two spectra.

The LSF half cell spectra obtained at 650°C between 10^5 and 10^{-2} Hz are presented in Figure 4.23d and Figure 4.24. The spectra measured in different atmospheres showed a high frequency shoulder followed by a 45° slope and a dominant low frequency feature. The length of the slope and the shape of the main feature were depending on the oxygen partial pressure. Low oxygen content resulted in short slopes and more pronounced semicircles, whereas high oxygen content led to longer slopes and more depressed semicircles. The measurements under bias voltage were conducted in 1% oxygen in nitrogen and the spectra showed similar behavior: anodic bias led to more depressed semicircles with high peak frequencies (20 Hz at +190 mV effective overpotential), whereas cathodic bias resulted in short 45° slopes and low peak frequencies (0.1 Hz at -160 mV effective overpotential). However, under high anodic bias, the spectra showed the beginning of a low frequency inductive artifact in the size of about 0.2 Ωcm^2.

The data was fitted with the transmission line equivalent circuit described in section 2.3.3. Parameters representing interfacial effects were fixed to zero. Example spectra with included fit are depicted in Figure 4.25, where good accordance between fitted curves and measured spectra can be seen. The shorter 45° slope of the red spectrum is indicative for higher ionic conductivity.

The extracted parameters from the equivalent circuit fit are presented in Fig-

(a) Half cell spectra

(b) Wing electrode impedance

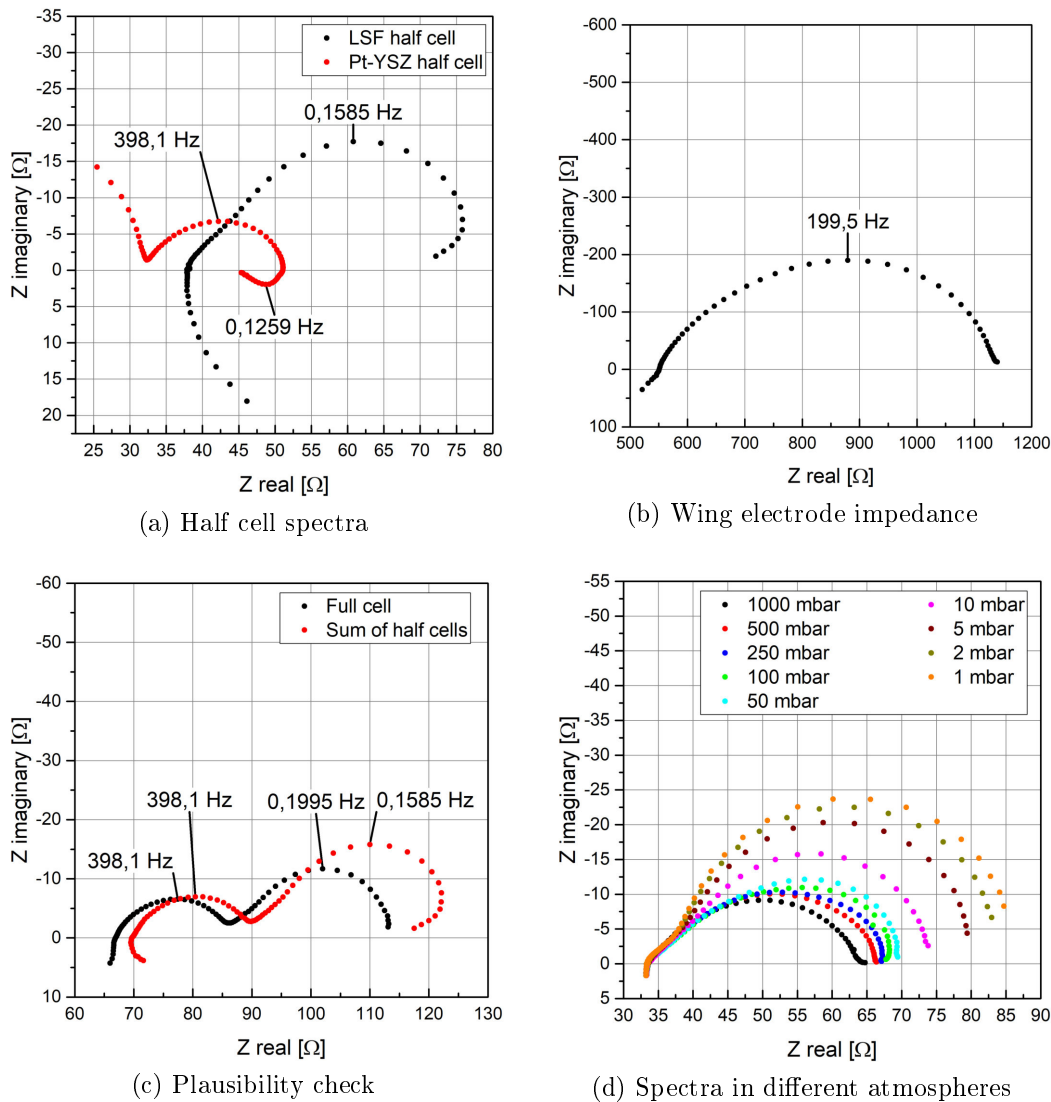(c) Plausibility check

(d) Spectra in different atmospheres

Figure 4.23: Impedance spectra of LSF three-electrode sample with Pt/YSZ counter electrode. Inset (a) depicts the spectra of both half cells, inset (b) the spectrum of the wing electrode. A comparison between the impedance spectrum of the full cell and the sum spectrum of both half cells is presented in inset (c). The spectra shown in (a)-(c) were obtained in 1% O_2 around 620°C and between 10^6 and 10^{-2} Hz. Inset (d) shows the LSF half cell impedance spectra at 650°C set temperature and different oxygen partial pressures.

(a) Negative bias   (b) Positive bias
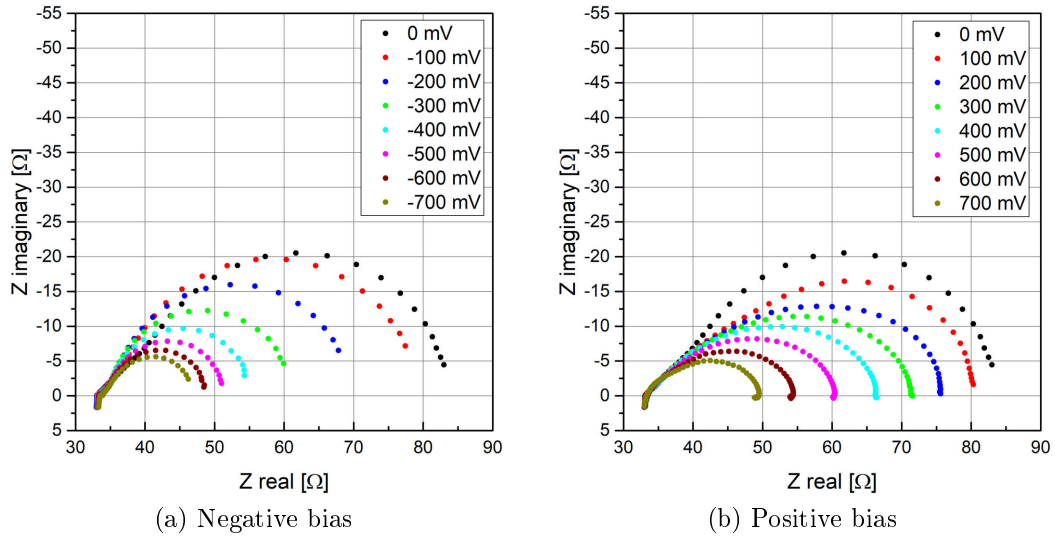
Figure 4.24: Impedance spectra of LSF half cell of the LSF three-electrode sample with Pt/YSZ counter electrode measured at 650°C set temperature in 1% O_2 under different bias voltages.

ure 4.26. The electrode resistance increased with decreasing oxygen partial pressure. With applied bias, the resistance showed a maximum at zero bias voltage and decreased with anodic and cathodic bias. This behavior is as expected from LSF thin films [13]. For bias cycles, the overpotential was calculated as described earlier and the effective p(O_2) was calculated by Equation 2.28. As a simplification of the impedance model, we assumed homogeneous overpotential within the porous LSF. The good agreement of the chemical capacitance and the effective ionic conductivity in p(O_2) and bias measurement cycles suggests that this simplification is valid. As expected, the chemical capacitance increased with decreasing oxygen partial pressure (or increasing cathodic bias) until it reached its maximum at around 10^{-5} bar. Considering that the chemical capacitance is governed by the concentration of the minority charge carrier (see Equation 2.17), the course of the chemical capacitance can be understood. At high oxygen partial pressures, the minority charge carriers are oxygen vacancies. With decreasing oxygen partial pressure their concentration rises until they become the majority charge carrier at an oxygen partial pressure around 10^{-5} bar, as can be seen in the Brouwer diagram (Figure 2.2). At even lower partial pressures, the chemical capacitance is governed by the concentration of electron holes that is declining with decreasing oxygen partial pressure, hence the decreasing chemical capacitance. The effective ionic conductivity was rather constant at high oxygen partial pressures and showed a strong increase transitioning to low pressures, in agreement with the increasing
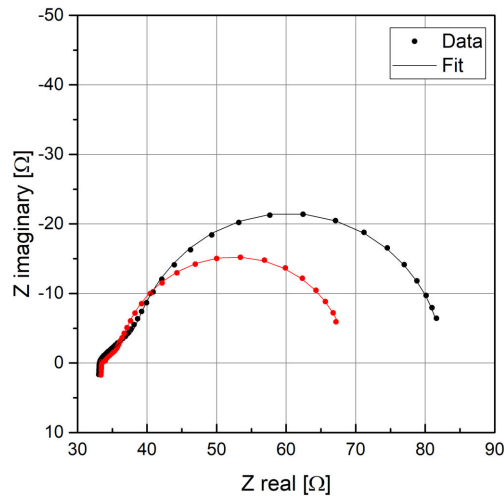
54

Figure 4.25: Example impedance spectra of LSF half cell of the LSF three-electrode sample with Pt/YSZ counter electrode including transmission line fit according to section 2.3.3. The black data was measured at a p(O_2) of $2 * 10^{-3}$ bar without bias, the red data at an effective p(O_2) of $1.79 * 10^{-4}$ bar and with an overpotential of -78 mV.

oxygen vacancy concentration.

The measurements at 750°C were conducted in a frequency range of 10^6 to 10^{-2} Hz. Again, a plausibility check was performed before starting the measurement, see Figure 4.27. Apart from an offset of about 2 Ω, the sum spectrum of the two half cells and the full cell (two-electrode) spectrum coincided. The source of the offset was of a metrological cause. Both half cell spectra were measured in 4-point configuration, whereas the full cell spectrum was measured in 2-point configuration. Therefore, the full cell spectrum included the resistance of the measuring cables which explained the offset. Figure 4.28 shows the individual spectra of the LSF and Pt/YSZ half cells. While the LSF half cell only showed a small intermediate frequency artifact loop, the spectrum of the Pt/YSZ half cell had a low frequency inductive artifact of the same size as the electrode feature. The peak frequencies of the artifact features corresponded to the peak frequency of the respective not measured half cell.

The measured LSF half cell spectra with applied bias voltage are presented in Figure 4.29. The spectra showed a high frequency inductive loop artifact, followed by a 45° slope and a dominant low frequency feature. With anodic bias, the main feature got more depressed and its peak frequency increased (10 Hz at +160 mV effective overpotential). Apart from that, the inductive loop artifact changed into a shoulder starting with an applied bias voltage of +200 mV. Cathodic bias led to shorter 45° slopes and lower peak frequencies of the dominant features (0.25 Hz

(a) Electrode resistance, p(O₂) cycles

(b) Electrode resistance, bias cycles

(c) Chemical capacitance
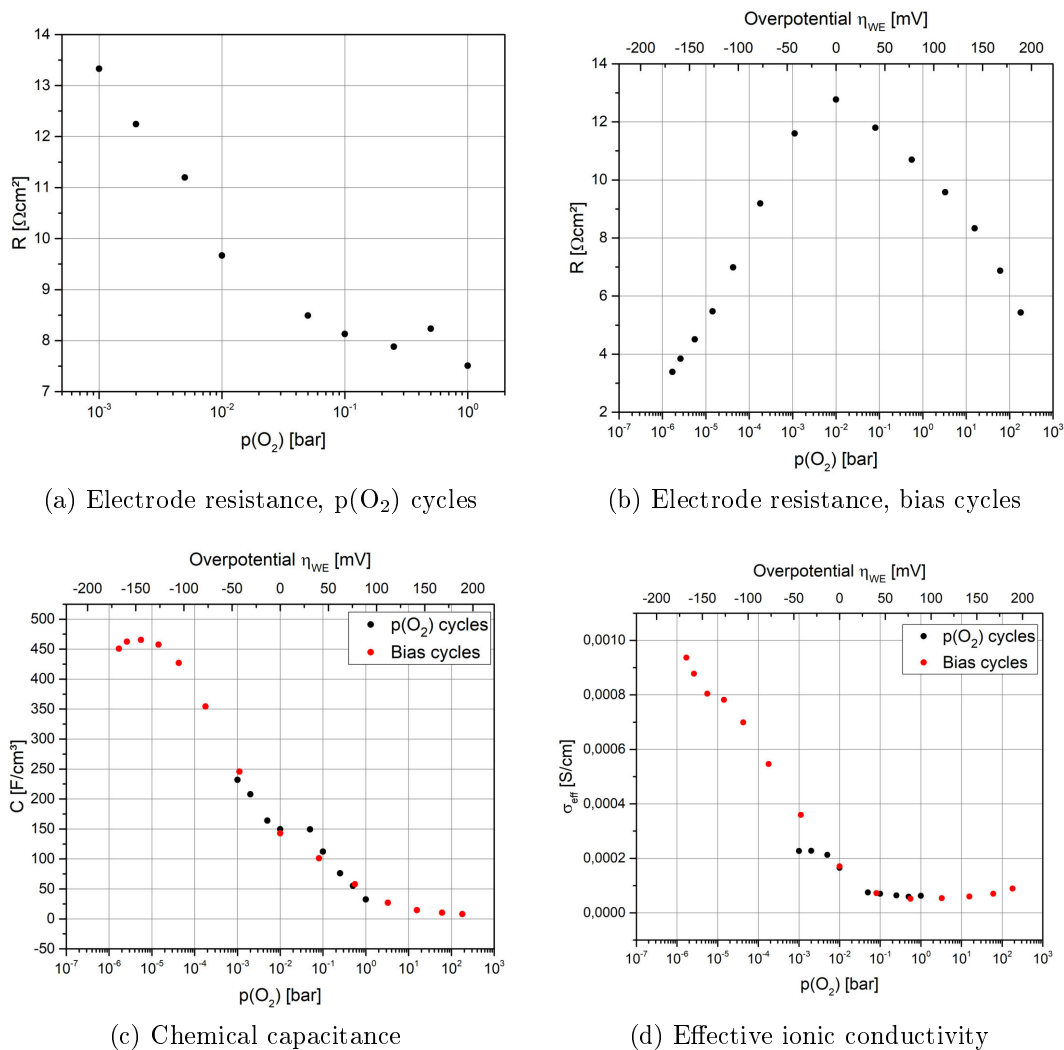

(d) Effective ionic conductivity

Figure 4.26: Resistance, chemical capacitance and ionic conductivity of LSF half cell of the LSF three-electrode sample with Pt/YSZ counter electrode obtained with $p(O_2)$ and bias cycles at a set temperature of 650°C. Inset (a) and inset (b) depict the resistance from the $p(O_2)$ and bias cycles, respectively. Inset (c) shows a comparison of the chemical capacitance of the two cycles, inset (d) the effective ionic conductivity. Oxygen partial pressures with applied bias voltage were calculated from the effective overpotential of the working electrode.

at -150 mV effective overpotential), indicative for higher ionic conductivity and chemical capacitance. This is expected from the materials defect chemistry. Also, the inductive loop got more pronounced with increasing negative bias voltage.
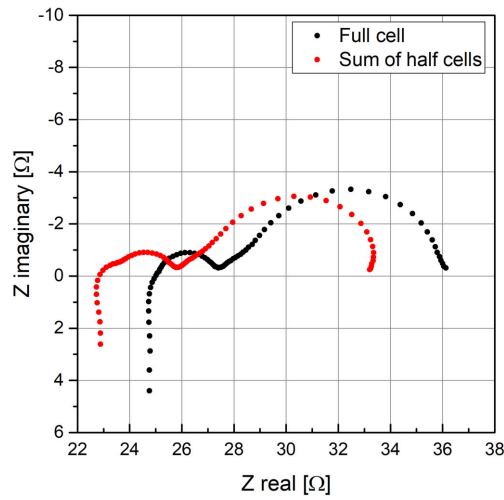
Figure 4.27: Comparison between the impedance spectrum of the full cell and the sum spectrum of both half cells of LSF three-electrode sample with Pt/YSZ counter electrode, obtained in 1% O_2 around 700°C

(a) Half cell spectra

(b) Half cell spectra, zoom-in
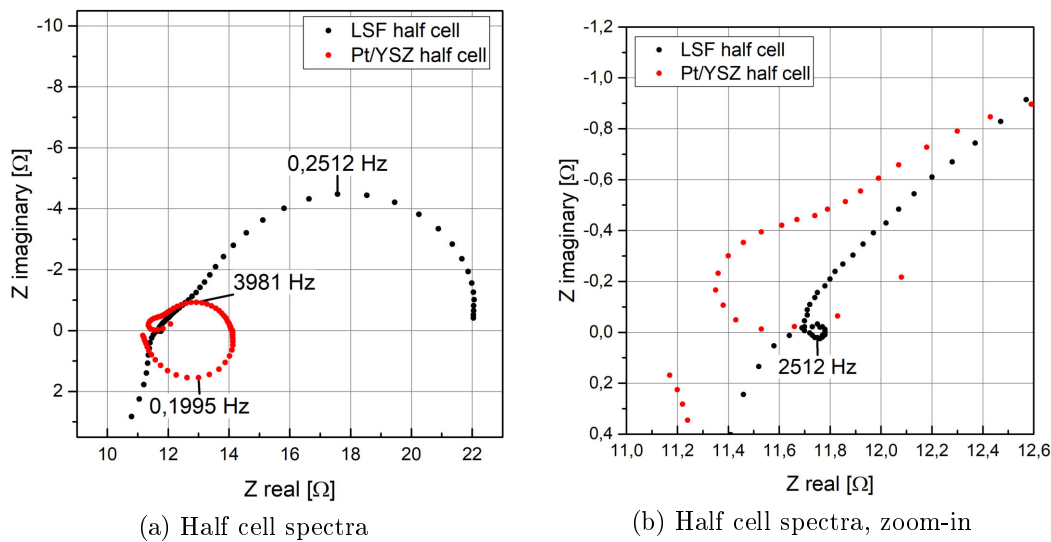
Figure 4.28: Half cell impedance spectra of LSF three-electrode sample with Pt/YSZ counter electrode measured in 1% O_2 around 700°C. The peak frequencies of the main electrode features and the inductive artifacts are marked.

The LSF half cell spectra obtained in different atmospheres showed similar behavior as the bias spectra, see Figure 4.30. High oxygen partial pressure resulted in a high frequency shoulder (without inductive loop), followed by an extended 45°

slope and a depressed low frequency feature. Lowering the oxygen partial pressure led to the formation of the high frequency inductive loop, a shorter 45° slope and a more pronounced dominant feature with lower peak frequency.

The data was fitted with the same transmission line equivalent circuit used for fitting of the spectra measured at 650°C. Under anodic bias, fitting was only possible until an applied bias voltage of +500 mV, corresponding to about 160 mV effective overpotential. Above that the fit did not produce satisfying results. With changing atmospheres, the fit was possible until a oxygen partial pressure of 250 mbar. Higher oxygen partial pressures led to very low reaction resistances R_{react} combined with high ionic transport resistances R_{ion}. As a consequence, the electrochemically active length λ, defined as $\sqrt{\dfrac{R_{react}}{R_{ion}}}$ at $\omega \to 0$, was significantly lower than the geometrical thickness of the electrode. This resulted in an over-parametrisation of the fit, which was therefore not possible without restrictions [42]. In order to fit the data at high oxygen partial pressures, one parameter had to be calculated with a different method: The ionic transport resistance was fitted to the data obtained from the bias voltage measurements with

$$\sigma_{ion} \sim p(O_2)^{-x} \longrightarrow log(R_{ion}) \sim x * log(p(O_2)) \qquad (4.6)$$

where σ_{ion} is the ionic conductivity. The fit revealed a scaling of the ionic transport resistance of $R_{ion} \sim p(O_2)^{0.21}$. This exponent is significantly lower than 0.5, which is expected from the defect chemical model of LSF, in which $[V_O^{\bullet\bullet}] \sim p(O_2)^{-0.5}$ at high oxygen partial pressure [31]. However, R_{ion} was interpolated for higher oxygen partial pressures with the above relation, allowing a fit of the impedance data with the transmission line circuit.

The fitting results are presented in Figure 4.31. The electrode resistance showed similar behavior to the measurements at 650°C: decreasing with increasing oxygen partial pressure for the $p(O_2)$ cycles and a maximum at zero bias voltage for the bias cycles. The chemical capacitance increased with decreasing oxygen partial pressure until it reached a maximum at around 10^{-4} bar. Measurements in different atmospheres and under bias voltage showed similar scaling but a minor offset concerning the chemical capacitance. The effective ionic conductivity was almost independent of the oxygen partial pressure at high pressures and showed a steep increase towards the lower pressure regime. Data from the $p(O_2)$ cycles showed good agreement with the bias cycles at high oxygen partial pressures, but included a decrease of the ionic conductivity at intermediate oxygen partial pressures that was not visible in the bias data. A similar course of the ionic conductivity, obtained from the $p(O_2)$ cycles at 650°C, can be seen in Figure 4.26. A possible reason for this behavior is the limited gas diffusion due to the low oxygen partial pressure in the gas atmosphere.

(a) Anodic bias

(b) Anodic bias, zoom-in
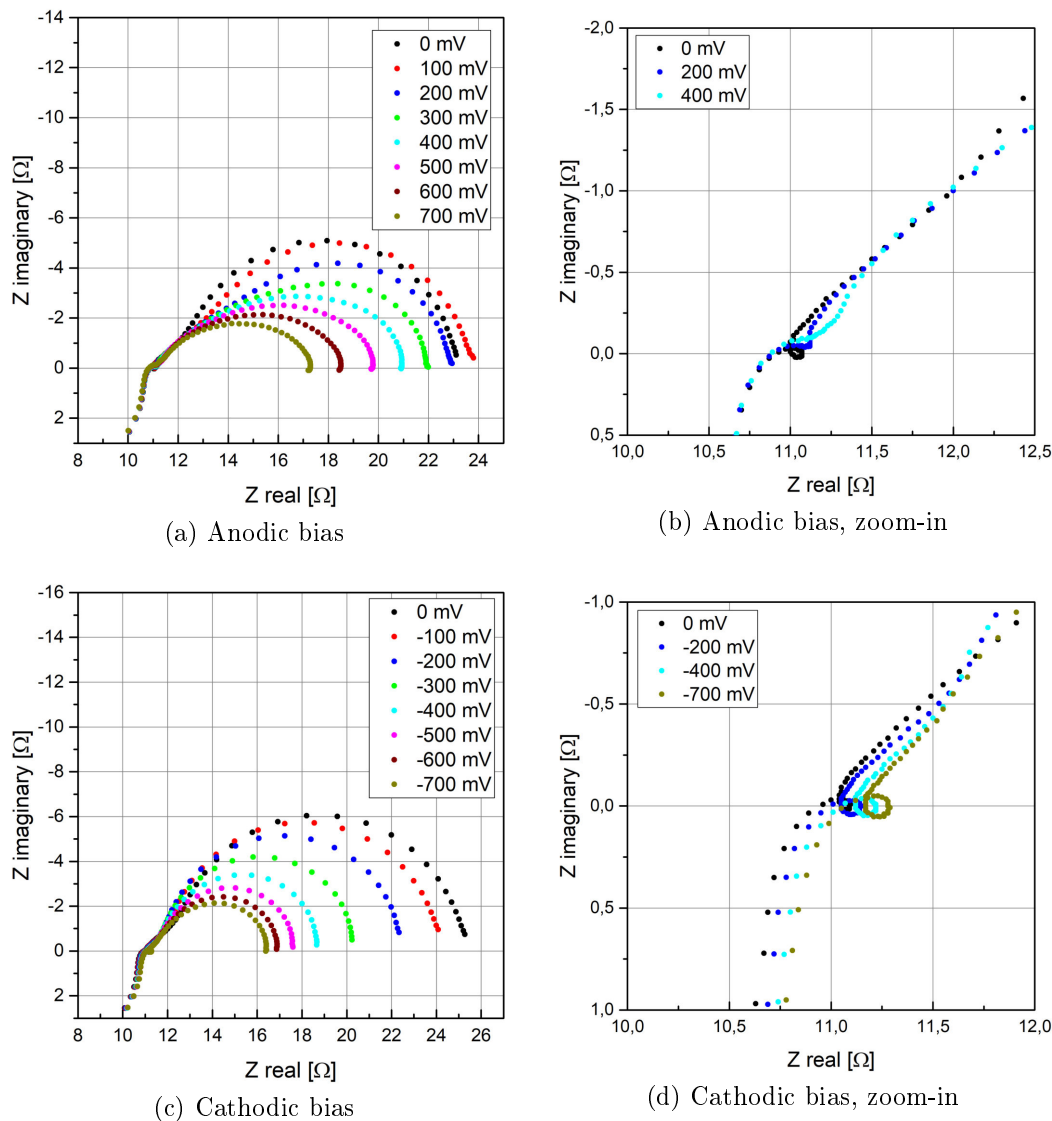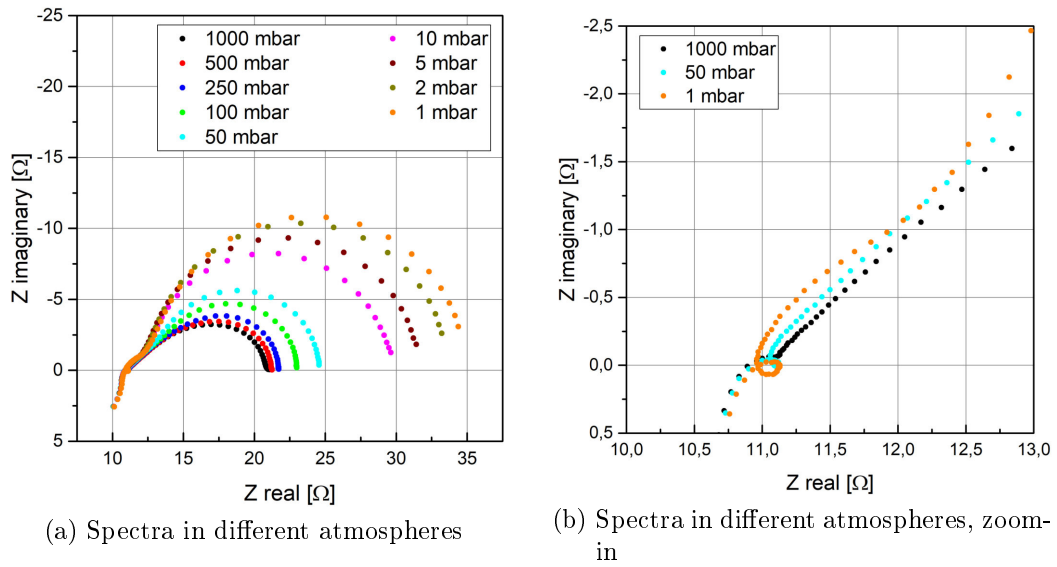
(c) Cathodic bias

(d) Cathodic bias, zoom-in

Figure 4.29: Impedance spectra of LSF half cell of the LSF three-electrode sample with Pt/YSZ counter electrode measured at 750°C set temperature in 1% O_2 under different bias voltages

Figure 4.32 shows the current-voltage characteristic of the LSF half cell at 650°C and 750°C. As expected, the course is steeper at higher temperatures, corresponding to lower electrode resistances. The resistances under cathodic bias were smaller as under anodic bias, resulting in a higher maximum cathodic current.

Before the measurements in reducing conditions were started, the plausibility check was performed. Figure 4.33 shows the spectra of the LSF and the Pt/YSZ

(a) Spectra in different atmospheres

(b) Spectra in different atmospheres, zoom-in

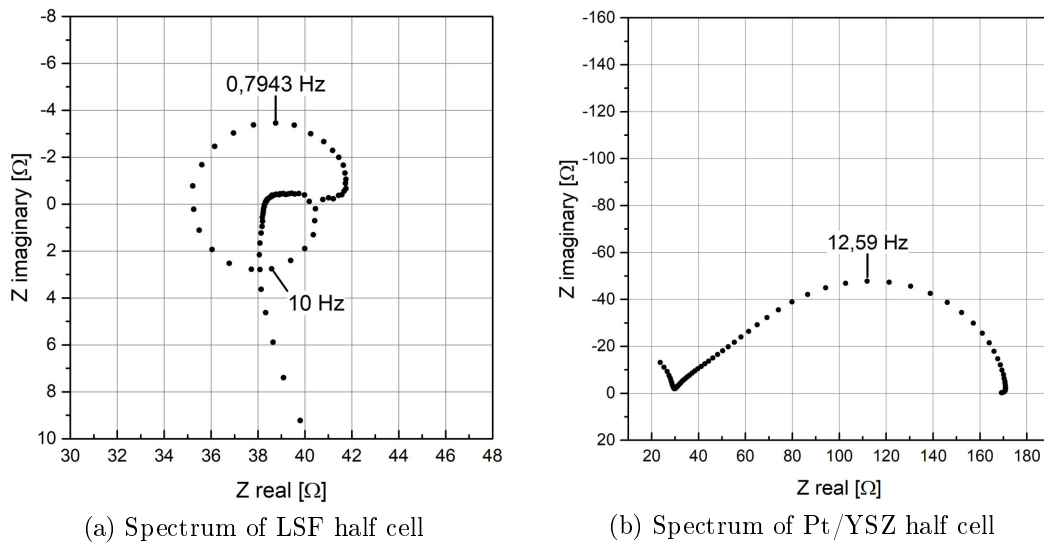Figure 4.30: Impedance spectra of LSF half cell of the LSF three-electrode sample with Pt/YSZ counter electrode measured at 750°C set temperature and different oxygen partial pressures

half cell in humidified 2.5% hydrogen in argon around 615°C. Contrary to the measurements in oxidizing atmosphere, the spectrum of the LSF half cell was heavily influenced by artifacts, whereas the Pt/YSZ impedance showed no visible artifact. The intermediate frequency inductive artifact of the LSF spectrum had approximately the same peak frequency as the main feature of the Pt/YSZ electrode, analogue to the artifacts observed in oxidizing conditions. As the electrode resistance of the Pt/YSZ electrode was significantly larger than in oxidizing conditions, so was the size of the artifact. Apart from that, the artifact was not separated from the main electrode feature which made a meaningful equivalent circuit fit impossible. Therefore, measurements in reducing atmospheres were not possible with the combination of these two electrode materials, as Pt/YSZ was not suitable as counter electrode for kinetically fast electrodes in reducing atmospheres. Interestingly, the magnitude of the Pt/YSZ CE artifact is about 1/20 of the CE polarization resistance in both atmospheres.

(a) Electrode resistance, p(O$_2$) cycles

(b) Electrode resistance, bias cycles

(c) Chemical capacitance

(d) Effective ionic conductivity
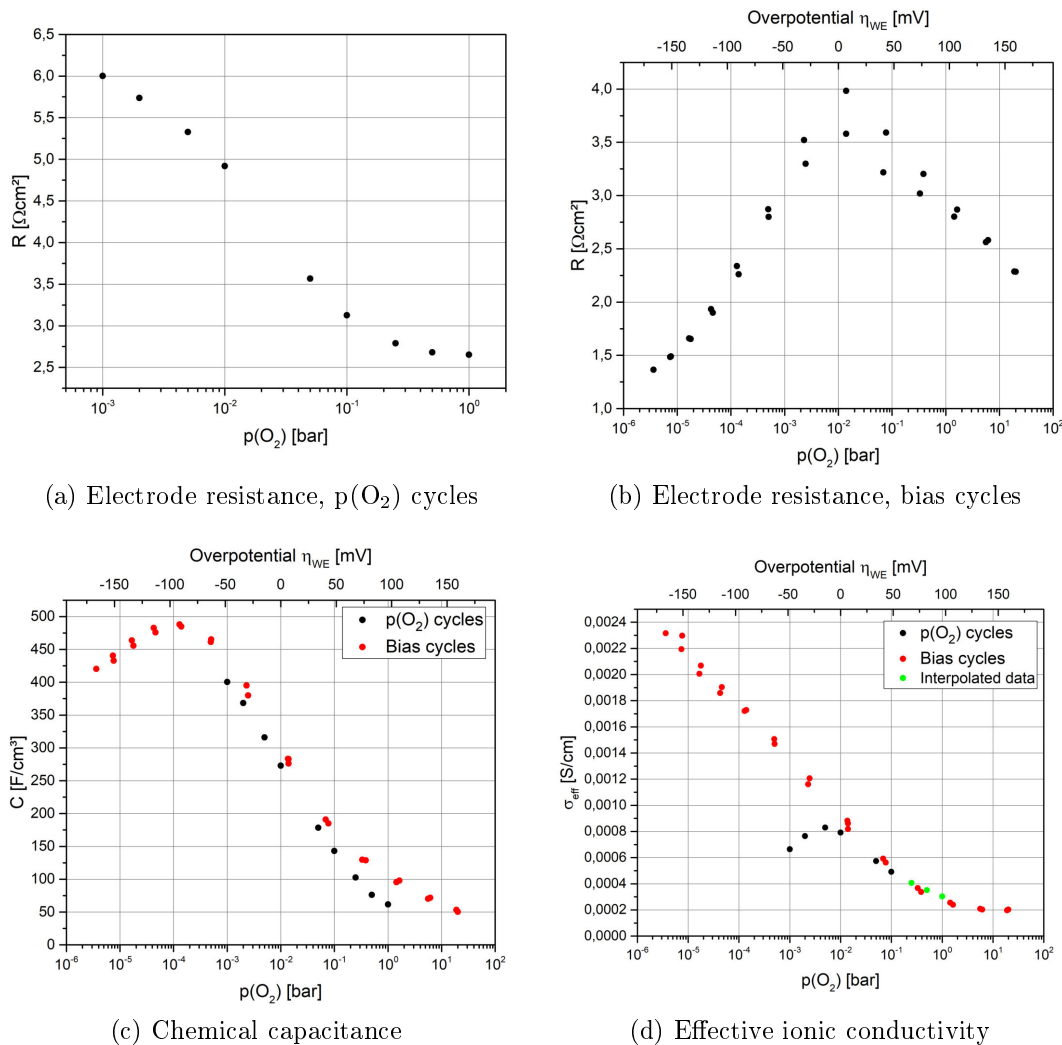
Figure 4.31: Resistance, chemical capacitance and ionic conductivity of LSF half cell of the LSF three-electrode sample with Pt/YSZ counter electrode obtained with p(O$_2$) and bias cycles at a set temperature of 750°C. Inset (a) and inset (b) depict the resistance from the p(O$_2$) and bias cycles, respectively. Inset (c) shows a comparison of the chemical capacitance of the two cycles, inset (d) the effective ionic conductivity. The interpolated values of the ionic conductivity, needed as a constraint for the fit at high oxygen partial pressures, are depicted in green. Oxygen partial pressures with applied bias voltage were calculated from the effective overpotential of the working electrode.
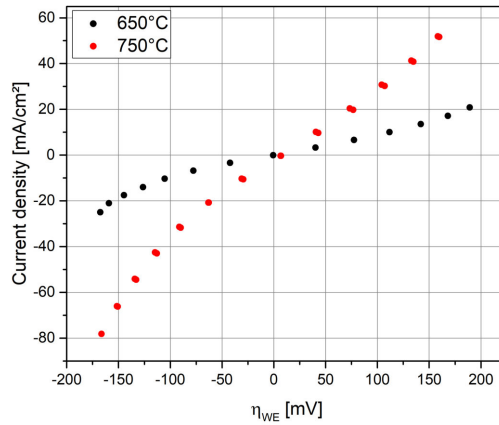
Figure 4.32: Current-voltage characteristic of LSF half cell of the LSF three-electrode sample with Pt/YSZ counter electrode measured in 1% O_2 at 650°C and 750°C set temperature

(a) Spectrum of LSF half cell
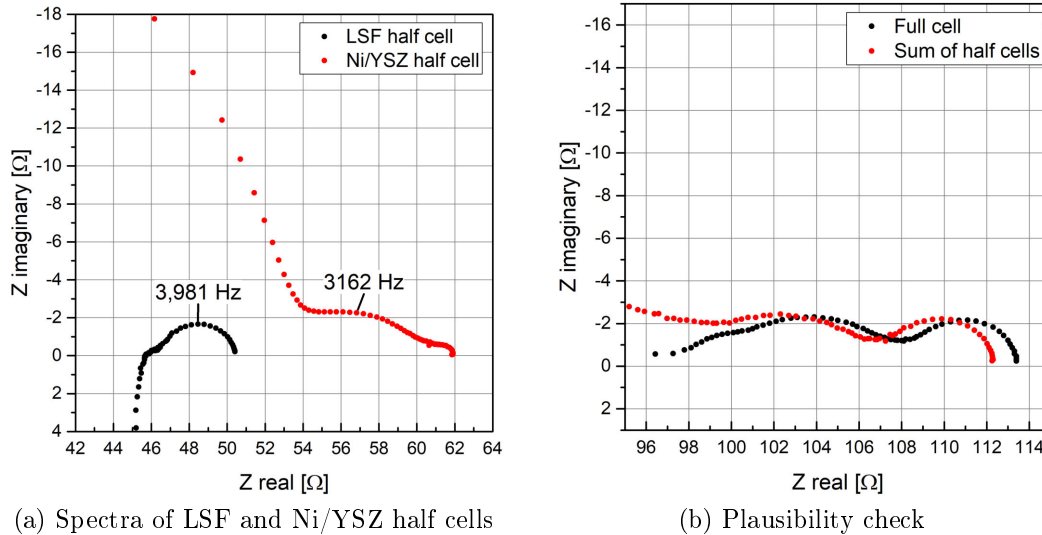
(b) Spectrum of Pt/YSZ half cell

Figure 4.33: Half cell impedance spectra of LSF three-electrode sample with Pt/YSZ counter electrode measured in humidified 2.5% hydrogen in argon around 615°C. The peak frequencies of the main electrode features and the inductive artifact are marked.

4.2.2 LSF with Ni/YSZ

As the measurements on the LSF sample with the Pt/YSZ counter electrode did not work in reducing conditions due to an incompatibility of electrode kinetics (electrode resistances) and characteristic frequencies, a different counter electrode

was used. Ni/YSZ is the standard SOFC anode electrode material and exhibits fast kinetics combined with a high peak frequency of the main electrode feature, see Figure 4.34a. The material was therefore chosen as a promising counter electrode for LSF in reducing conditions.

The Ni/YSZ counter electrode was produced by screen printing of commercial NiO/YSZ paste (Heraeus, Germany), consisting of 60 Vol% NiO and 40 Vol% YSZ, on the electrolyte substrate, followed by a layer of pure NiO as current collector. For the reference electrode, NiO/YSZ and NiO paste were brushed on the wing. During the heating of the sample in reducing atmospheres, NiO is reduced to Ni resulting in a decrease of size which creates the needed porosity.

Before the measurements on the sample were started, the plausibility check was performed, see Figure 4.34b. Similar to previous plausibility checks, the spectra coincided apart from a slight offset of $1.5\,\Omega$ between the spectra that was caused by the resistance of the measuring cables on the two-electrode full cell measurement. In the high frequency regime however, the two spectra did not coincide. This divergence was caused by capacitive currents through the measuring line of the reference electrode due to a grounded shield of the BNC cable. As can be seen in Figure 4.34a these currents led to vast high frequency artifacts which did not fully cancel out when adding up the half cell spectra. Since the artifacts did not interfere with the main electrode feature, they did not impede the measurement.

(a) Spectra of LSF and Ni/YSZ half cells   (b) Plausibility check

Figure 4.34: Impedance spectra of LSF three-electrode sample with Ni/YSZ counter electrode measured in humidified 2.5% hydrogen in argon around 615°C. The peak frequencies of the main electrode features are marked in inset (a).

Measurements were conducted at 650°C and 750°C in different reducing atmospheres and with applied bias voltage. The spectra were recorded between 10^6 and $2 * 10^{-2}$ Hz with an excitation voltage of 100 mV. The high excitation was chosen due to the ratio of the resistance of the LSF electrode to the electrolyte offset of 1 to 10, as only a fraction of the applied measuring voltage was effective at the electrode. The LSF half cell spectra measured at 650°C in different atmospheres are presented in Figure 4.35. All spectra showed the beginning of a vast high frequency inductive artifact semicircle that is not fully visible in the plots, as it would have compromised the visibility of the relevant part of the spectra. As it did not change shape in different atmospheres and only occurred in the high frequency part of the spectra, it was most likely caused by a capacitive current through the reference electrodes measuring line. The artifact feature was followed by an intermediate frequency shoulder and a dominant low frequency semicircle. With increasing water to hydrogen ratio, the dominant feature got more pronounced, whereas the shoulder remained uninfluenced. Increasing the hydrogen partial pressure in the atmosphere resulted in a bigger and more depressed low frequency feature. However, also the shoulder was influenced and almost disappeared into a loop at higher hydrogen partial pressures, see Figure 4.35c. Interestingly, the ohmic offset resistance also depended on the atmosphere. This can be understood from the relatively low electronic conductivity of LSF in reducing atmospheres [11], which causes an increase of the ohmic resistance that is proportional to the electronic conductivity.

The measurements with applied bias voltage were all conducted in a one-to-one ratio of hydrogen and water. Analogue to the excitation voltage, the applied bias voltage was rather high as only a fraction of it was effective at the LSF electrode. The measurement was carried out in bias cycles of 0 mV -> +2000 mV -> -2000 mV -> 0 mV. The recorded LSF half cell spectra are presented in Figure 4.36. Generally, the spectra had the same shape as those obtained in different atmospheres. However, there were differences between the individual cycles. During the first cycle with anodic bias, the dominant low frequency feature increased substantially in size with increasing bias. Apart from that, low frequency inductive artifacts were visible in the spectra. At +2000 mV applied bias voltage, a small inductive artifact was present in the spectra at the onset of the intermediate frequency shoulder. The spectra of the second anodic bias cycle did not show the strong increase of the low frequency feature with increasing bias and the intermediate frequency inductive artifact at +2000 mV was not visible. However, the low frequency inductive artifacts had the same absolute size as with the first cycle. Under cathodic bias, the size of the dominant feature was only slightly affected by the applied bias. At high negative bias, low frequency artifacts were visible. The spectra at -2000 mV differed strongly between the two measuring cycles. The spectrum of the first cycle showed a closed low frequency feature followed by a

64
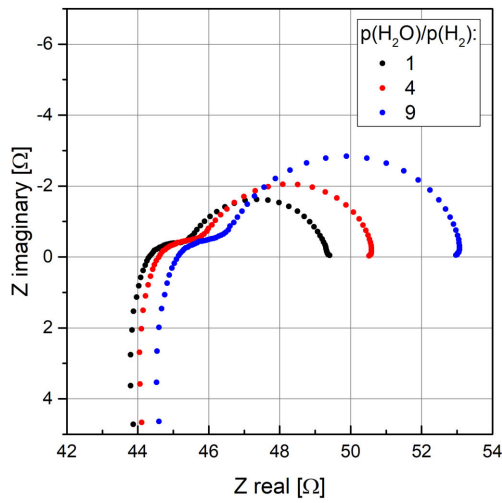
(a) Spectra in less reducing atmospheres
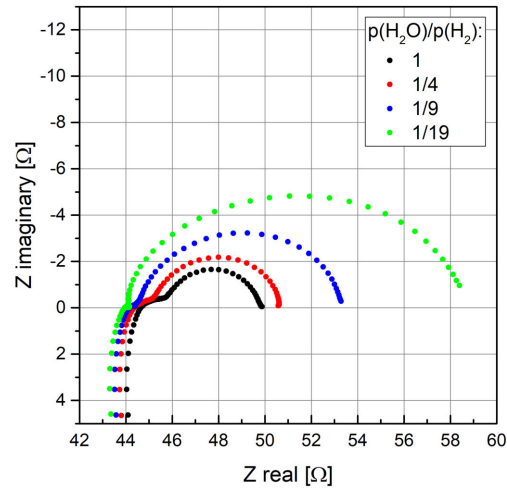
(b) Spectra in more reducing atmospheres
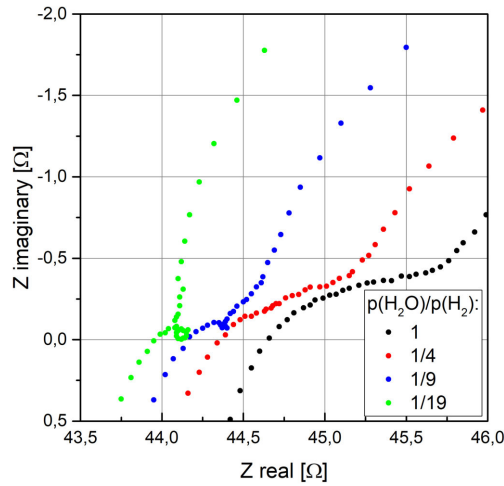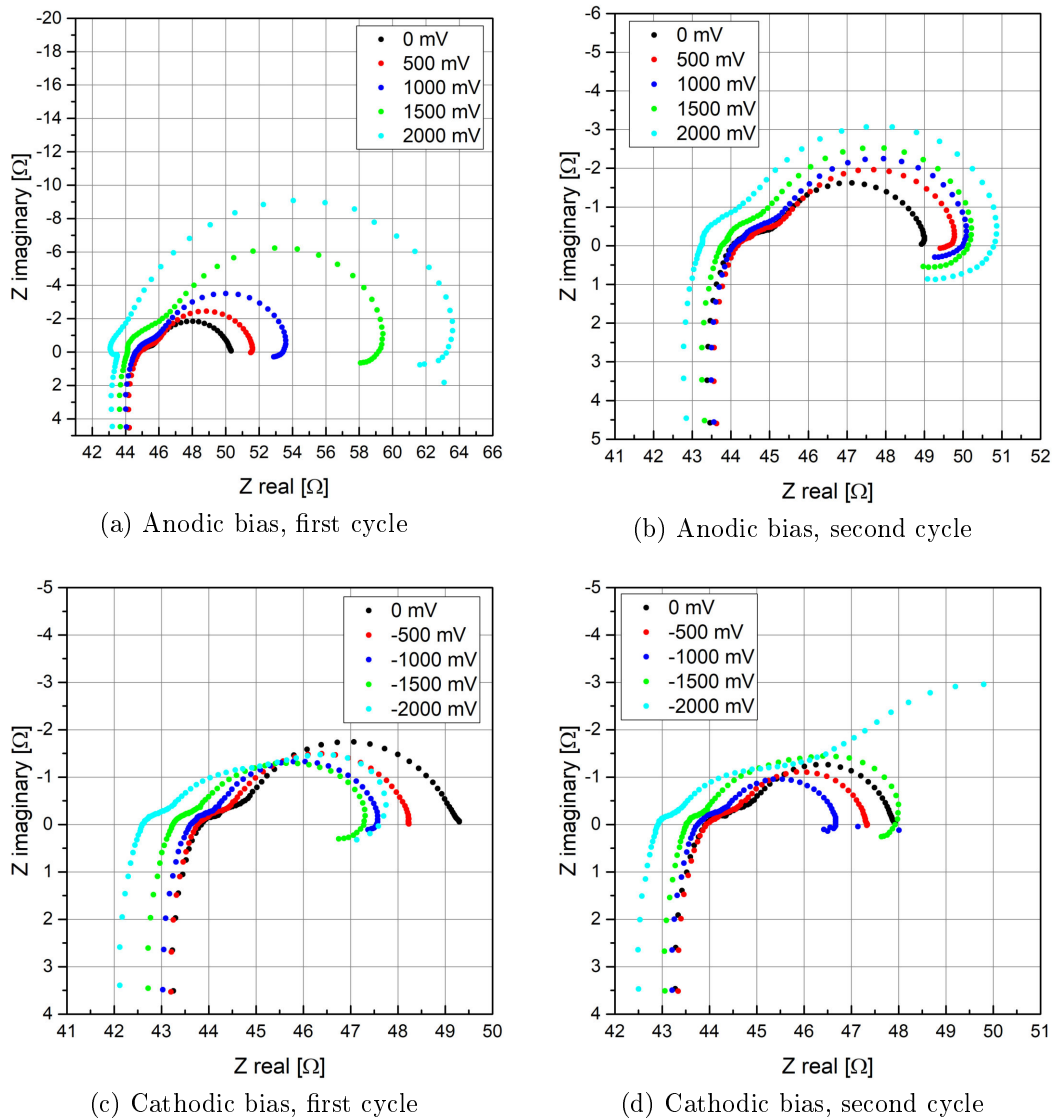

(c) Spectra in more reducing atmospheres,
zoom-in

Figure 4.35: Impedance spectra of LSF half cell of the LSF three-electrode sample with Ni/YSZ counter electrode measured in different atmospheres at 650°C set temperature. Inset (c) shows an enlargement of the high frequency part of inset (b).

small inductive artifact, whereas the spectrum of the second cycle contained an additional low frequency arc.

The spectra were all fitted with a series connection of an offset resistance and two R‖CPE elements. However, fitting of the spectra obtained at -2000 mV bias voltage was not possible with this equivalent circuit. The extracted parameters

(a) Anodic bias, first cycle

(b) Anodic bias, second cycle

(c) Cathodic bias, first cycle

(d) Cathodic bias, second cycle

Figure 4.36: Impedance spectra of LSF half cell of the LSF three-electrode sample with Ni/YSZ counter electrode measured at 650°C set temperature in humidified hydrogen in argon under different bias voltages

are presented in Figure 4.37a-c. The electrode resistance obtained in different atmospheres showed a minimum at a one-to-one ratio of water and hydrogen. It is likely that the small partial pressures of H_2 and H_2O caused rate determining gas diffusion resistances. H_2O diffusion dominates the ASR at low $p(O_2)$ and H_2 diffusion dominates at high $p(O_2)$. The chemical capacitance of the main feature increased with decreasing oxygen partial pressure. This behavior is again

in accordance with the Brouwer diagram in Figure 2.2. In this oxygen partial pressure range the minority charge carriers are electrons and their concentration increases with decreasing oxygen partial pressure, hence the chemical capacitance is also expected to increase. Comparing the results of the $p(O_2)$ cycles to the bias cycles, the chemical capacitance showed good accordance at higher oxygen partial pressures. At lower pressures, the scaling of the chemical capacitance with the oxygen partial pressure differed. When plotting the logarithm of the capacitance against the logarithm of the equivalent oxygen partial pressure and fitting the curves, one received $C_{chem} \propto p(O_2)^{-0.10}$ and $C_{chem} \propto p(O_2)^{-0.17}$ for the $p(O_2)$ and the bias cycles, respectively (see Figure 4.37d). When comparing the two bias cycles, no difference was visible considering the chemical capacitance. With the electrode resistance however, one could see the gap between the two cycles at higher oxygen partial pressures. Interestingly, 2000 mV bias voltage in the first cycle corresponded to 148 mV effective overpotential at the LSF electrode. In the second cycle, it corresponded only to 85 mV, due to a lower polarization resistance.

The current-voltage characteristic of the LSF half cell is depicted in Figure 4.38. The curve of the first cycle was asymmetric, as it flattened at higher anodic overpotential, corresponding to the increased electrode resistance. The second curve did not flatten and showed an almost linear behavior over the observed overpotential range.

The measurements at 750°C did not provide satisfying results. Starting with the first measurement in strongly reducing atmospheres, all subsequent spectra showed the same massive artifact that did not allow a meaningful interpretation of the observed spectra, see Figure 4.39. Since the artifact was in the high frequency range of the spectra, the LSF electrode was ruled out as a source for that feature as all LSF features had low characteristic frequencies. Therefore, the source of the artifact was the reference or the counter electrode. As only the LSF half cell spectrum was measured, it was not possible to identity the actual source. However, parts of the Ni/YSZ counter electrode were sintered to the Pt meshes of the sample holder and most of the electrode delaminated upon the removal of the sample. If the counter electrode started to delaminate during the measurement, this could have caused the artifact. Moreover, gas phase diffusion is expected to dominate the impedance even more at higher temperature.
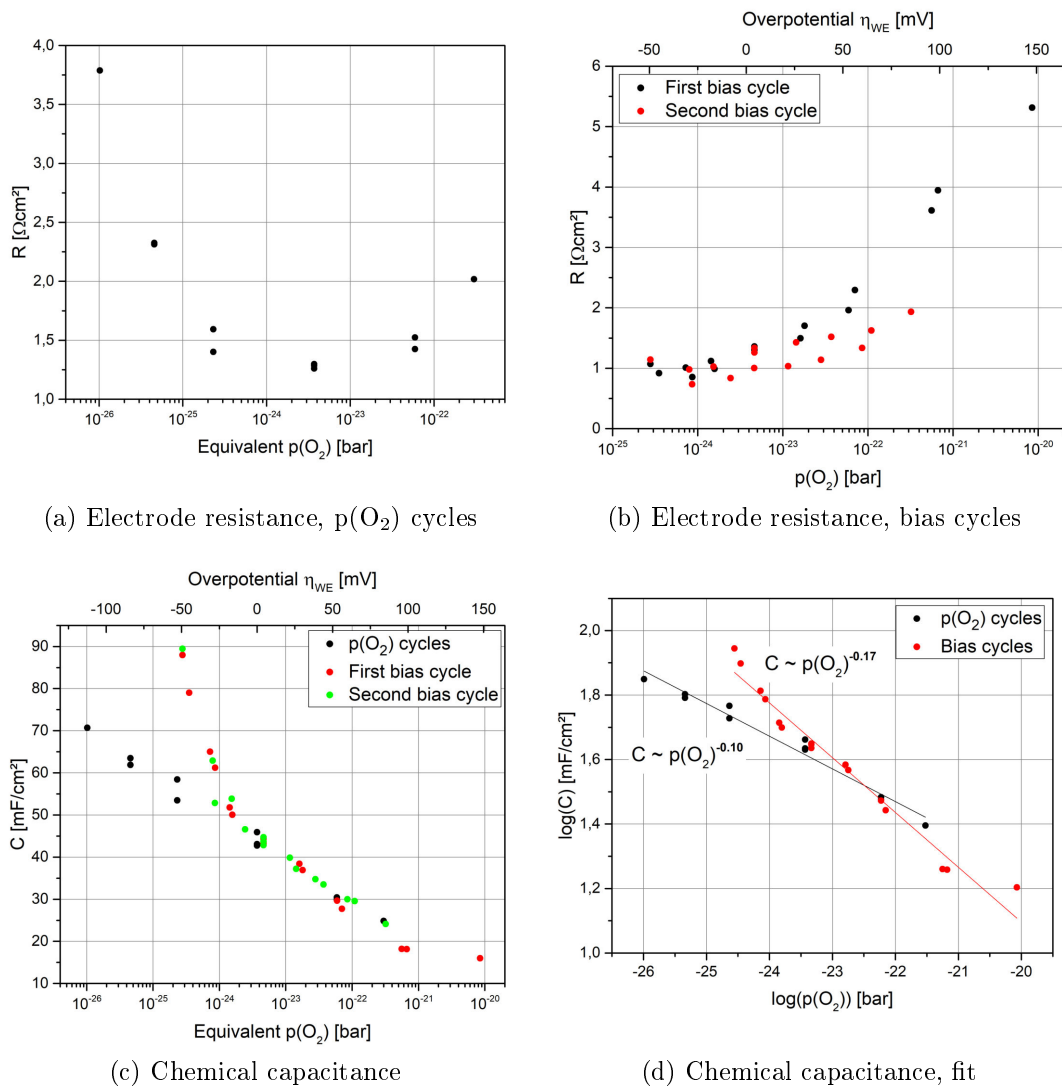
(a) Electrode resistance, p(O₂) cycles

(b) Electrode resistance, bias cycles

(c) Chemical capacitance

(d) Chemical capacitance, fit

Figure 4.37: Resistance and chemical capacitance of LSF half cell of the LSF three-electrode sample with Ni/YSZ counter electrode obtained with p(O₂) and bias cycles at a set temperature of 650°C. Inset (a) and inset (b) depict the resistance from the p(O₂) and bias cycles, respectively. Inset (c) shows a comparison of the chemical capacitance of the cycles. In inset (d) the logarithm of the chemical capacitance is fitted (thin lines) over the logarithm of the oxygen partial pressure. Oxygen partial pressures with applied bias voltage were calculated from the effective overpotential of the working electrode.
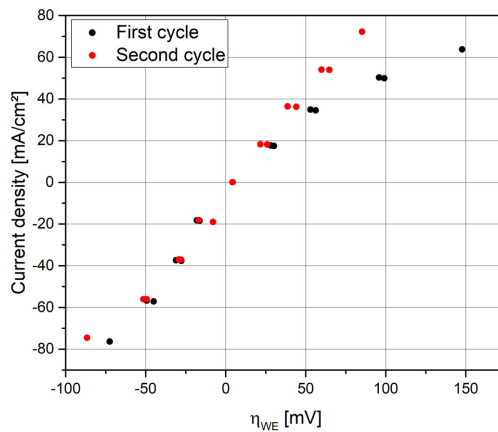
Figure 4.38: Current-voltage characteristic of the LSF half cell of the LSF three-electrode sample with Ni/YSZ counter electrode measured at 650°C set temperature in humidified hydrogen in argon.
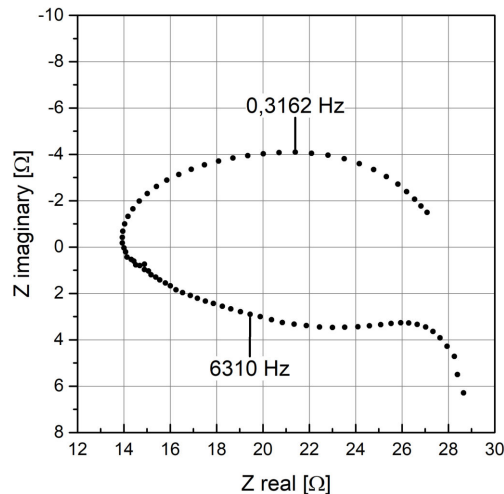
Figure 4.39: Spectrum of LSF half cell of the LSF three-electrode sample with Ni/YSZ counter electrode measured at 750°C set temperature. The ratio of $p(H_2)$ to $p(H_2O)$ was 19 to 1, corresponding to an oxygen partial pressure of around $6 * 10^{-24}$ bar.

4.2.3 GDC with Ni/YSZ

GDC has polarization resistances and peak frequencies similar to LSF in reducing atmospheres. As the sample was measured in reducing conditions only, Ni/YSZ was chosen as suitable counter electrode. The measurements were conducted in different reducing atmospheres at 650°C and 750°C set temperature and under bias

voltage. Starting with this sample, the trigger box, mentioned in subsection 3.2.2, was used for the measurements. Therefore, it was possible to measure both half cells and the full cell spectra in every measuring condition.

At the start of the measurement, a plausibility check was performed. Figure 4.40a depicts the two half cell spectra at a temperature of approximately 610°C. Similar to the spectra of the LSF sample with Ni/YSZ counter electrode, they showed vast high frequency artifacts of about the same shape and size but different sign. Following the high frequency inductive artifact, the GDC spectrum consisted of a smaller intermediate frequency inductive shoulder and a dominant low frequency semicircle. The Ni/YSZ spectrum showed an elongated intermediate frequency feature, which followed the high frequency artifact, and a low frequency inductive semicircle. The peak frequencies of the main electrode features of each half cell spectrum corresponded to the frequencies of the artifacts of the other half cell. Therefore, the artifacts were assumed to originate from the counter electrodes due to shifts in the equipotential surface of the reference electrode. As the artifacts were separated from the electrode features, they did not interfere with the measurement. The comparison of the sum of the half cell spectra with the full cell spectrum in Figure 4.40b showed good agreement over a wide frequency range. Only at high frequencies a slight deviation between the spectra was visible. This was a result of the high frequency artifacts caused by capacitive currents over the measuring line of the reference electrode.

The GDC half cell spectra measured at 650°C set temperature in different reducing atmospheres are presented in Figure 4.41a-b. All spectra showed a high frequency inductive artifact, followed by a smaller inductive artifact shoulder and a dominant low frequency semicircle. In less reducing atmospheres, the main feature changed only slightly in size. In more reducing conditions however, the low frequency feature was more pronounced and started separating into two features. Apart from that, the size of the artifact shoulder, originating from the counter electrode, increased in more reducing conditions. That increase corresponded to the spectra of the Ni/YSZ half cell that also showed larger electrode features in more reducing conditions, see Figure 4.41c. The Ni/YSZ spectra themselves developed a feature in the frequency range of about 1 Hz that increased in size in more reducing conditions. In strongly reducing conditions, the partial pressure of H_2O is very low and limited gas diffusion becomes relevant. For Ni/YSZ electrodes, gas diffusion leads to features in the range of 1 Hz [42] that are separated from the high frequency electrode feature. Therefore, the low frequency features of the Ni/YSZ spectra in strongly reducing atmospheres were identified as gas diffusion impedance. These features posed a problem since they were in the same frequency range as the GDC electrode feature. Hence, artifacts originating from the diffusion features were not separated from the GDC electrode feature and distorted the

(a) Spectra of GDC and Ni/YSZ half cells
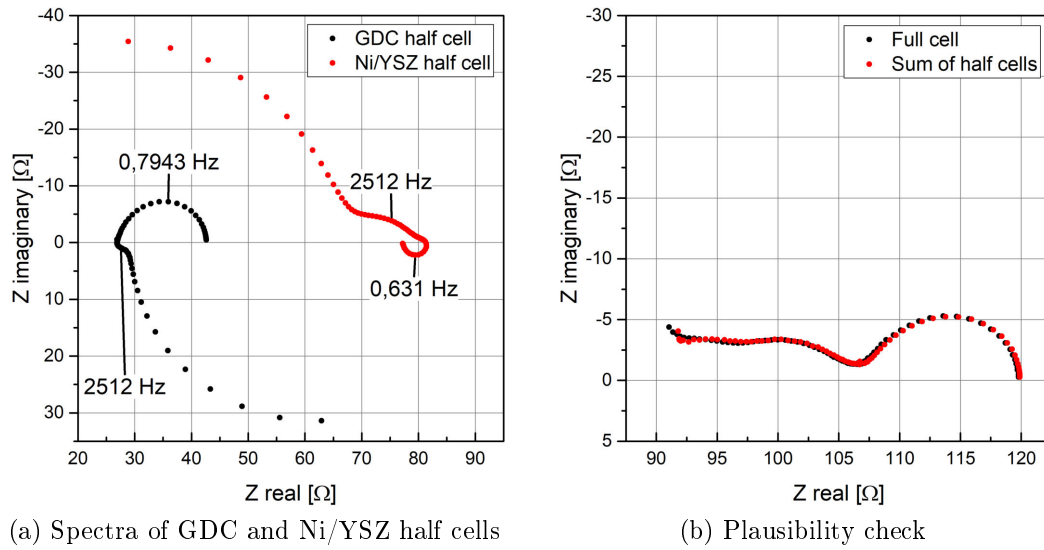

(b) Plausibility check

Figure 4.40: Impedance spectra of GDC three-electrode sample with Ni/YSZ counter electrode measured in humidified 2.5% hydrogen in argon around 610°C. The peak frequencies of the main electrode features are marked in inset (a).

spectra in a complicated way.

The bias measurements were conducted in a one-to-one ratio of hydrogen and water with applied bias voltages from -800 mV to +800 mV. The recorded GDC half cell spectra are presented in Figure 4.42. The shape of the spectra was similar to those recorded in different atmospheres. Positive bias voltage led to a decrease of the size of the dominant feature and to the appearance of a low frequency inductive artifact. Under negative bias, the dominant feature increased in size and started separating into two features. However, the newly formed feature was an approximately 45° slope, contrary to the measurements in changing atmospheres where the new feature was a not fully separated semicircle.

The GDC spectra were fitted with a series connection of a resistor and one or two R||CPE elements. Two R||CPE elements were needed for the spectra in strongly reducing atmospheres and with high cathodic bias voltage to produce a satisfying fit. The extracted parameters are presented in Figure 4.43. The electrode resistance showed a minimum around a one-to-one ratio of water and hydrogen and a strong increase with more reducing conditions. At higher oxygen partial pressures, the increase was less distinct. Since the ASR values were much higher than for LSF, gas diffusion was most likely not rate limiting. With applied bias voltage, the electrode resistance decreased with anodic bias and increased with cathodic bias until it reached a maximum around -70 mV effective overpotential at

71

(a) GDC spectra in less reducing atmospheres

(b) GDC spectra in more reducing atmospheres
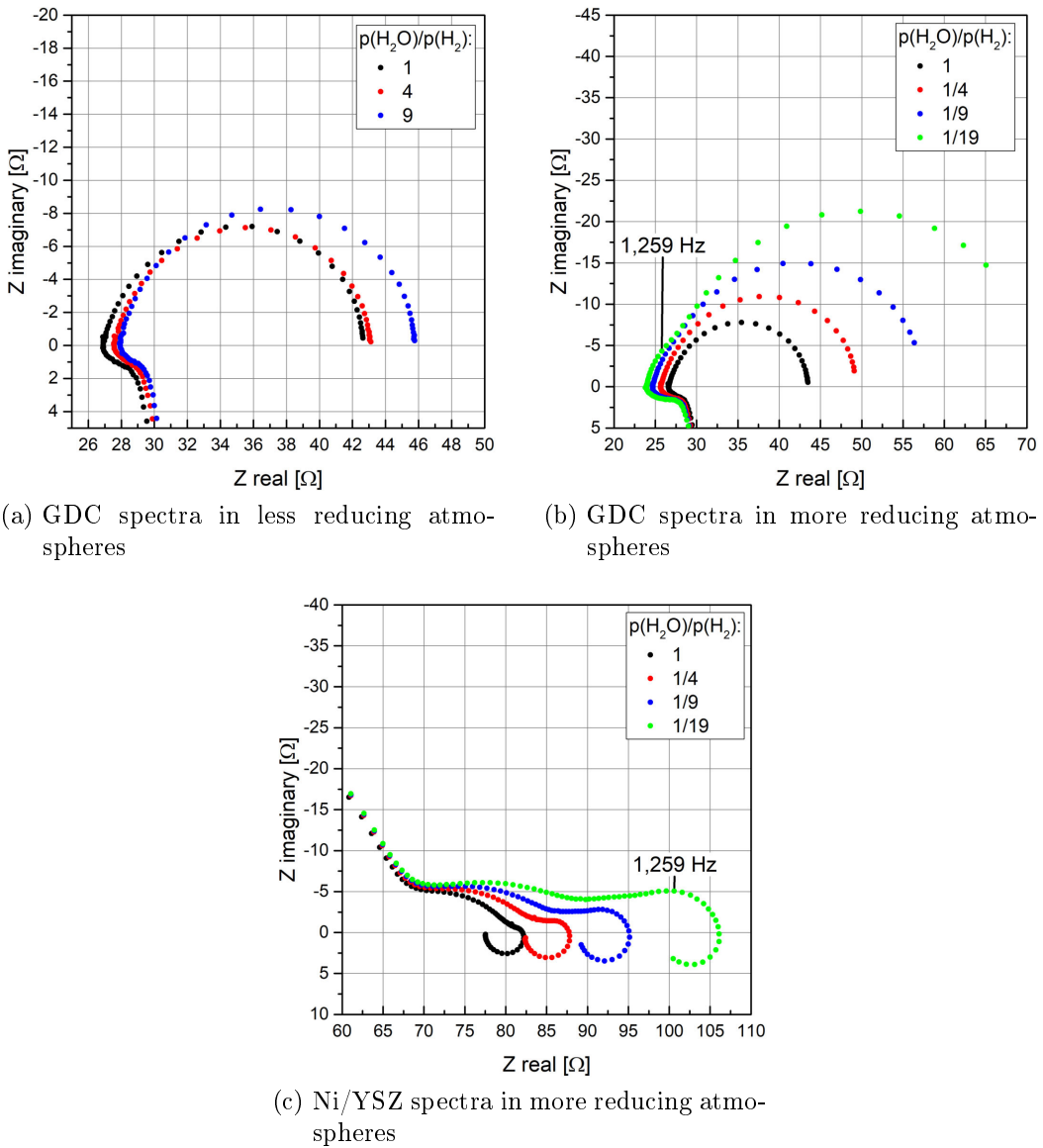

(c) Ni/YSZ spectra in more reducing atmospheres

Figure 4.41: Impedance spectra of GDC three-electrode sample with Ni/YSZ counter electrode measured in different atmospheres at 650°C set temperature. Inset (a) and (b) show spectra of the GDC half cell, inset (c) spectra of the Ni/YSZ half cell.

the working electrode. The chemical capacitance showed a strong increase at lower oxygen partial pressures and flattened at higher pressures, with good coincidence between the different measuring cycles. The fitting of the chemical capacitance revealed a scaling with the oxygen partial pressure given by

(a) Anodic bias

(b) Cathodic bias
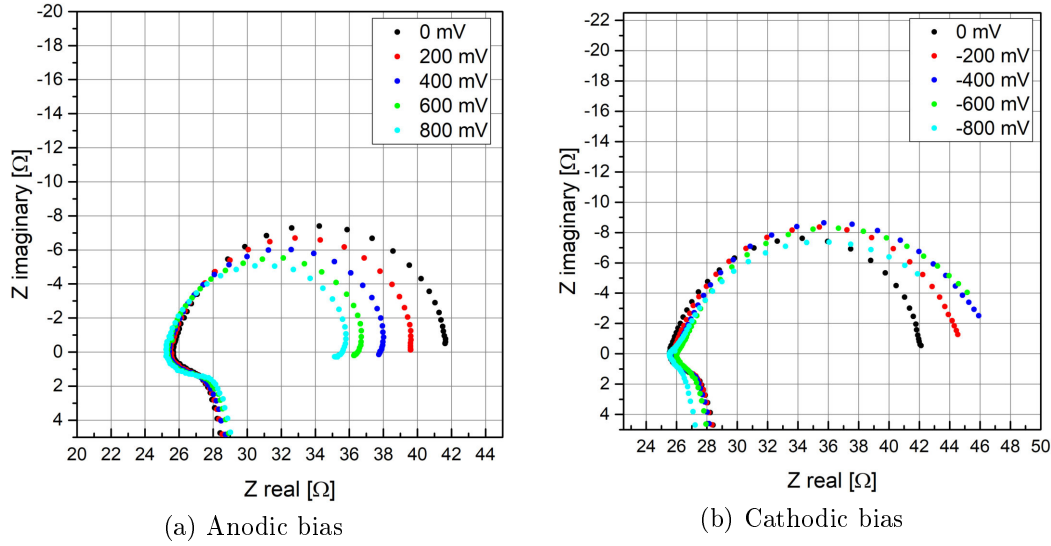
Figure 4.42: Impedance spectra of GDC half cell of the GDC three-electrode sample with Ni/YSZ counter electrode measured at 650°C set temperature in humidified hydrogen in argon under different bias voltages

$C_{chem} \propto p(O_2)^{-0.26}$. That was approximately the same scaling as with the GDC thin film in Figure 4.21c.

Considering the oxygen exchange reaction of GDC (Equation 2.19), the equilibrium constant of this reaction can be written as

$$K = \frac{[Ce_{Ce}^{\times}]^2 * [O_O^{\times}]}{[Ce_{Ce}^{'}]^2 * [V_O^{\bullet\bullet}] * \sqrt{p(O_2)}} \tag{4.7}$$

where terms in square brackets represent concentrations. In reducing conditions and the dilute limit, the concentration of oxygen vacancies and the concentrations of oxygen and Ce^{4+} in the lattice are much greater than the concentration of electronic defects and can therefore be approximated as constant when considering changes in the oxygen partial pressure. Thus, the electron concentration c_{eon} (represented by $[Ce_{Ce}^{'}]$) can be written as:

$$c_{eon} \propto p(O_2)^{-\frac{1}{4}}. \tag{4.8}$$

As the chemical capacitance is given by Equation 2.17 and dominated by the minority charge carrier, a scaling of the chemical capacitance with $p(O_2)^{-\frac{1}{4}}$ is expected [32]. Therefore, meaningful results can be obtained with three-electrode measurements, even if artifacts are present in the spectra. Analogous measurements were carried out also at 750°C set temperature.

73

(a) Electrode resistance, p(O₂) cycles

(b) Electrode resistance, bias cycles

(c) Chemical capacitance

(d) Chemical capacitance, fit
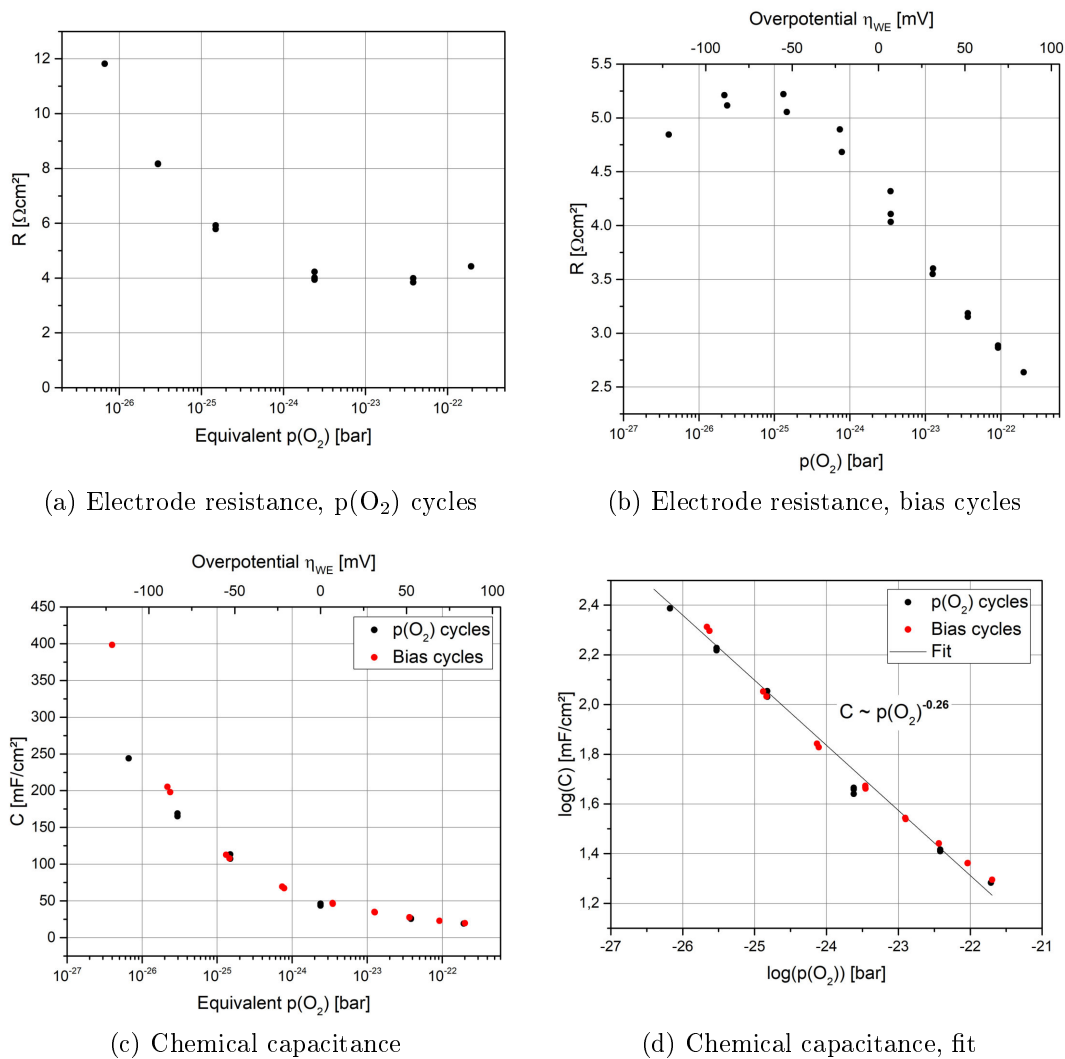
Figure 4.43: Resistance and chemical capacitance of GDC half cell of the GDC three-electrode sample with Ni/YSZ counter electrode obtained with p(O₂) and bias cycles at a set temperature of 650°C. Inset (a) and inset (b) depict the resistance from the p(O₂) and bias cycles, respectively. Inset (c) shows a comparison of the chemical capacitance of the cycles. In inset (d) the logarithm of the chemical capacitance is fitted over the logarithm of the oxygen partial pressure. Oxygen partial pressures with applied bias voltage were calculated from the effective overpotential of the working electrode.

The spectra measured at 750°C set temperature in different atmospheres are presented in Figure 4.44. Again, all spectra showed a high frequency inductive artifact that was not influenced by different atmospheres. However, the artifact was less pronounced than with the measurements at 650°C set temperature. Following the high frequency artifact, all spectra showed an intermediate frequency inductive shoulder and a dominant low frequency semicircle. Less reducing conditions did not change the shape of the spectra, but led to a small increase of the electrode resistance. Increasing the hydrogen partial pressure resulted in a more pronounced dominant feature that, in accordance to the spectra obtained at 650°C, separated into two distinguishable features. Also the size of the inductive artifact shoulder increased in more reducing atmospheres, corresponding to an increase of the electrode feature of the Ni/YSZ counter electrode. Figure 4.44c depicts the spectra of the half cells, the full cell and the sum of the half cells at a ratio of $p(H_2O)$ to $p(H_2)$ of 1 to 19. The Ni/YSZ spectra again showed a diffusion feature in the range of 1 Hz that influenced the spectra of the GDC half cell. As the gas diffusion feature was only weakly thermally activated, the impact on the spectra was more severe at higher temperatures.

The spectra with applied bias voltage are presented in Figure 4.45. Anodic bias had almost no influence on the shape of the spectra, but led to an increase of the offset resistance. However, at +800 mV applied bias voltage the Ni/YSZ half cell had a dominant low frequency feature in the same frequency range as the GDC half cell, see Figure 4.45c. Therefore, artifacts resulting from that feature would not be visible in the spectrum of the GDC half cell. Applying cathodic bias on the other hand, led to a decreased offset resistance and to the separation of the dominant low frequency semicircle into two features. Again, the feature was a 45° slope and not as pronounced as the additional feature in changing atmospheres. The changes in the offset resistance were not observed in any of the previous measurements. As the offset resistance of the Ni/YSZ half cell was considerably bigger than the offset resistance of the GDC half cell, the changes were identified to originate from the Ni/YSZ electrode due to an additional contact resistance. This contact resistance could be caused by the partial delamination of the Ni current collector that readily sintered to the Pt meshes.

After applying -800 mV bias voltage, all subsequent spectra showed a vast high frequency artifact feature, see Figure 4.45d. The artifact bore a strong resemblance to the artifact of the LSF three-electrode sample with Ni/YSZ counter electrode that appeared after the first measurement in strongly reducing atmospheres (Figure 4.39). In the spectra of the Ni/YSZ half cell, an artifact of similar size and shape appeared in the capacitive half of the complex impedance plane. However, comparing the full cell spectra from before and after applying -800 mV bias voltage revealed almost identical shapes. Hence, the Ni/YSZ electrode was ruled out as

(a) GDC spectra in less reducing atmospheres

(b) GDC spectra in more reducing atmospheres
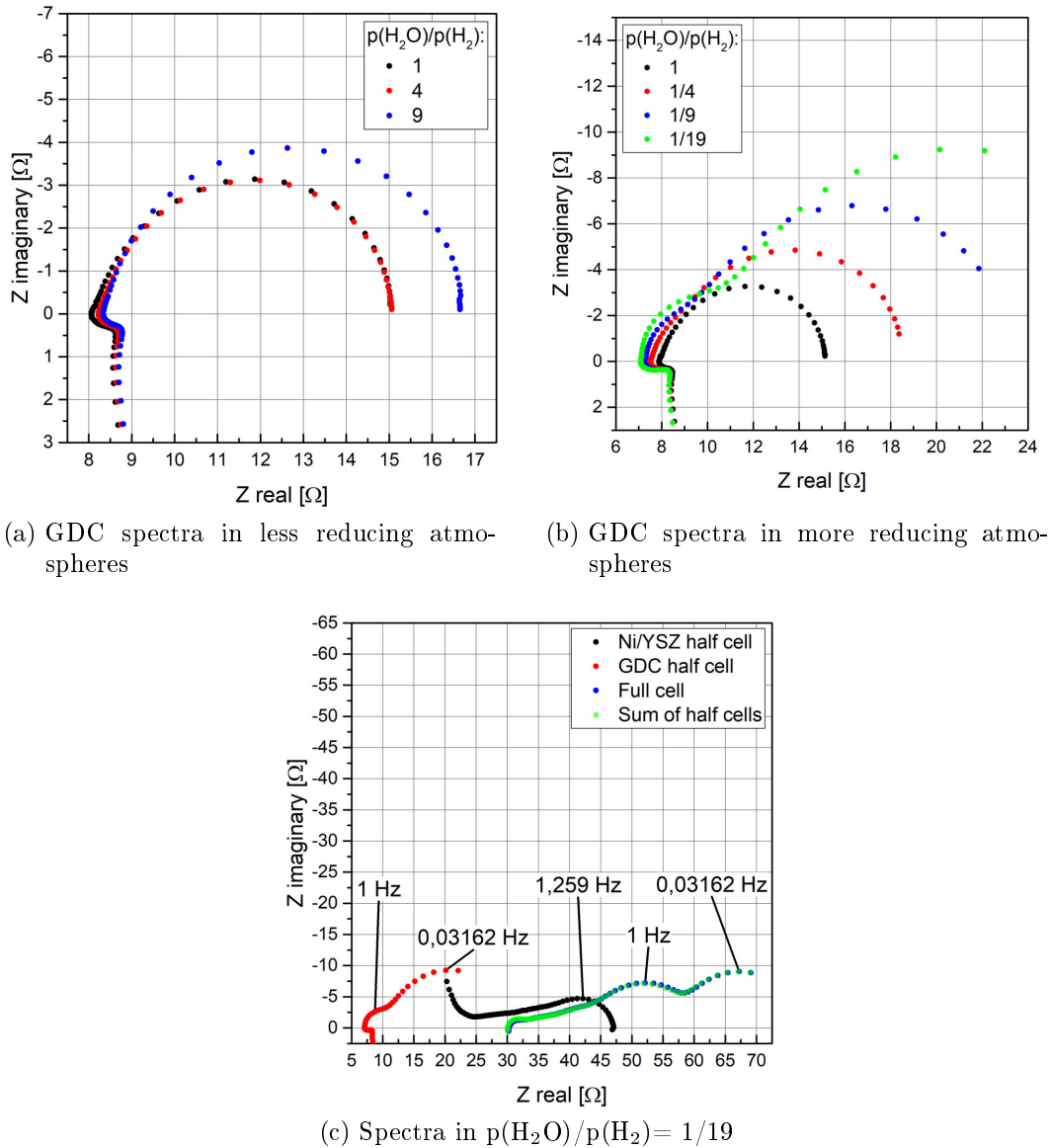

(c) Spectra in $p(H_2O)/p(H_2)= 1/19$

Figure 4.44: Impedance spectra of GDC three-electrode sample with Ni/YSZ counter electrode measured in different atmospheres at 750°C set temperature. Inset (c) shows the spectra of both the half cells, the full cell and the sum of the half cells in the most reducing measured atmosphere.

source of the artifact as changes with the electrode would also be visible in the full cell spectrum. The artifact was therefore attributed to changes with the reference electrode, resulting in a shift of the probed equipotential surface.

(a) GDC spectra, anodic bias

(b) GDC spectra, cathodic bias

(c) Spectra at +800 mV

(d) Spectra at -600 mV
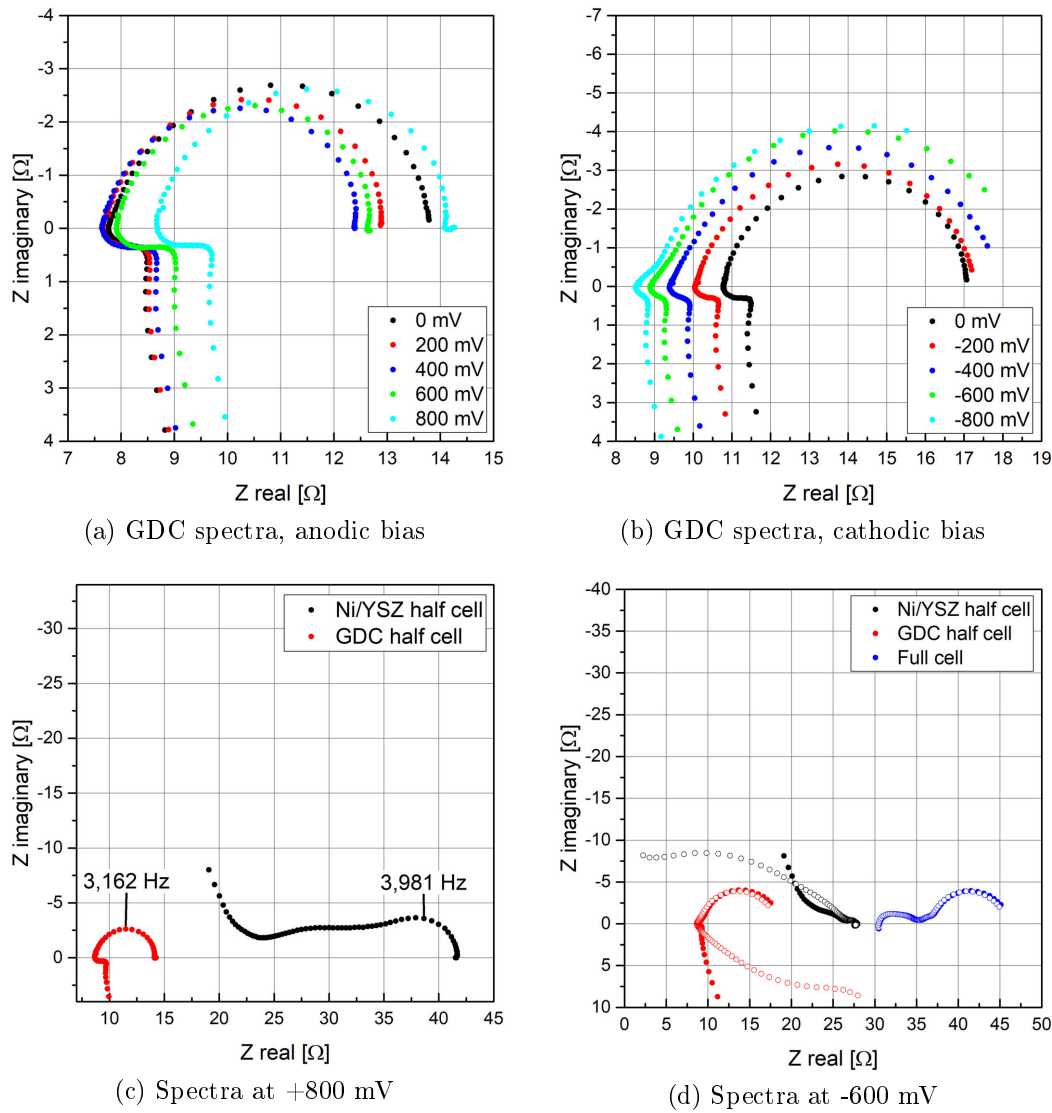
Figure 4.45: Impedance spectra of GDC three-electrode sample with Ni/YSZ counter electrode measured at 750°C set temperature in humidified hydrogen in argon under different bias voltages. Inset (c) shows the spectra of both half cells at the highest positive bias voltage of +800 mV. Inset (d) depicts a comparison of both the half cells spectra and the full cell spectra from before and after applying of the maximum negative bias voltage of -800 mV. Closed symbols represent the spectra before and open symbols after applying of the bias.

The GDC half cell spectra obtained at 750° set temperature were fitted with an offset resistance and a series connection of one or two R‖CPE elements. Again, spectra at strongly reducing atmospheres and with high cathodic bias were fitted with two R‖CPE elements. The extracted parameters are presented in Figure 4.46. The general trends were analogue to the measurements at 650° set temperature. The electrode resistance obtained from the $p(O_2)$ cycles showed a minimum around a one-to-one ratio of water and hydrogen. In more reducing conditions, the resistance showed a stronger increase than in less reducing atmospheres. With applied bias voltage, the resistance increased with cathodic bias and decreased with anodic bias until it reached a minimum around +70 mV effective overpotential. The chemical capacitance showed good accordance between the two different measurement cycles, with a strong increase at lower oxygen partial pressure that flattened out at higher pressures. The scaling of the chemical capacitance with the oxygen partial pressure was given by $C_{chem} \propto p(O_2)^{-0.36}$. The difference to the 650°C measurement is due to defect interactions when GDC becomes significantly sub-stoichiometric [50].

The current-voltage characteristic of the GDC half cell for both measuring temperatures is depicted in Figure 4.47. The curve obtained at 750°C set temperature was steeper than the curve obtained at 650°C. This was in accordance with the smaller resistances at higher temperatures. As the resistances with applied anodic bias were smaller than with cathodic bias, the slope of the curves was steeper with positive effective overpotential. Comparing this current-voltage characteristic to the characteristic of the GDC thin film sample (Figure 4.22), one finds good accordance. The linear regime of Figure 4.22 between -100 mV and +100 mV effective overpotential corresponds to the almost linear behavior of the three-electrode sample. Apart from that, the steeper course with applied anodic bias is present at both curves. Lastly, the current density at +75 mV effective overpotential was around 20 mA/cm^2 and 0.25 mA/cm^2 for three-electrode sample and thin film, respectively. A factor of 10^2 is a plausible difference between a porous sample and a thin film.

Summing up, the measurements of the GDC three-electrode sample with Ni/YSZ counter electrode delivered meaningful results that were in good agreement with the GDC thin film sample in subsection 4.1.4. The ASR (and the chemical capacitance) of the porous electrode were about 100 times smaller (10 times larger), due to the higher active surface and available GDC volume. Also the dependence of the ASR and C_{chem} on bias voltage or atmosphere was very similar between thin film and porous GDC. As the typical characteristic frequencies of the GDC electrode were in the low frequency range of the spectra, high frequency artifacts did not affect the electrode features. However, measurements with low H_2O partial pressure led to gas diffusion features in the counter electrode spectra that were in

(a) Electrode resistance, p(O₂) cycles

(b) Electrode resistance, bias cycles
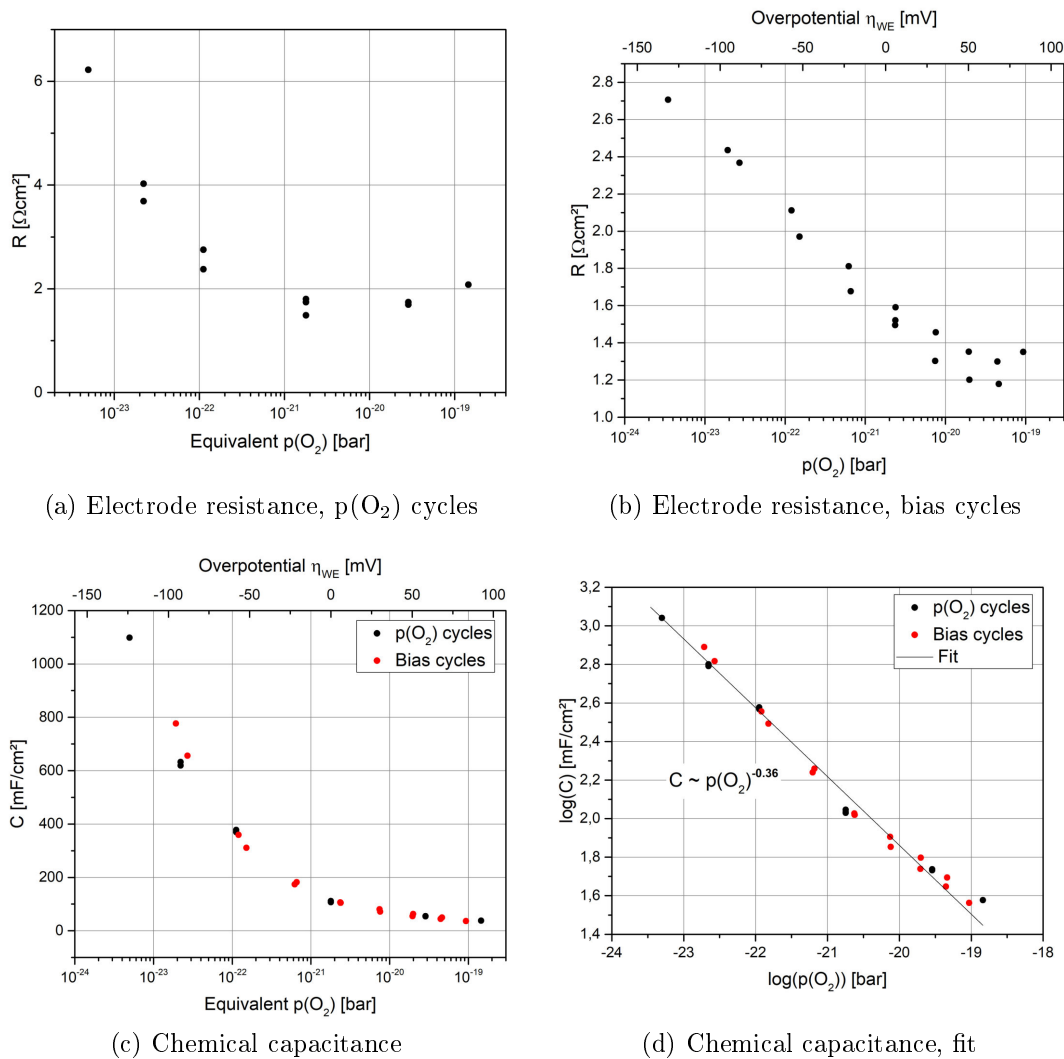

(c) Chemical capacitance

(d) Chemical capacitance, fit

Figure 4.46: Resistance and chemical capacitance of GDC half cell of the GDC three-electrode sample with Ni/YSZ counter electrode obtained with p(O₂) and bias cycles at a set temperature of 750°C. Inset (a) and inset (b) depict the resistance from the p(O₂) and bias cycles, respectively. Inset (c) shows a comparison of the chemical capacitance of the cycles. In inset (d) the logarithm of the chemical capacitance is fitted over the logarithm of the oxygen partial pressure. Oxygen partial pressures with applied bias voltage were calculated from the effective overpotential of the working electrode.
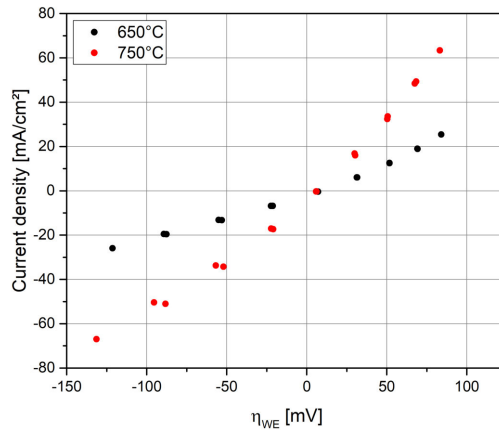
Figure 4.47: Current-voltage characteristic of GDC half cell of the GDC three-electrode sample with Ni/YSZ counter electrode measured in humidified hydrogen in argon

the same frequency range as the GDC electrode features. Hence, artifacts resulting from the Ni/YSZ electrode have not been clearly visible in the GDC spectra and could easily lead to false interpretations. Therefore, measurements should not be conducted in atmospheric conditions in which gas diffusion may be relevant.

4.2.4 GDC symmetric

Following the measurements on asymmetric three-electrode samples, symmetric samples were measured. Measurements on symmetric cells have the inherent problem that artifacts, originating from the counter electrode, are not visible in the spectra with OCV measurements, as the peak frequencies of both electrodes are identical. Applying bias, however, influences the electrodes in a different way as a constant DC current (equal to a net reaction in a certain direction) is associated with the bias voltage. Therefore, the spectra of identical half cells differ with applied bias voltage and artifacts are visible in the spectra.

The symmetric GDC sample was produced by screen printing GDC paste on the electrolyte and brushing the paste on the wing. After applying the Pt current collector, the sample was sintered at 1150°C for 3 hours. The measurements on the symmetric GDC sample were conducted in different reducing atmospheres at 650°C and 750°C set temperature and with applied bias voltage. The spectra were recorded between 10^6 and $2 * 10^{-2}$ Hz with an excitation voltage of 20 mV. As the spectra of the GDC three-electrode sample with Ni/YSZ counter electrode showed vast high frequency artifacts, active shielding of the reference electrode measuring line (see subsection 3.2.4) was implemented starting with the symmetric GDC

sample. A comparison between the spectra with and without active shielding is depicted in Figure 4.48. The spectra without active shielding both showed a vast high frequency artifact that drastically reduced in size once the shielding was activated. Unexpectedly, the nominally identical electrodes had rather different spectra. This finding was surprising, given that the electrodes were prepared at the same time. Apart from the high frequency artifact, the spectrum of half cell 1 showed a semicircle with a peak frequency of about 3 Hz, followed by an artifact semicircle with a peak frequency of 0.5 Hz. Notably, the size of the low frequency artifact was bigger than the size of the main feature. The spectrum of the second half cell only showed a dominant low frequency semicircle with a peak frequency of 0.5 Hz. Comparing the spectra to measurements on the asymmetric GDC three-electrode sample (Figure 4.34a) revealed accordance with the spectrum of half cell 2.
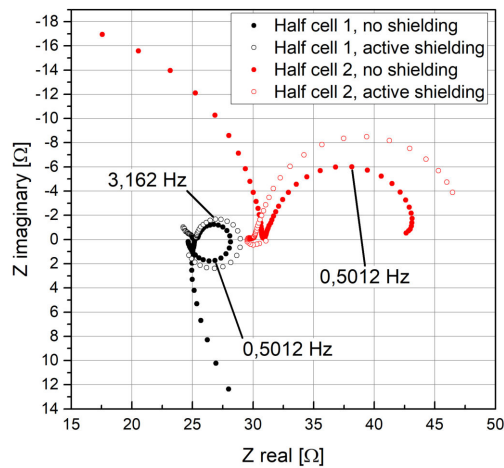
Figure 4.48: Impedance spectra of symmetric GDC three-electrode sample measured in humidified 2.5% hydrogen in argon around 620°C. The peak frequencies of the main features in the spectra are marked.

The spectra measured at 650°C set temperature in different reducing atmospheres are presented in Figure 4.49. The spectra of half cell 1 all showed a small high frequency artifact, followed by an intermediate frequency semicircle and a low frequency inductive artifact semicircle. Less reducing atmospheres led to a small increase of the size of the main electrode feature. The low frequency artifact remained uninfluenced with a size similar to the main feature. In more reducing atmospheres the electrode feature and the low frequency artifact both were more pronounced. However, the size of the artifact relative to the main feature decreased in more reducing conditions. The spectra of half cell 2 all showed a small high frequency artifact that was similar sized as the high frequency artifact from half

cell 1, followed by a dominant low frequency semicircle. Analogue to half cell 1, less reducing atmospheres had only little impact on the electrode feature, whereas more reducing atmospheres led to a distinct increase in size.
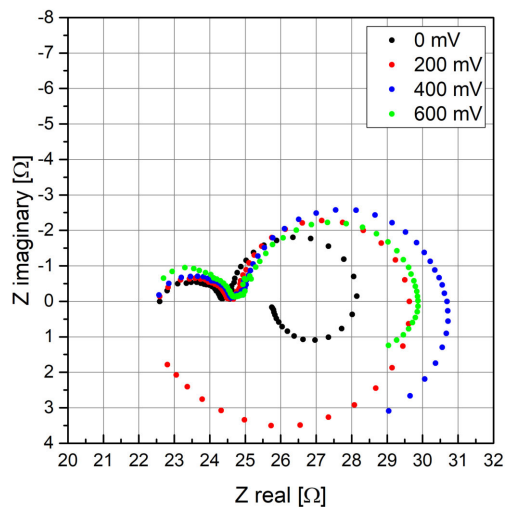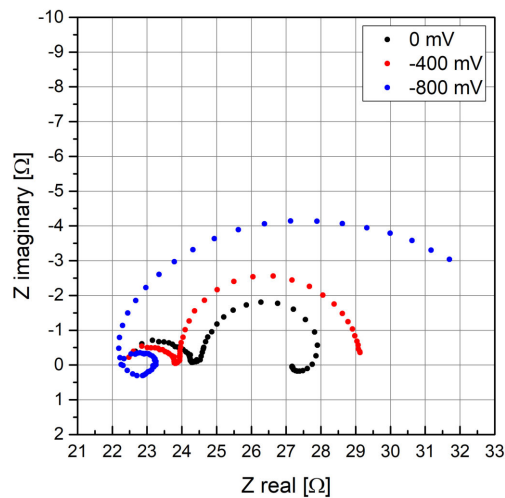

(a) Half cell 1

(b) Half cell 2
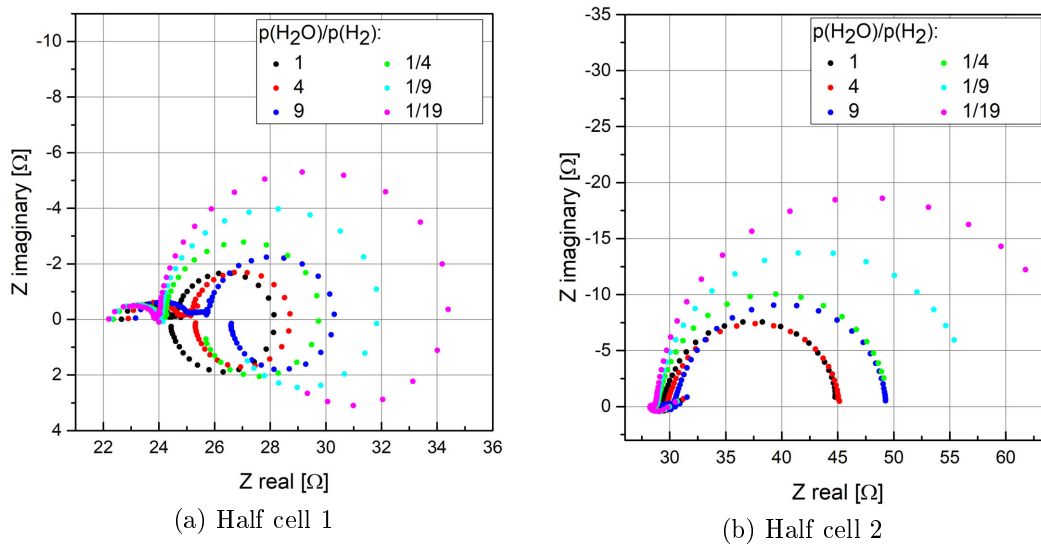
Figure 4.49: Impedance spectra of symmetric GDC three-electrode sample measured in different atmospheres at 650°C set temperature

The spectra with applied bias were all measured in a one-to-one ratio of hydrogen and water and are presented in Figure 4.50. The bias voltage is always applied to the working electrode (WE, half cell 1). However, positive bias on the WE corresponds to a negative potential of the counter electrode (CE, half cell 2) compared to the WE and vice versa. Therefore, the behavior of the WE under positive bias is analogue to the behavior of the CE under negative bias.

The spectra of half cell 1 with positive bias had the same shape as those obtained in different atmospheres. With increasing anodic bias, the size of the electrode feature increased until it reached a maximum at +400 mV. Also the size of the low frequency artifact was influenced by anodic bias. At +200 mV the artifact semicircle was larger than the electrode feature. Cathodic bias led to a depressed electrode feature with low peak frequency (0.1 Hz at -800 mV) and the disappearance of the low frequency artifact. However, the spectra obtained with high negative bias showed an inductive loop with a peak frequency of about 5 Hz. The spectra of half cell 2 showed similar behavior. With applied positive bias voltage, corresponding to a negative overpotential of the CE, the spectra showed an inductive loop and a depressed electrode feature with small peak frequency. Negative applied bias led to a higher peak frequency of the electrode feature and

(a) Half cell 1, anodic bias

(b) Half cell 1, cathodic bias
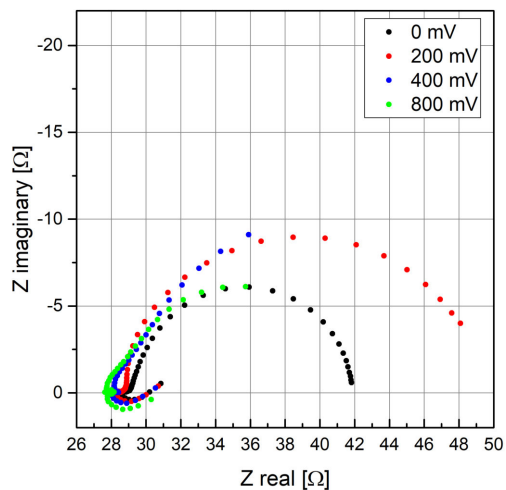
(c) Half cell 2, anodic bias
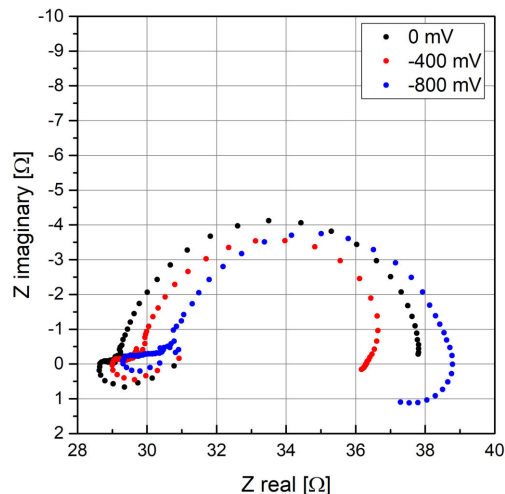
(d) Half cell 2, cathodic bias

Figure 4.50: Impedance spectra of symmetric GDC three-electrode sample measured at 650°C set temperature in humidified hydrogen in argon under different bias voltages. As the bias voltage is always applied to the WE (half cell 1), the effective overpotential of half cell 2 is positive for cathodic bias and vice versa.

the presence of a low frequency artifact feature. At -800 mV the peak frequency of the electrode feature was about 3 Hz and the peak frequency of the low frequency artifact was 0.5 Hz, corresponding to the features of half cell 1.

All obtained spectra at 650°C set temperature were fitted with an offset resis-

tance and a series connection of an R||CPE element. The extracted parameters are presented in Figure 4.51. Data of half cell 1 with applied anodic bias voltage was not included in the plots as the calculated effective overpotential did not yield meaningful results. Due to the vast artifact features in Figure 4.50a, the DC resistance is smaller than the high frequency electrolyte resistance. In such a case, negative overpotential is calculated for anodic bias. The electrode resistance in different atmospheres showed similar scaling for both half cells with a minimum at a one-to-one ratio of water and hydrogen. However, the ASR of half cell 1 was only about 25% of the ASR of half cell 2. Comparing the data with the asymmetric GDC three-electrode sample (Figure 4.43), revealed good agreement with half cell 2 regarding the ASR in different gas atmospheres. With applied bias voltage, the electrode resistance increased with negative overpotential at the electrodes. Again, the electrode resistance of half cell 1 was smaller but the difference was less distinct. The chemical capacitance showed only good accordance between the different measuring cycles with positive effective overpotential. At lower equivalent oxygen partial pressures, the chemical capacitance obtained with the bias cycles varied stronger than for gas partial pressure dependent measurements. When artifacts are present in the spectra, calculation of the overpotential is prone to errors because the high frequency offset does not necessarily reflect the electrolyte resistance in DC conditions. Fitting of the chemical capacitance obtained with the $p(O_2)$ cycles revealed a scaling with the oxygen partial pressure given by $C_{chem} \propto p(O_2)^{-0.19}$ which was a little lower than the ideal scaling given by Equation 4.8.

The spectra measured at 750°C set temperature in different atmospheres are presented in Figure 4.52. The spectra of half cell 1 showed a small high frequency artifact, followed by a dominant low frequency semicircle. Contrary to the measurements at 650°C set temperature, no low frequency artifact was visible in the spectra. Again, less reducing atmospheres had only little influence on the electrode feature, whereas more reducing atmospheres led to a strong increase in size. The spectra of half cell 2 showed a high frequency inductive artifact, followed by an intermediate frequency shoulder and a dominant low frequency semicircle. The influence of changing atmospheres on the main feature was analogue to half cell 1. Notably, the peak frequencies of the main features of both half cells were comparable in every atmosphere. Therefore, artifacts originating from the respective counter electrode, if present, do not produce additional features.

The spectra with applied bias voltage are presented in Figure 4.53. As the bias voltage causes different peak frequencies for half cell 1 and 2, artifacts become visible. The spectra of half cell 1 showed a small high frequency artifact, followed by a dominant semicircle. With increasing anodic bias voltage, a low frequency inductive artifact semicircle became visible that changed into a loop at +800 mV. Under cathodic bias the dominant feature increased in size and got more
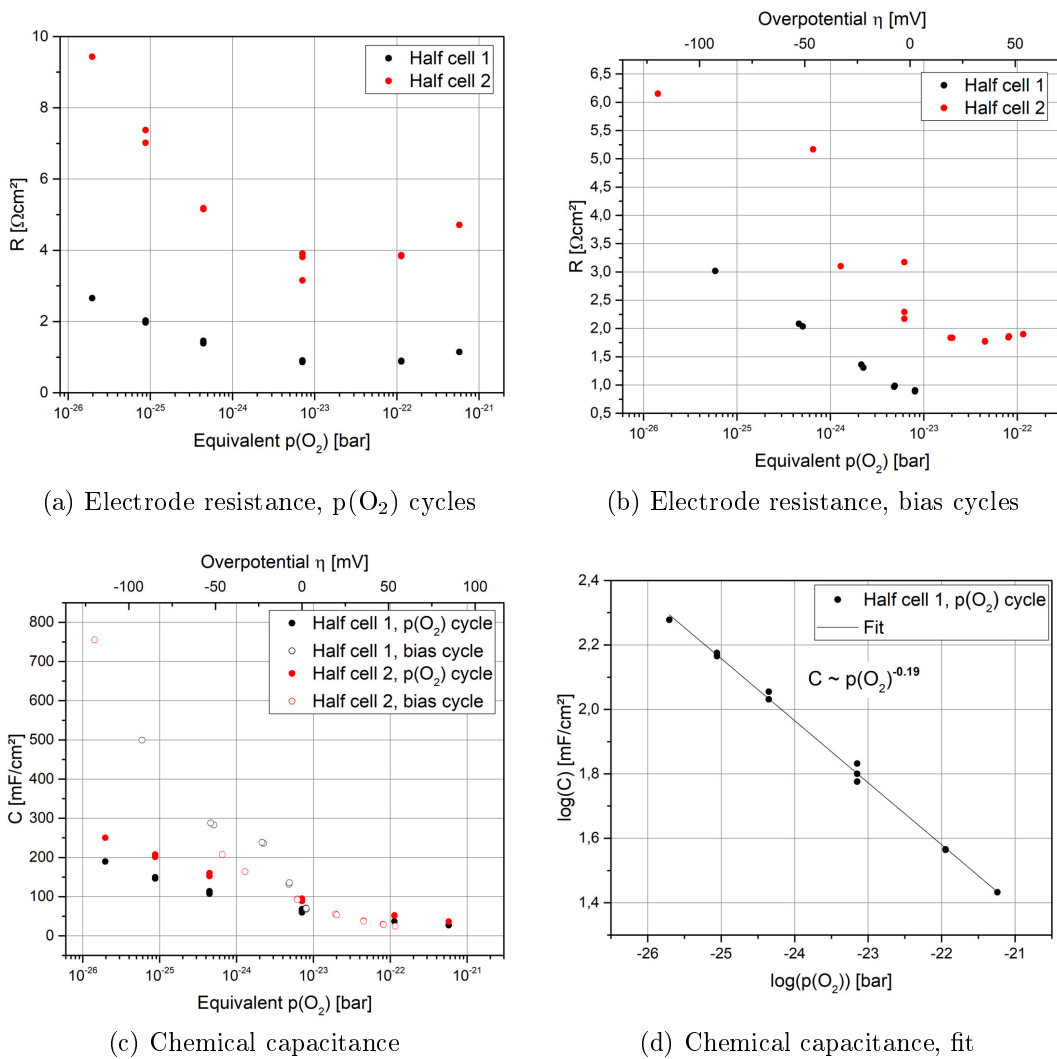
(a) Electrode resistance, p(O₂) cycles

(b) Electrode resistance, bias cycles

(c) Chemical capacitance

(d) Chemical capacitance, fit

Figure 4.51: Resistance and chemical capacitance of symmetric GDC three-electrode sample obtained with p(O$_2$) and bias cycles at a set temperature of 650℃. Inset (a) and inset (b) depict the resistance from the p(O$_2$) and bias cycles, respectively. Inset (c) shows a comparison of the chemical capacitance of the cycles. In inset (d) the logarithm of the chemical capacitance is fitted over the logarithm of the oxygen partial pressure. Oxygen partial pressures with applied bias voltage were calculated from the effective overpotential of the respective electrode.

(a) Half cell 1   (b) Half cell 2
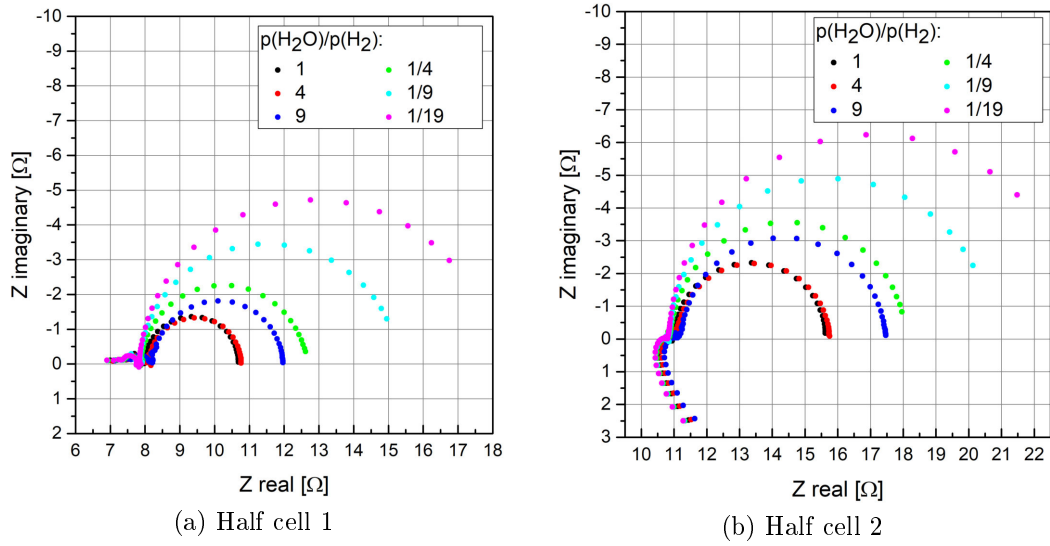
Figure 4.52: Impedance spectra of symmetric GDC three-electrode sample measured in different atmospheres at 750°C set temperature

depressed. Starting with -600 mV, the spectra included an intermediate frequency loop feature and a non-closing low frequency feature. The spectra of half cell 2 showed analogue behavior with low frequency loops at positive effective overpotential (corresponding to negative applied bias voltage) and intermediate frequency loops at negative effective overpotential. Again, also the peak frequencies of the electrode and artifact features were comparable between the two electrodes, considering comparable bias voltages. At +800 mV, the electrode feature of half cell 1 had a peak frequency of about 3 Hz which was also found at -800 mV with half cell 2.

All measured spectra at 750°C set temperature were fitted with an offset resistance and a series connection of an R||CPE element. The extracted parameters are presented in Figure 4.54. Data from the spectra with a non-closing low frequency was not included in the plots as the equivalent circuit fit did not yield meaningful results. The electrode resistance in different atmospheres showed the expected scaling with the oxygen partial pressure and a minimum at a one-to-one ratio of water and hydrogen. The difference between the half cells was about 0.5 Ωcm^2 for all atmospheres. With applied bias voltage the electrode resistance increased with negative effective overpotential and was rather constant with positive effective overpotential. Notably, the chemical capacitance showed good accordance between both half cells p(O_2) cycles and the bias cycle of half cell 2. Fitting of the chemical capacitance revealed a scaling of $C_{chem} \propto p(O_2)^{-0.45}$ for the bias cycle of half cell 1 and an ideal scaling of $C_{chem} \propto p(O_2)^{-0.25}$ for all other cycles. Again,
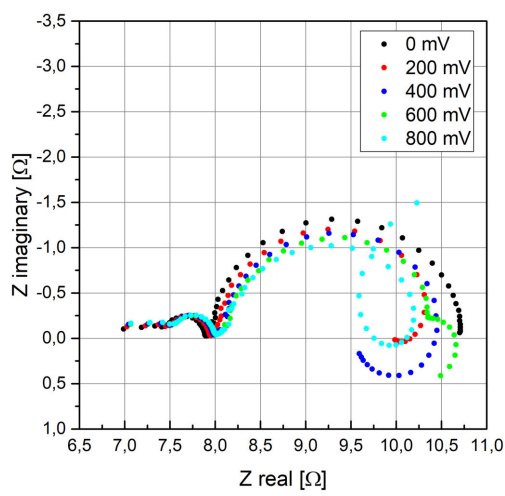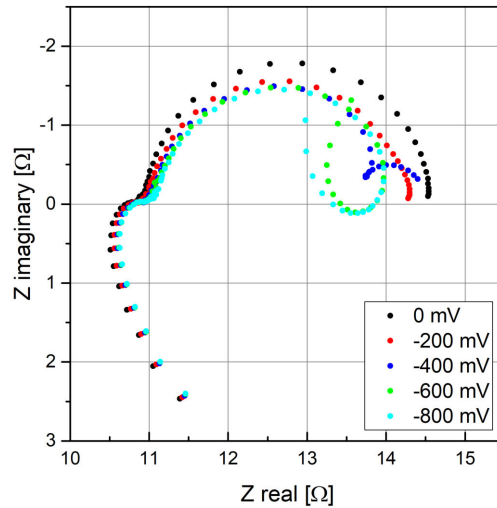
(a) Half cell 1, anodic bias
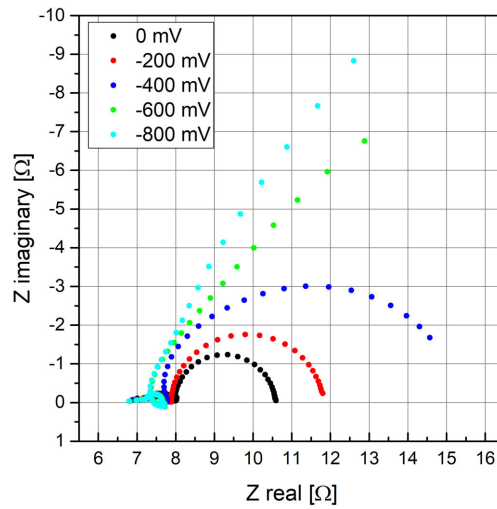
(b) Half cell 1, cathodic bias
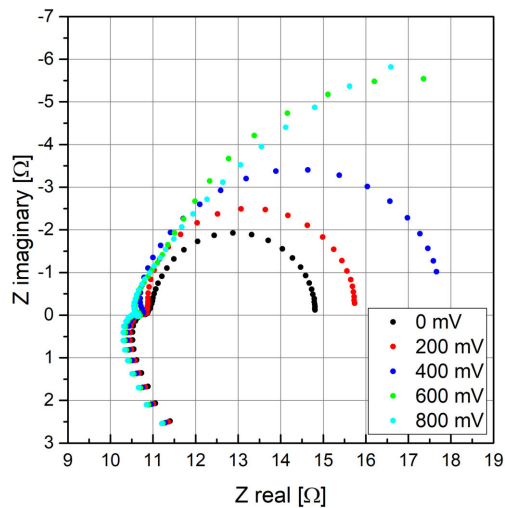
(c) Half cell 2, anodic bias

(d) Half cell 2, cathodic bias

Figure 4.53: Impedance spectra of symmetric GDC three-electrode sample measured at 750°C set temperature in humidified hydrogen in argon under different bias voltages. As the bias voltage is always applied to the WE (half cell 1), the effective overpotential of half cell 2 is positive for cathodic bias and vice versa.

this discrepancy of the exponents shows that calculation of an exact overpotential is difficult for EIS spectra containing artifacts.

The current-voltage characteristics of both half cells are depicted in Figure 4.55. Generally, the curves had a steeper course with positive overpotential that was also

present in the previously recorded current-voltage characteristics of GDC samples. However, the linear course of the asymmetric GDC three-electrode sample was not found. At 650°C set temperature the curves of both half cells differ clearly. The curve of half cell 1 was disrupted with an offset of about 25 mV under anodic bias. This was presumably caused by a shift of the equipotential surface of the reference electrode with the frequency, causing a difference between the AC and the DC electrolyte offset. To accurately calculate the effective overpotential of the electrode, the DC electrolyte offset resistance is needed. However, only the AC value is accessible through the impedance spectra. As the artifacts in the spectra of half cell 1 under anodic bias at 650°C were particularly distinct, the difference between the AC and DC electrolyte offset was significant. Considering the cathodic regime, half cell 2 covers a larger overpotential range than half cell 1 which was expected due to the larger ASR. Apart from that, the curve of half cell 1 flattened with increasing cathodic bias, whereas the curve of half cell 2 showed a plateau. At 750°C the curves of both half cells had a similar flattening course in the cathodic regime that indicated the relevance of gas diffusion limitation. With positive overpotential, the curve of half cell 1 was steeper than the curve of half cell 2 which started flattening at higher overpotentials.

Summing up, it was possible to extract meaningful results from the measured spectra even though artifacts were present. The active shielding significantly reduced the high frequency artifacts originating form a voltage divider effect on the measuring line of the reference electrode. Differences in the ASR and the peak frequencies of the nominally identical half cells were rather large at 650°C set temperature, leading to the presence of significant low frequency artifacts in the spectra of half cell 1. At 750°C set temperature, the differences between the half cells were considerably smaller and the extracted properties showed good agreement with the previous measurements on other samples. However, due to the more distinct separation of electrode and artifact features when using appropriate counter electrode materials (peak frequencies at least two orders of magnitude apart), measurements on asymmetric three-electrode samples provide better results.
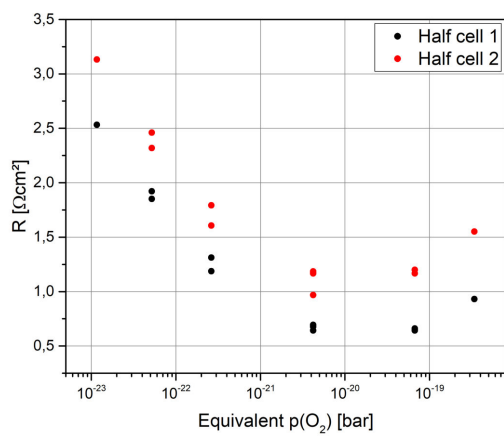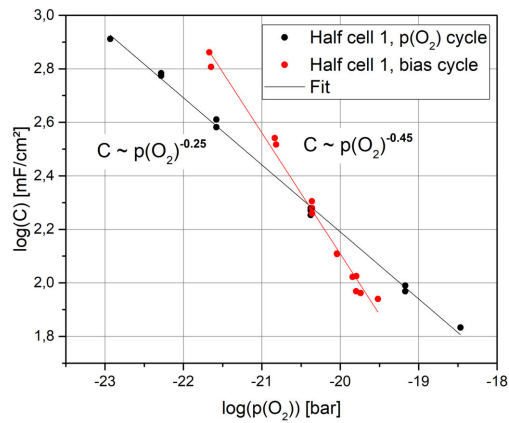
(a) Electrode resistance, p(O$_2$) cycles
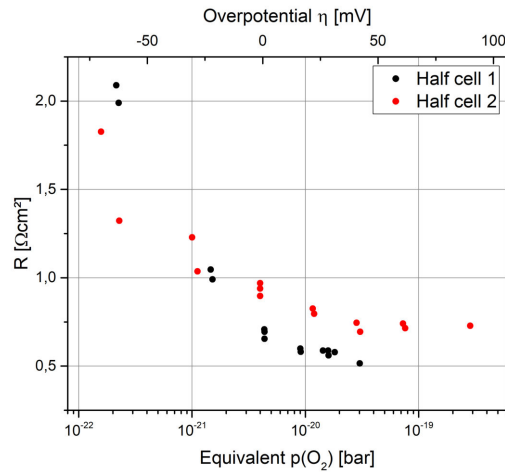
(b) Electrode resistance, bias cycles
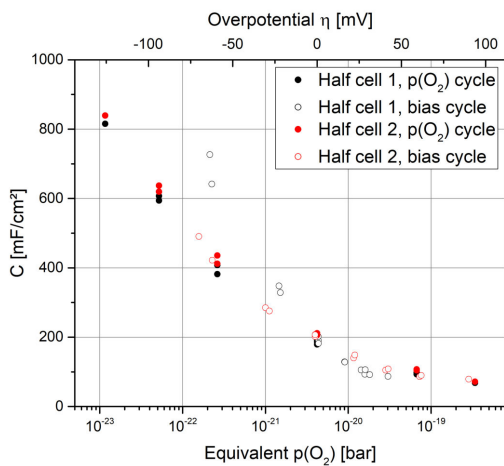
(c) Chemical capacitance

(d) Chemical capacitance, fit

Figure 4.54: Resistance and chemical capacitance of symmetric GDC three-electrode sample obtained with p(O$_2$) and bias cycles at a set temperature of 750℃. Inset (a) and inset (b) depict the resistance from the p(O$_2$) and bias cycles, respectively. Inset (c) shows a comparison of the chemical capacitance of the cycles. In inset (d) the logarithm of the chemical capacitance is fitted over the logarithm of the oxygen partial pressure. Oxygen partial pressures with applied bias voltage were calculated from the effective overpotential of the respective electrode.
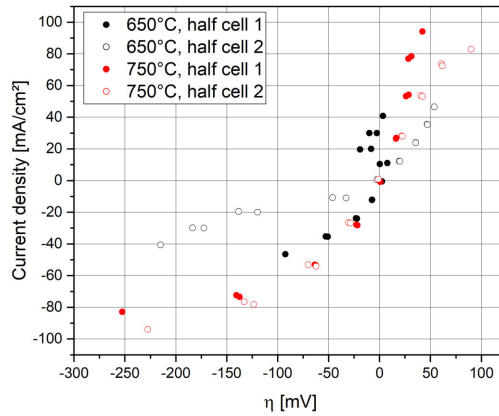
Figure 4.55: Current-voltage characteristic of the symmetric GDC three-electrode sample measured in humidified hydrogen in argon

4.2.5 LSF symmetric

The symmetric LSF three-electrode sample was prepared by depositing GDC thin films on both sides of the electrolyte as a diffusion barrier and subsequently screen printing of the LSF electrodes on the substrate. Sintering was done at 1050°C, as elaborated in the experimental section. The reference electrode was porous GDC with a Pt current collector. Measurements were conducted in different oxidizing and reducing atmospheres and with applied bias voltage. To minimize the influence of gas diffusion, the measurements in reducing conditions were performed in a low pressure measuring setup (see subsection 3.2.5). Again, active shielding was used to minimize the coupling capacitance of the reference electrode measuring line to its shield and therefore to decrease the high frequency artifacts. However, the shielding did not yield the expected results: Without shielding, the high frequency artifact was an inductive line for one electrode and a capacitive line for the other. Improving the setup in a way that the complex part of the impedance was approaching zero at 10^6 Hz resulted in a high frequency semicircle as artifact, see Figure 4.56. As the shielding setup consisted only of two potentiometers, the amplitude and phase of the RE shielding was adjusted to a fixed value and it was not possible to fully compensate the capacitive currents at every frequency.

The spectra in different oxidizing atmospheres at 650°C set temperature are presented in Figure 4.57. The spectra of both half cells showed a high frequency artifact followed by a 45° slope and a dominant low frequency feature. Lowering the oxygen partial pressure led to a shorter slope and a more pronounced low frequency semicircle. As the dominant feature of half cell 1 had a larger ASR and lower peak frequency than the corresponding feature of half cell 2, it was not fully contained in the measured spectra at low oxygen partial pressures. However, the
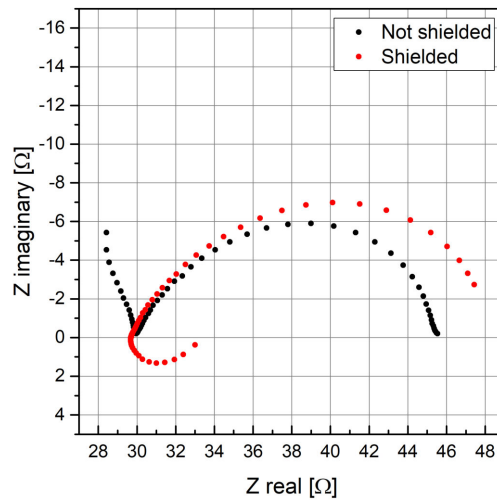
Figure 4.56: Impedance spectra of half cell 2 of the symmetric LSF three-electrode sample measured in pure oxygen around 620°C
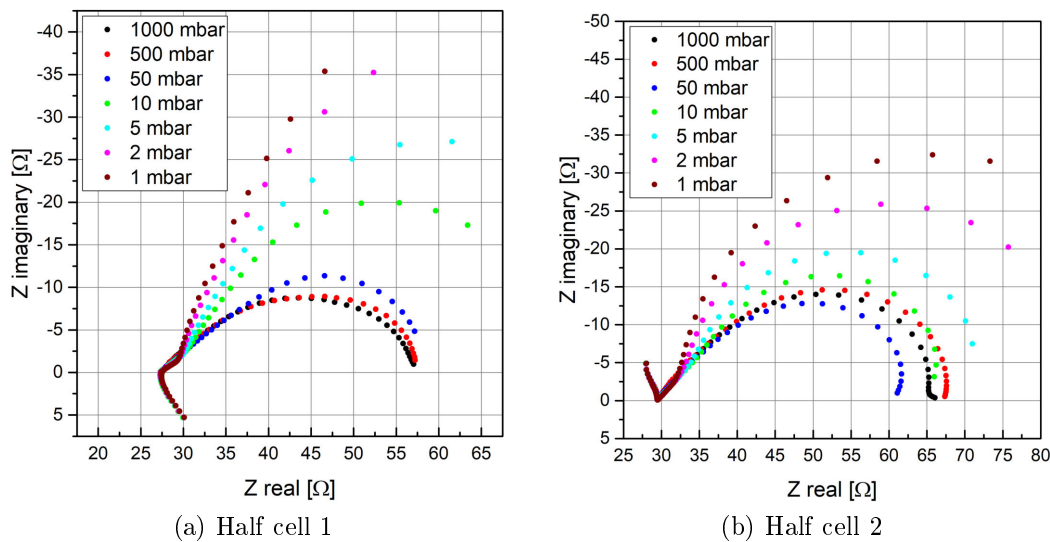

(a) Half cell 1

(b) Half cell 2

Figure 4.57: Impedance spectra of symmetric LSF three-electrode sample measured at 650°C set temperature and different oxygen partial pressures

spectra of both cells showed good accordance with the spectra of the asymmetric LSF sample, see Figure 4.23b).

The spectra with applied bias were measured in the range of ± 1000 mV and are presented in Figure 4.58. Both half cells showed consistent behavior, yet applying bias had a strong influence on the spectra. Positive effective overpotential on the electrode resulted in a higher peak frequency of the dominant feature (0.25 - 5

Hz), whereas negative effective overpotential resulted in a lower peak frequency (0.05 - 0.2 Hz). Therefore, the spectra of the half cell with positive overpotential showed a low frequency inductive artifact, originating from the other half cell, that was well separated from the electrode feature. Considering the half cell with negative overpotential however, the peak frequency of its electrode feature was lower than the peak frequency of the respective counter electrode. Contrary to the measurements with the Pt/YSZ counter electrode, where the peak frequencies were sufficiently separated even with applied bias voltage, this led to artifacts in the intermediate frequency range which interfered with the electrode feature. As a result, the spectra with negative overpotential often contained inductive loops that did not allow a meaningful fit with an equivalent circuit.

Positive effective overpotential generally led to a more depressed dominant feature that increased in size until ± 400 mV, depending on the half cell. Above that, the size decreased abruptly and the feature separated into two distinct features with peak frequencies of about 300 Hz and 3 Hz, respectively. This behavior was not observed with the asymmetric LSF sample, where the electrode feature decreased in size with increasing positive effective overpotential and did not separate into two distinctive features.

The spectra in different oxidizing atmospheres were fitted with the transmission line equivalent circuit as described in subsection 4.2.1. For the spectra with applied bias voltage, no consistent fit was possible. Therefore, the ASR was directly extracted from the spectra by subtracting the low frequency real axis intercept from the high frequency one. However, this was only possible for the half cell spectra with positive effective overpotential. The extracted parameters are depicted in Figure 4.59. The electrode resistance in different atmospheres was rather constant at higher oxygen partial pressures and increased towards lower pressures. This coincided with the data from the asymmetrical LSF sample. With applied bias voltage, the electrode resistance had a maximum at around 125 mV effective overpotential. In both measuring cycles, the electrode resistance of half cell 1 was larger than the resistance of half cell 2. As expected, the chemical capacitance increased with decreasing oxygen partial pressure, since the minority charge carriers were oxygen vacancies in this partial pressure range. Also the effective ionic conductivity increased with decreasing oxygen partial pressure, corresponding to an increased concentration of oxygen vacancies. Both the chemical capacitance and ionic conductivity showed good agreement with the asymmetrical sample considering scaling and magnitude.
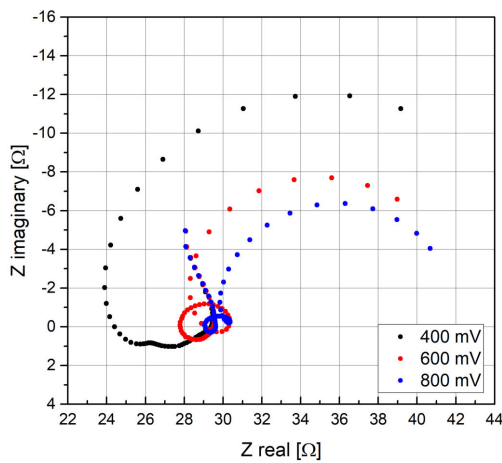
The spectra measured at 750°C set temperature showed similar behavior as the spectra at 650°C set temperature. Spectra measured in different atmospheres are presented in Figure 4.60, those measured with applied bias in Figure 4.61. Negative effective overpotential on the measured electrode again resulted in distorted spectra
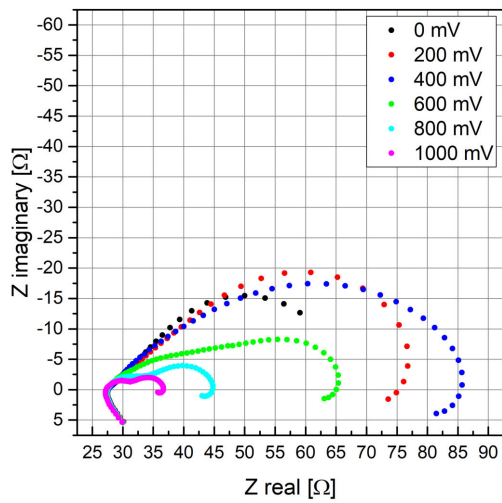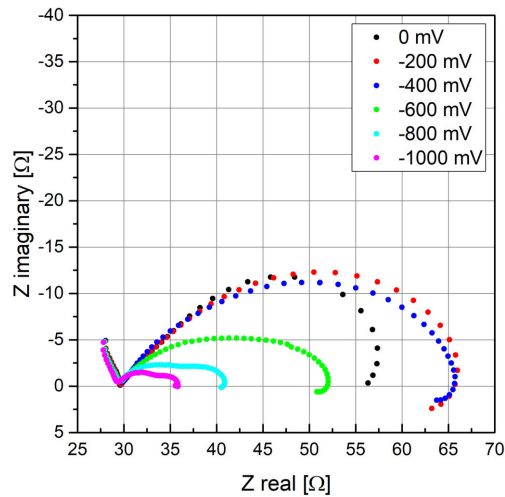
92

(a) Half cell 1, anodic bias
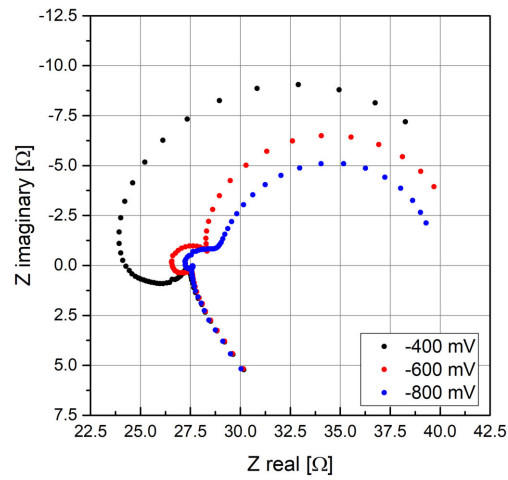
(b) Half cell 1, cathodic bias

(c) Half cell 2, anodic bias

(d) Half cell 2, cathodic bias

Figure 4.58: Impedance spectra of symmetric LSF three-electrode sample measured at 650°C set temperature in 1% O_2 under different bias voltages. As the bias voltage is always applied to the WE (half cell 1), the effective overpotential of half cell 2 is positive for cathodic bias and vice versa.

as the peak frequencies of the half cells were not compatible. Notably, also the spectra with positive effective overpotential were distorted at high applied bias voltages, as the low frequency inductive artifact changed into a loop followed by another capacitive semicircle.
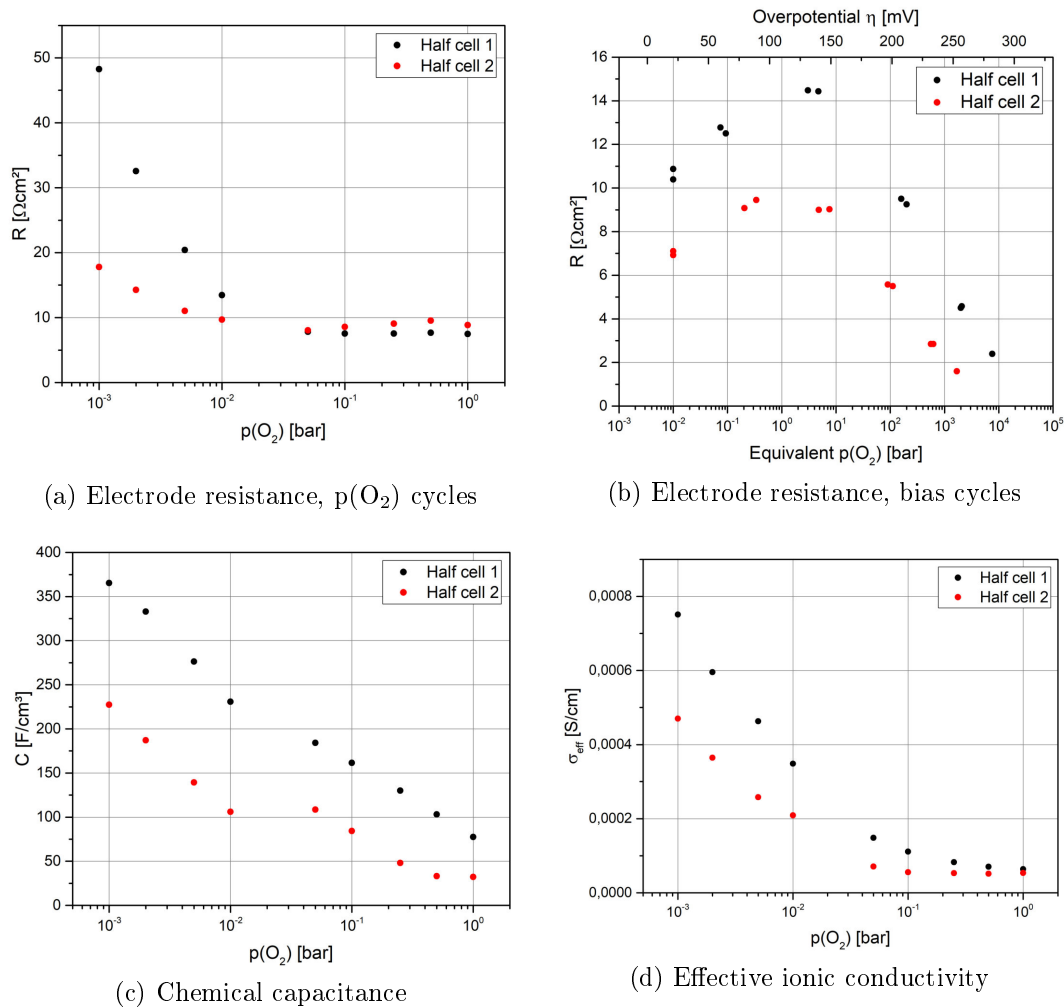
(a) Electrode resistance, p(O$_2$) cycles

(b) Electrode resistance, bias cycles

(c) Chemical capacitance

(d) Effective ionic conductivity

Figure 4.59: Resistance, chemical capacitance and effective ionic conductivity of symmetric LSF three-electrode sample obtained with p(O$_2$) and bias cycles at a set temperature of 650°C. Inset (a) and inset (b) depict the resistance from the p(O$_2$) and bias cycles, respectively. Inset (c) shows the chemical capacitance of the p(O$_2$) cycle, in inset (d) the effective ionic conductivity is shown. Oxygen partial pressures with applied bias voltage were calculated from the effective overpotential of the respective electrode.

All the measured spectra were fitted with the transmission line equivalent circuit used at 650°C. However, fitting was not possible for the spectra with negative effective overpotential and the spectra with the highest positive effective overpotential as these spectra were too heavily distorted. The extracted parameters are
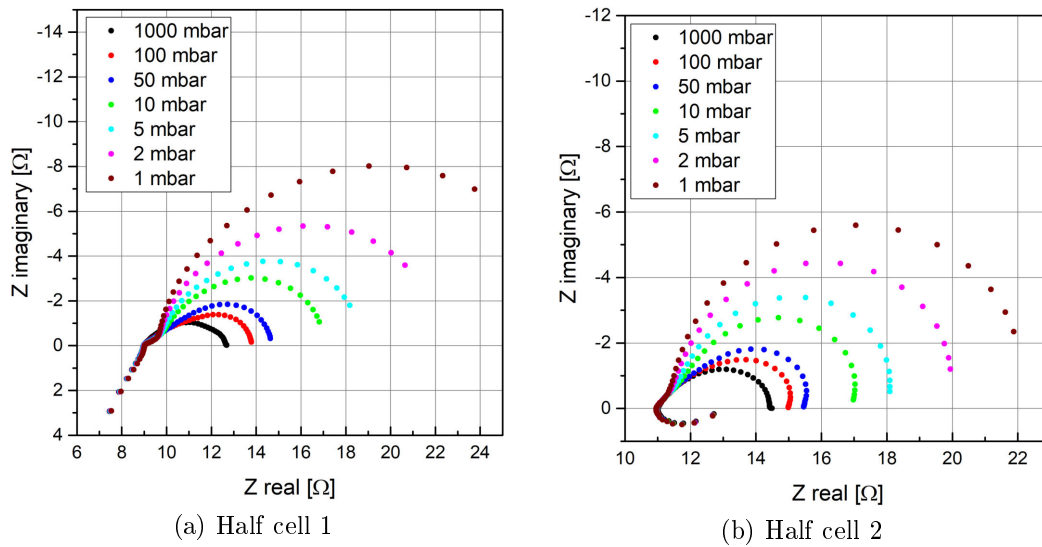
(a) Half cell 1

(b) Half cell 2

Figure 4.60: Impedance spectra of symmetric LSF three-electrode sample measured at 750°C set temperature and different oxygen partial pressures

depicted in Figure 4.62. The electrode resistance obtained in different atmospheres showed the expected increase with falling oxygen partial pressure. With applied bias voltage, the electrode resistance had a maximum around +50 mV effective overpotential. The chemical capacitance coincided between both bias cycles and the $p(O_2)$ cycle of half cell 2 and was also in accordance to the results from the asymmetrical LSF sample. Considering the effective ionic conductivity, all measurement cycles yielded similar results with a constant course at higher oxygen partial pressures and an increase with lower partial pressures.

The current-voltage characteristics of the sample for both measuring temperatures are depicted in Figure 4.63. As expected, the curves of half cell 2 had steeper courses over the whole overpotential range, corresponding to smaller ASRs. Apart from that, the curves were similar and showed agreement with the measurements from the asymmetric sample.

The low pressure measurements in reducing atmospheres were conducted at 625°C and 725°C set temperature in the low pressure measurement setup in pure H_2 + H_2O without Ar balance. Again, spectra were recorded in different atmospheric conditions and with applied bias voltage. The atmospheres were defined by the partial pressure of H_2 that ranged from 6 mbar to 65.5 mbar and the constant partial pressure of H_2O (approx. 25 mbar). The recorded spectra at 625°C set temperature in different atmospheres are presented in Figure 4.64. As the shielding of the reference electrode measuring line was not active during the measurement, the spectra showed vast high frequency artifacts. For half cell 1, the artifact was
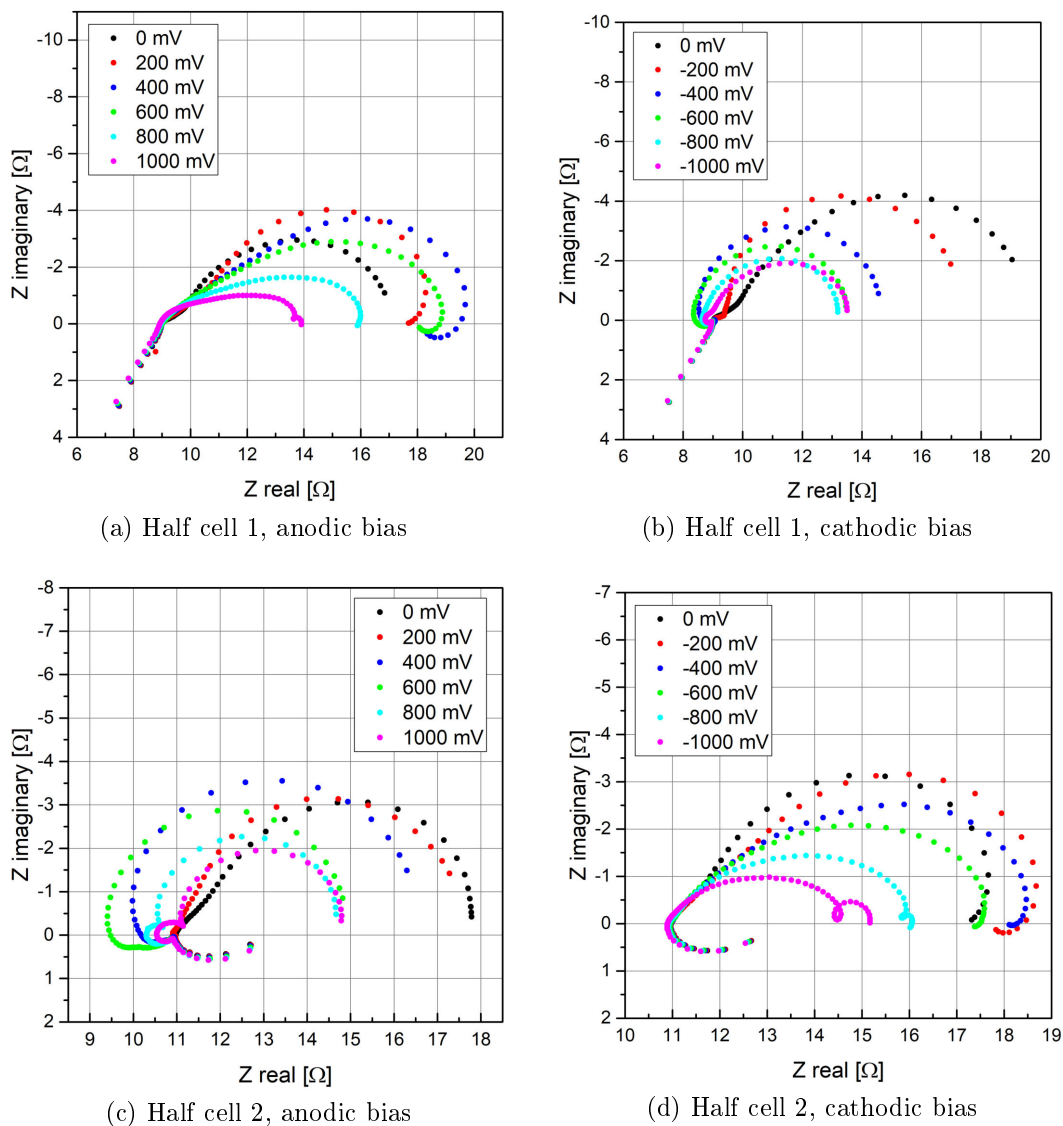
(a) Half cell 1, anodic bias

(b) Half cell 1, cathodic bias

(c) Half cell 2, anodic bias

(d) Half cell 2, cathodic bias

Figure 4.61: Impedance spectra of symmetric LSF three-electrode sample measured at 750°C set temperature in 1% O_2 under different bias voltages. As the bias voltage is always applied to the WE (half cell 1), the effective overpotential of half cell 2 is positive for cathodic bias and vice versa.

followed by an intermediate frequency shoulder and a depressed low frequency semicircle. The spectra of half cell 2 did not contain the shoulder, but also showed a dominant low frequency feature. Increasing the hydrogen partial pressure did not influence the shape of the spectra but resulted in a decreased ASR. The peak
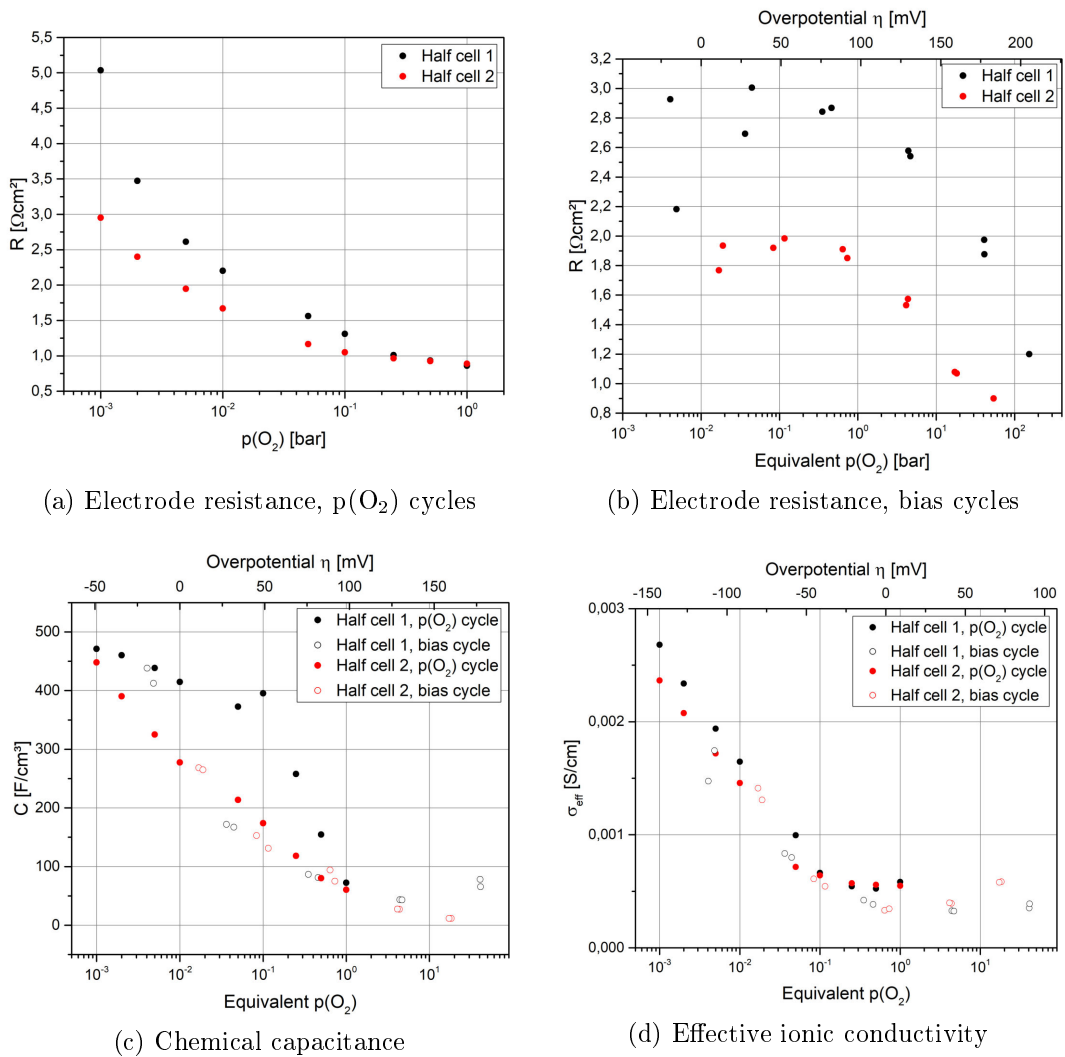
(a) Electrode resistance, p(O$_2$) cycles

(b) Electrode resistance, bias cycles

(c) Chemical capacitance

(d) Effective ionic conductivity

Figure 4.62: Resistance, chemical capacitance and effective ionic conductivity of symmetric LSF three-electrode sample obtained with p(O$_2$) and bias cycles at a set temperature of 750°C. Inset (a) and inset (b) depict the resistance from the p(O$_2$) and bias cycles, respectively. Inset (c) shows a comparison of the chemical capacitance obtained with the different cycles, inset (d) of the ionic conductivity. Oxygen partial pressures with applied bias voltage were calculated from the effective overpotential of the respective electrode.
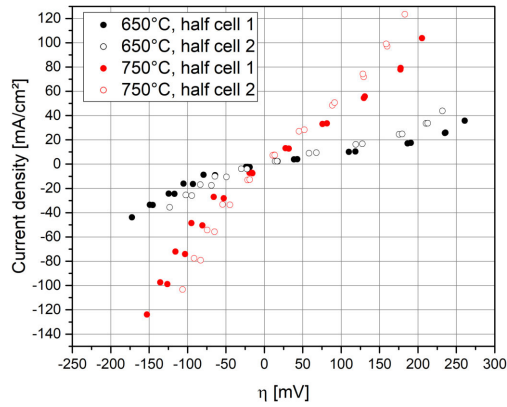
Figure 4.63: Current-voltage characteristic of the symmetric LSF three-electrode sample measured in 1% O_2
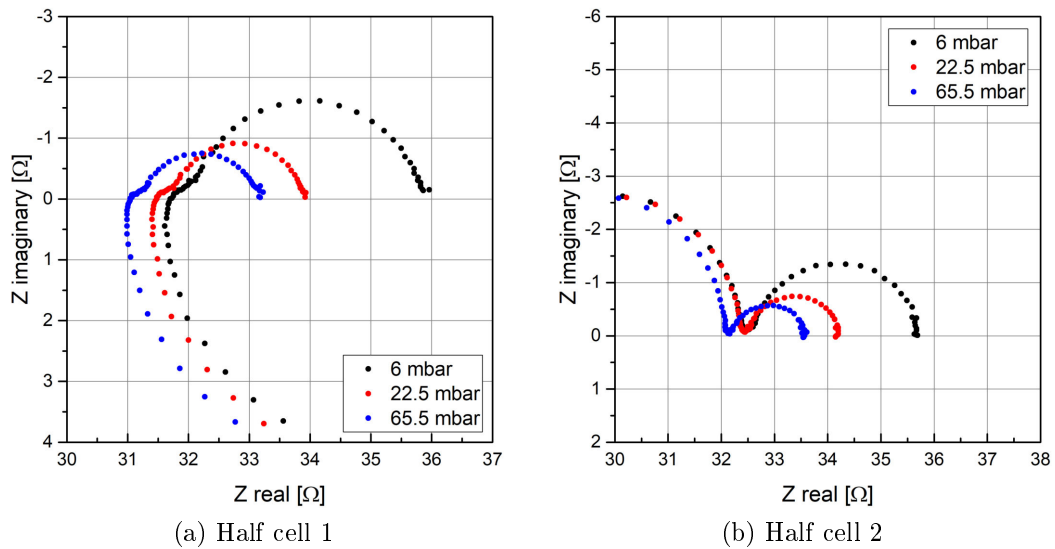

(a) Half cell 1

(b) Half cell 2

Figure 4.64: Impedance spectra of symmetric LSF three-electrode sample measured at 625°C set temperature with different hydrogen partial pressures

frequency of the main feature was rather constant around 10 Hz.

The bias measurements were conducted in range of ± 2000 mV and in an atmosphere with 22.5 mbar hydrogen partial pressure. The measured spectra are presented in Figure 4.65. With positive effective overpotential on the measured electrode, the spectra had a similar shape as those measured in different atmospheres and a peak frequency of about 3 Hz. The main electrode feature of half cell 1 increased with increasing bias, whereas the corresponding feature of half cell

2 was rather constant. Both half cells showed the beginning of a low frequency inductive artifact at higher bias voltages. The spectra with negative effective overpotential were heavily distorted with intermediate frequency artifacts that were considerably larger than the electrode features. As those artifacts split the electrode features, meaningful equivalent circuit fits were not possible.

The spectra were fitted with a series connection of an offset resistance and one or two R∥CPE elements, where one element was used for the spectra of half cell 2 and two elements for the spectra of half cell 1. The extracted parameters are depicted in Figure 4.66. The electrode resistance obtained in different atmospheres increased with increasing oxygen partial pressure which was already clearly visible in the recorded spectra. Comparing the results with the asymmetric LSF sample (Figure 4.37) revealed an about 1 Ωcm^2 lower ASR for the symmetric sample. The reason for this was the low pressure setup, in which the symmetric sample was measured, that reduced the influence of gas diffusion. With applied bias voltage, the electrode resistance increased with increasing bias. However, the ASR of half cell 2 reached a plateau at higher bias voltages which was not the case for half cell 1. Considering the chemical capacitance, the values obtained with the different measuring cycles coincided. An increasing chemical capacitance with decreasing oxygen partial pressure was expected (minority charge carrier are electrons) and was also found with the asymmetric sample. Fitting of the chemical capacitance in the low pressure range revealed a scaling of $C_{chem} \propto p(O_2)^{-0.16}$.

The spectra measured at 725°C in different atmospheres are presented in Figure 4.67. Generally, the spectra of both half cells showed similar behavior as those recorded at 625°C. However, the intermediate frequency shoulder was now also visible in the spectra of half cell 2. The peak frequency of the dominant feature was in the range of 4 Hz to 13 Hz.

The spectra with applied bias voltage are presented in Figure 4.68. Positive effective overpotential did not influence the shape of the spectra but led to an increased ASR and the beginning of a low frequency artifact. Negative effective overpotential, however, resulted in massive artifacts that were several times the size of the electrode feature. As again the frequency ranges were not compatible, those artifacts heavily distorted the spectra and prohibited meaningful equivalent circuit fits.

Fitting of the spectra was done with a series connection of an offset resistance and two R∥CPE elements. The extracted parameters are depicted in Figure 4.69. The electrode resistance of both half cells increased with increasing oxygen partial pressure. Contrary to the measurements at 625°C, the electrode resistance of half cell 1 was lower than the resistance of half cell 2 in changing atmospheres. With the bias cycles, a maximum of the electrode resistance was observable around 125 mV. The chemical capacitance showed good accordance between the different measuring
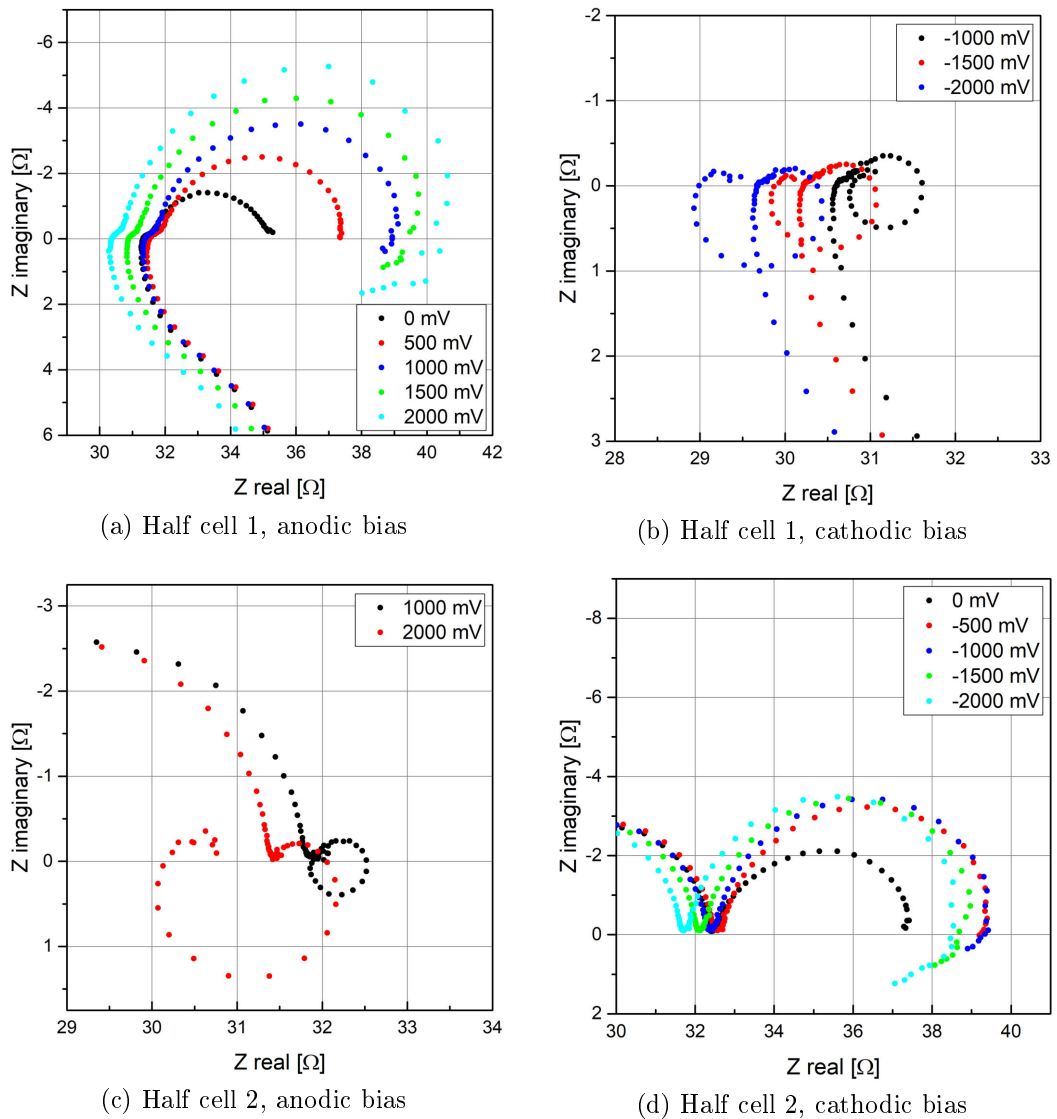
(a) Half cell 1, anodic bias

(b) Half cell 1, cathodic bias

(c) Half cell 2, anodic bias

(d) Half cell 2, cathodic bias

Figure 4.65: Impedance spectra of symmetric LSF three-electrode sample measured at 625°C set temperature in 22.5 mbar H_2 and 25 mbar H_2O under different bias voltages. As the bias voltage is always applied to the WE (half cell 1), the effective overpotential of half cell 2 is positive for cathodic bias and vice versa.

cycles and the expected increase with decreasing oxygen partial pressure. A fit of the chemical capacitance revealed a scaling of $C_{chem} \propto p(O_2)^{-0.11}$ and $C_{chem} \propto p(O_2)^{-0.17}$ for the bias cycles and $p(O_2)$ cycles, respectively.
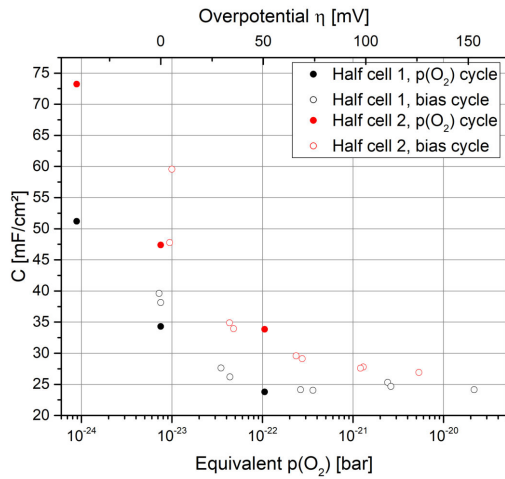
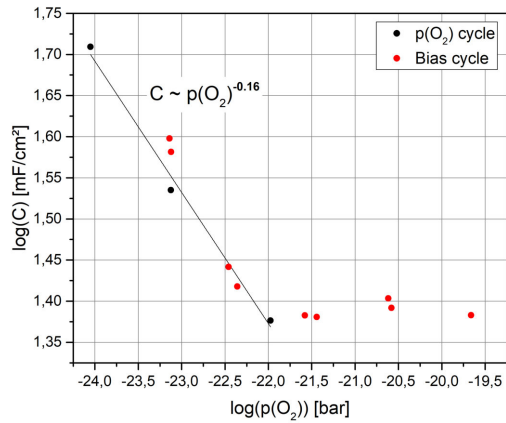The current-voltage characteristic in reducing atmospheres is depicted in Fig-
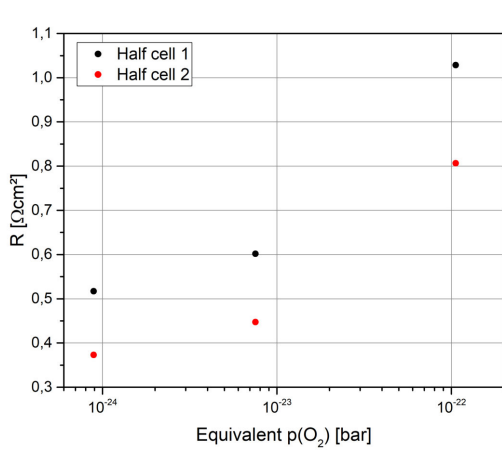
(a) Electrode resistance, p(O$_2$) cycles
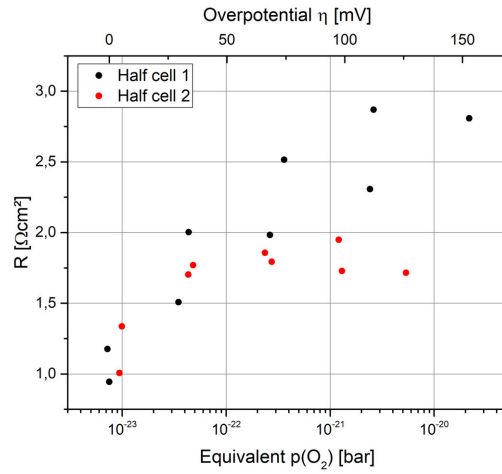
(b) Electrode resistance, bias cycles

(c) Chemical capacitance

(d) Chemical capacitance of half cell 1, fit

Figure 4.66: Resistance and chemical capacitance of symmetric LSF three-electrode sample obtained with p(O$_2$) and bias cycles at a set temperature of 625°C. Inset (a) and inset (b) depict the resistance from the p(O$_2$) and bias cycles, respectively. Inset (c) shows a comparison of the chemical capacitance of the different cycles. In inset (d) the logarithm of the chemical capacitance is fitted (thin line) over the logarithm of the oxygen partial pressure. Oxygen partial pressures with applied bias voltage were calculated from the effective overpotential of the respective electrode.
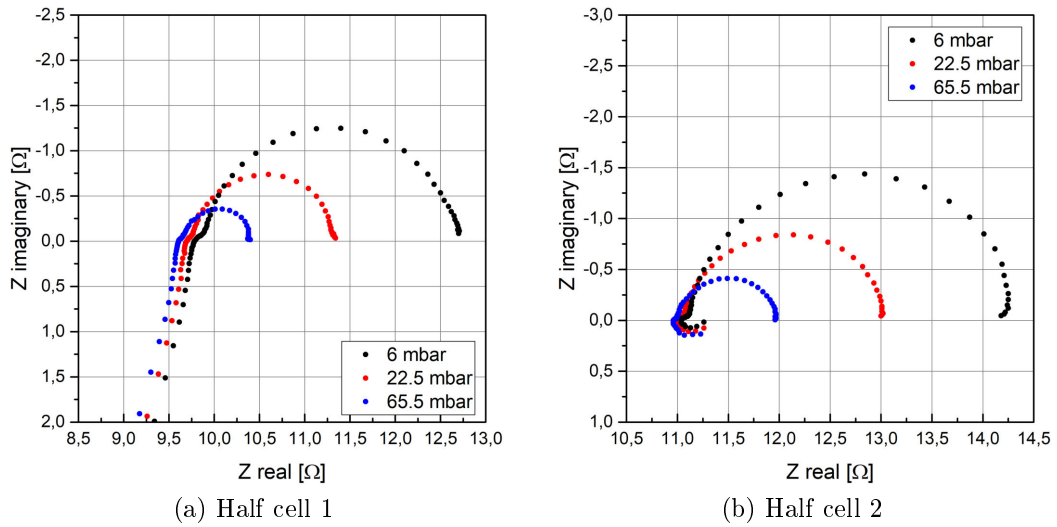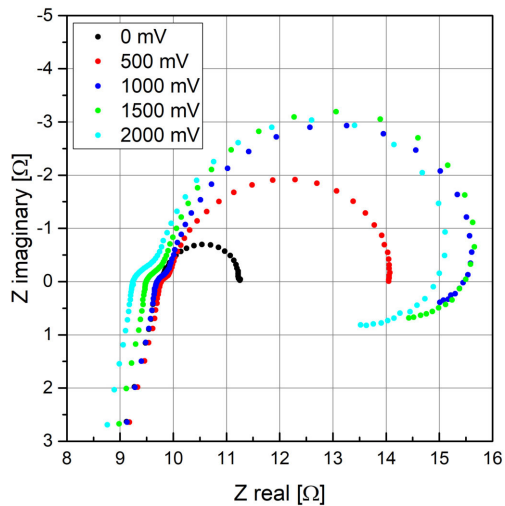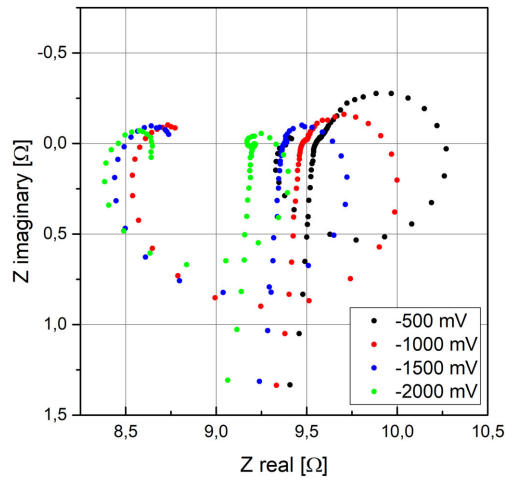
(a) Half cell 1

(b) Half cell 2

Figure 4.67: Impedance spectra of symmetric LSF three-electrode sample measured at 725°C set temperature with different hydrogen partial pressures

ure 4.70. With positive effective overpotential, the curves had a linear course that was steeper at 725°C, corresponding to smaller ASRs at higher temperatures. In the cathodic regime, the calculation of the overpotential was less accurate due to the vast artifacts in the spectra, resulting in high current densities with only little effective overpotential on the measured electrode (especially pronounced at 725°C). The fast kinetics with negative effective overpotential, potentially caused by the formation of Fe particles at the LSF surface [51], resulted in low ASRs that were significantly smaller than the measurement artifacts originating from the respective counter electrode. Analogue to the symmetric GDC sample, that resulted in the problem of different AC and DC electrolyte resistances due to a shifted equipotential surface of the reference electrode. Therefore, the effective overpotential of the measured electrode could not be accurately calculated in the cathodic regime.

Summing up, the measurement on the symmetric LSF sample yielded viable results in oxidizing and reducing conditions that were comparable to the asymmetric sample and in agreement with the expected behavior. However, the peak frequencies of the LSF electrodes were not compatible when measuring the electrode with a negative effective overpotential. In oxidizing atmospheres, this led to artifacts in the intermediate frequency that separated the electrode feature and prevented an equivalent circuit fit. In reducing atmospheres, negative overpotential drastically increased the electrode kinetics, resulting in very low ASRs, and led to
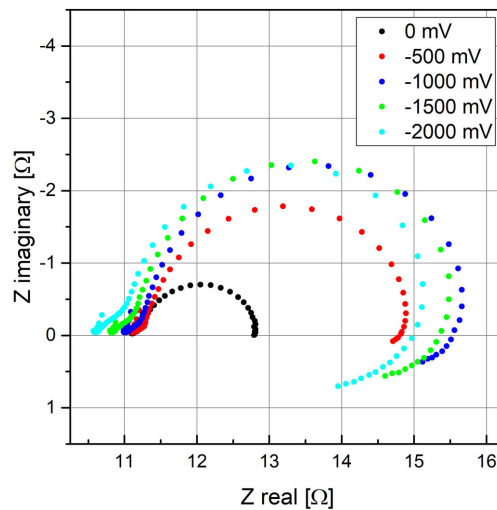
102

(a) Half cell 1, anodic bias

(b) Half cell 1, cathodic bias
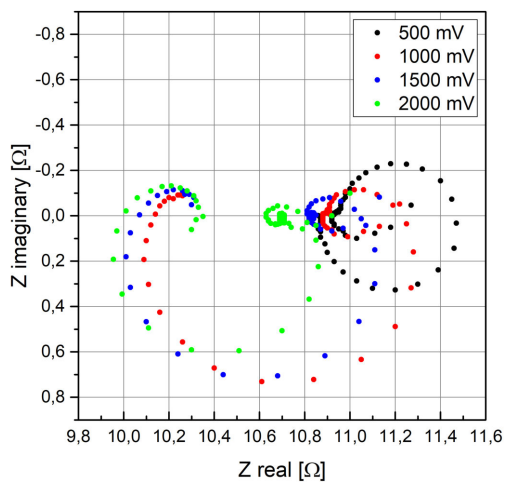
(c) Half cell 2, anodic bias

(d) Half cell 2, cathodic bias

Figure 4.68: Impedance spectra of symmetric LSF three-electrode sample measured at 725°C set temperature in 22.5 mbar H_2 and 25 mbar H_2O under different bias voltages. As the bias voltage is always applied to the WE (half cell 1), the effective overpotential of half cell 2 is positive for cathodic bias and vice versa.
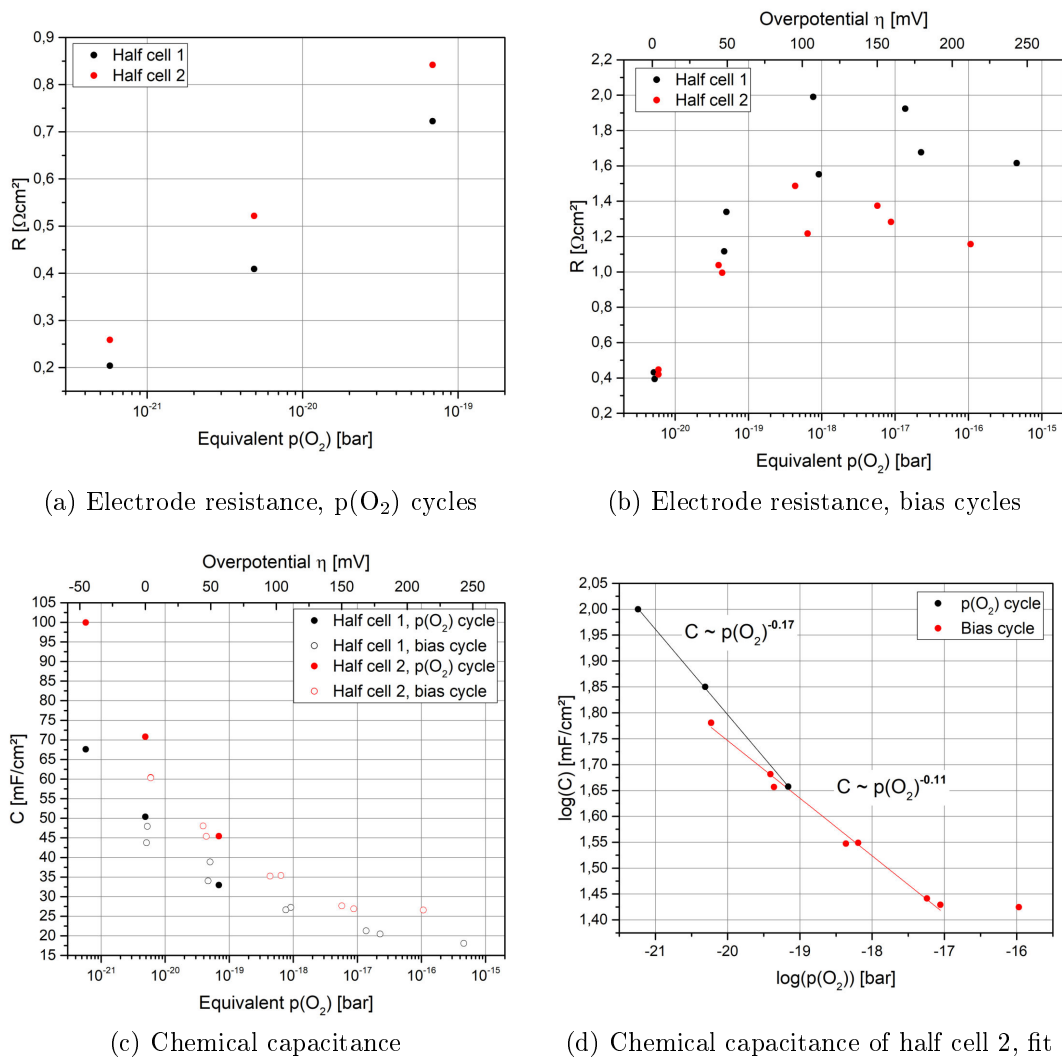
(a) Electrode resistance, p(O₂) cycles

(b) Electrode resistance, bias cycles

(c) Chemical capacitance

(d) Chemical capacitance of half cell 2, fit

Figure 4.69: Resistance and chemical capacitance of symmetric LSF three-electrode sample obtained with p(O₂) and bias cycles at a set temperature of 725°C. Inset (a) and inset (b) depict the resistance from the p(O₂) and bias cycles, respectively. Inset (c) shows a comparison of the chemical capacitance of the different cycles. In inset (d) the logarithm of the chemical capacitance is fitted (thin lines) over the logarithm of the oxygen partial pressure. Oxygen partial pressures with applied bias voltage were calculated from the effective overpotential of the respective electrode.
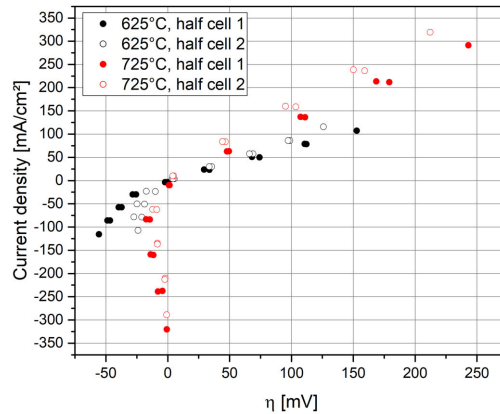
Figure 4.70: Current-voltage characteristic of the symmetric LSF three-electrode sample measured in 22.5 mbar H_2 and 25 mbar H_2O

artifacts many times larger than the electrode features. The presence of these vast artifacts indicated a significant shift of the equipotential surface of the reference electrode with changing frequencies, resulting in different AC and DC electrolyte offset resistances and therefore a distorted current-voltage characteristic.

4.2.6 Ni/GDC symmetric

The symmetric Ni/GDC three-electrode sample was prepared analogue to the other three-electrode samples by screen printing commercial NiO/GDC paste on the substrate and brushing it on the wing as reference electrode. An additional layer of NiO was brushed on the electrodes as a current collector. NiO was in situ reduced to Ni in the measuring setup. The measurements were conducted with the low pressure measuring setup in different reducing atmospheres and with applied bias voltage, as described in subsection 4.2.5. As the peak frequencies of this material were rather high, active shielding was needed to reduce the high frequency artifacts originating from the coupling capacitances. A comparison of the spectra with and without active shielding is depicted in Figure 4.71.

The measured spectra at 625°C set temperature in different atmospheres are presented in Figure 4.72. The spectra of half cell 1 consisted of a small high frequency semicircle followed by a 45° slope and a dominant low frequency feature. The high frequency semicircle was identified as an artifact since it had a corresponding inductive feature in the spectra of half cell 2 and was not visible in the full cell spectra. The spectra of half cell 2 showed a high frequency inductive artifact followed by a 45° slope and a dominant intermediate frequency feature. As the peak frequencies of half cell 1 were one order of magnitude smaller and the ASRs considerably larger than of half cell 2, the spectra of half cell 2 showed low
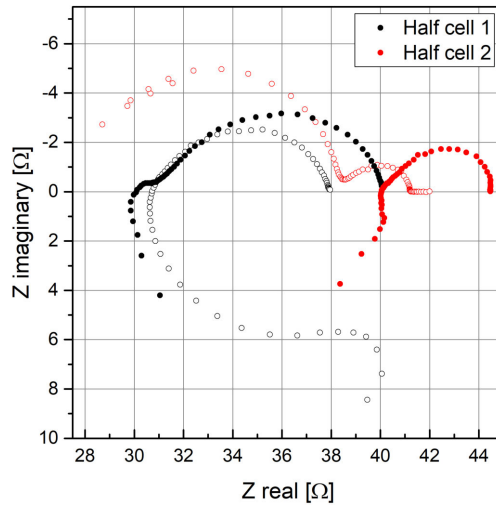
Figure 4.71: Effect of active shielding on Ni/GDC three-electrode sample measured in 6 mbar H_2 and 25 mbar H_2O around 620°C. Full symbols and open symbols represent the data with and without active shielding, respectively.

(a) Half cell 1

(b) Half cell 2
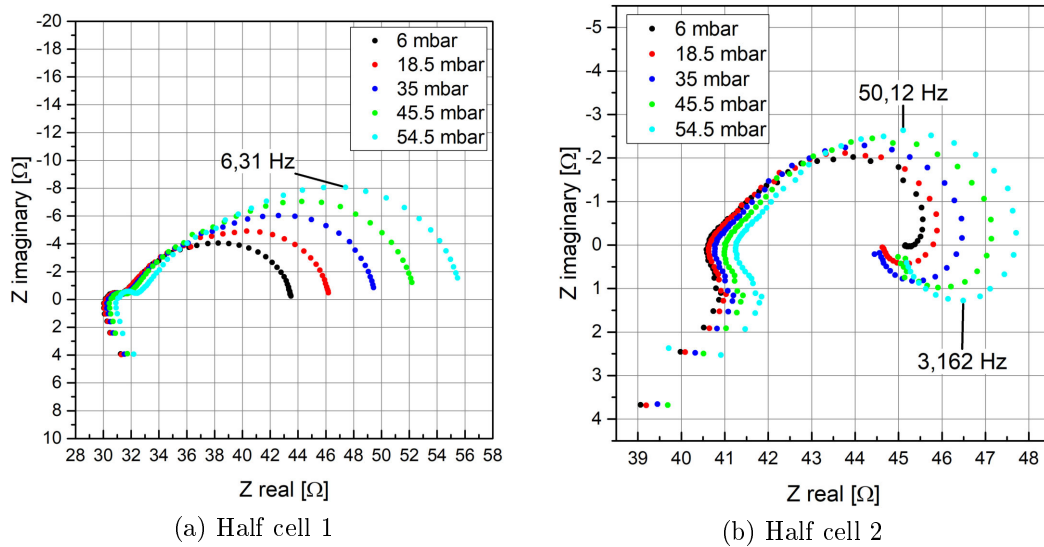
Figure 4.72: Impedance spectra of symmetric Ni/GDC three-electrode sample measured at 625°C set temperature with different hydrogen partial pressures

frequency inductive artifacts, corresponding to the features of half cell 1.

The spectra with applied bias voltage are presented in Figure 4.73. Positive

106

effective overpotential led to increased peak frequencies of the main electrode feature and the presence of low frequency inductive artifacts. Especially with half cell 2, the size of the artifacts was comparable to the size of the electrode features. Spectra with negative effective overpotential had lower peak frequencies and no inductive artifacts. However, the peak frequencies of the corresponding counter electrodes were in the range of the electrode features. For half cell 2, this led to the formation of two separate electrode features, which was clearly visible in the spectrum measured with a bias voltage of 250 mV (frequencies marked in the spectra). Since the ASRs of both half cells were rather different at nominally identical conditions, so were the full cell spectra. Positive effective overpotential on half cell 1 led to a decreased ASR that was comparable in size to the ASR of half cell 2 with negative effective overpotential. As the peak frequencies of both half cells were separated by an order of magnitude, two overlapping features were visible in the full cell spectrum. Negative effective overpotential on half cell 1 yielded large ASRs that were multiple times larger than the ASRs of half cell 2 with positive effective overpotential. Therefore, only one feature was visible in the full cell spectrum.

The spectra were fitted with the transmission line equivalent circuit as described in subsection 4.2.1. The extracted parameters are presented in Figure 4.74. The electrode resistance in different atmospheric conditions increased with progressing time, independent from the actual atmosphere. Hence degradation effects were overshadowing the influence of changing atmospheres. With applied bias voltage, the electrode resistance had a maximum around -150 mV effective overpotential and showed a sharp descent around 0 mV. Notably, the ASR of half cell 2 was smaller than the ASR of half cell 1 by a factor of 3 to 4 throughout the whole measurement. The chemical capacitance increased with decreasing partial pressure until reaching a maximum around 10^{-26} bar. Comparing the different measuring cycles and both half cells, agreement was found to some extent. However, the fit quality was questionable, especially for half cell 2 with positive effective overpotential.

The spectra measured in different atmospheres at a set temperature of 725°C are presented in Figure 4.75. Both spectra had high frequency artifacts followed by a 45° slope and a dominant low frequency feature. However, half cell 2 had vast low frequency artifact features. Again, the reasons for those were incompatible peak frequencies and large ASRs of half cell 1. As the ASR of half cell 1 was even larger than when measured at 625°C set temperature, the size of the artifacts also increased and was comparable to the size of the electrode features. The working electrode of the sample (electrode of half cell 1) crumbled away when it was removed from the sample holder, possibly explaining the increased ASR at higher temperatures.
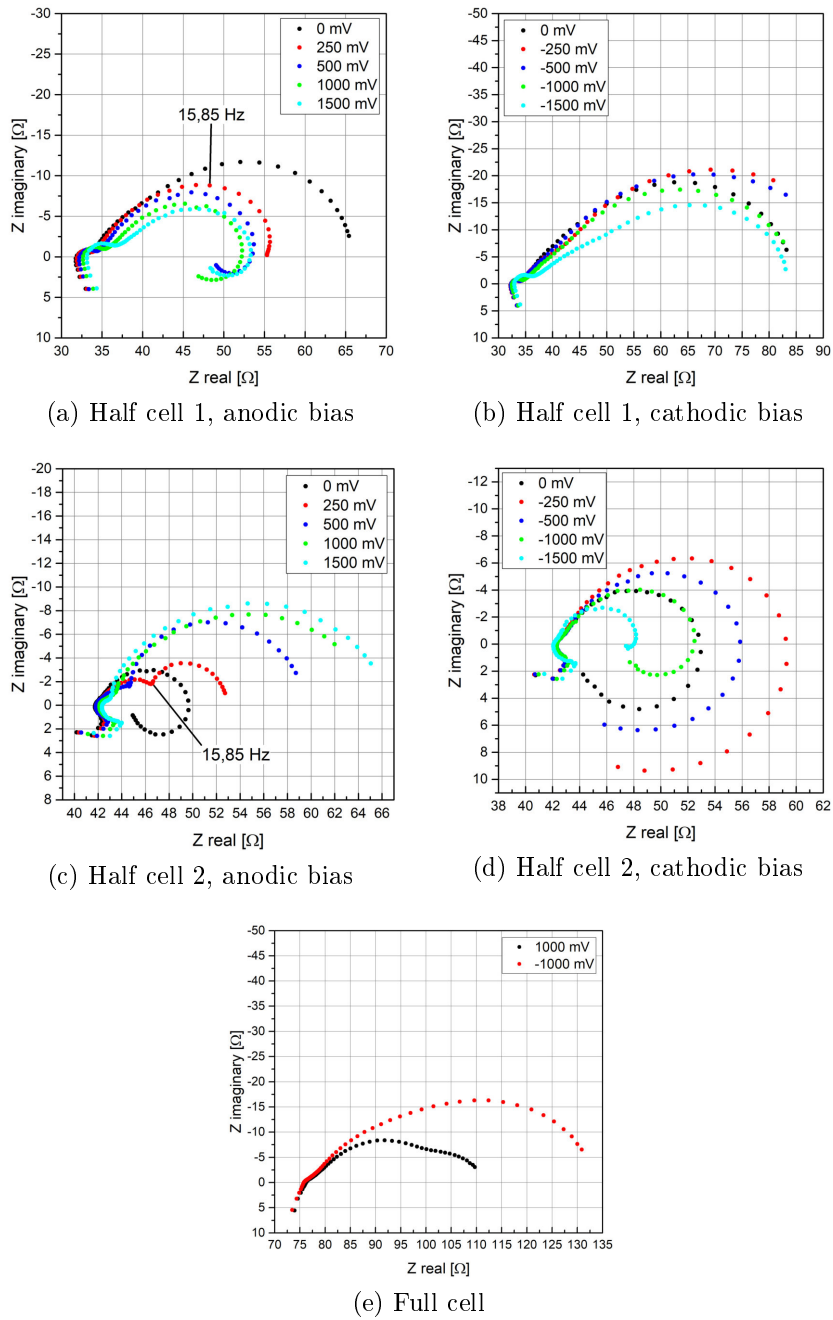
(a) Half cell 1, anodic bias
(b) Half cell 1, cathodic bias

(c) Half cell 2, anodic bias
(d) Half cell 2, cathodic bias

(e) Full cell

Figure 4.73: Impedance spectra of symmetric Ni/GDC three-electrode sample measured at 625°C set temperature in 18.5 mbar H_2 and 25 mbar H_2O under different bias voltages. As the bias voltage is always applied to the WE (half cell 1), the effective overpotential of half cell 2 is positive for cathodic bias and vice versa.
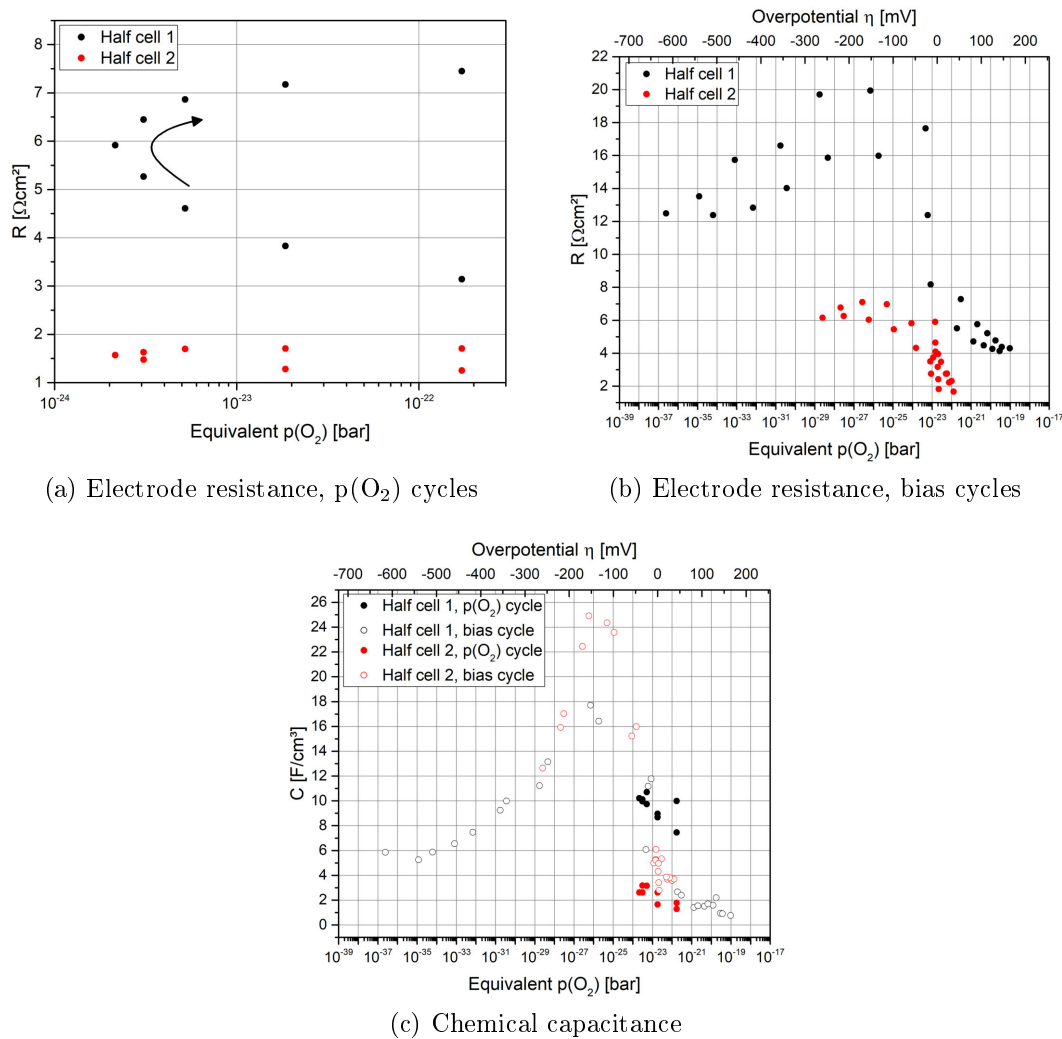
(a) Electrode resistance, p(O$_2$) cycles

(b) Electrode resistance, bias cycles

(c) Chemical capacitance

Figure 4.74: Resistance and chemical capacitance of symmetric Ni/GDC three-electrode sample obtained with p(O$_2$) and bias cycles at a set temperature of 625°C. Inset (a) and inset (b) depict the resistance from the p(O$_2$) and bias cycles, respectively. The arrow in inset (a) indicates the succession of measurements. Inset (c) shows a comparison of the chemical capacitance of the different cycles. Oxygen partial pressures with applied bias voltage were calculated from the effective overpotential of the respective electrode.

The spectra with applied bias voltage are presented in Figure 4.76. Analogue to the previous measurements, positive effective overpotential led to higher peak frequencies and the presence of low frequency artifacts, whereas negative effective
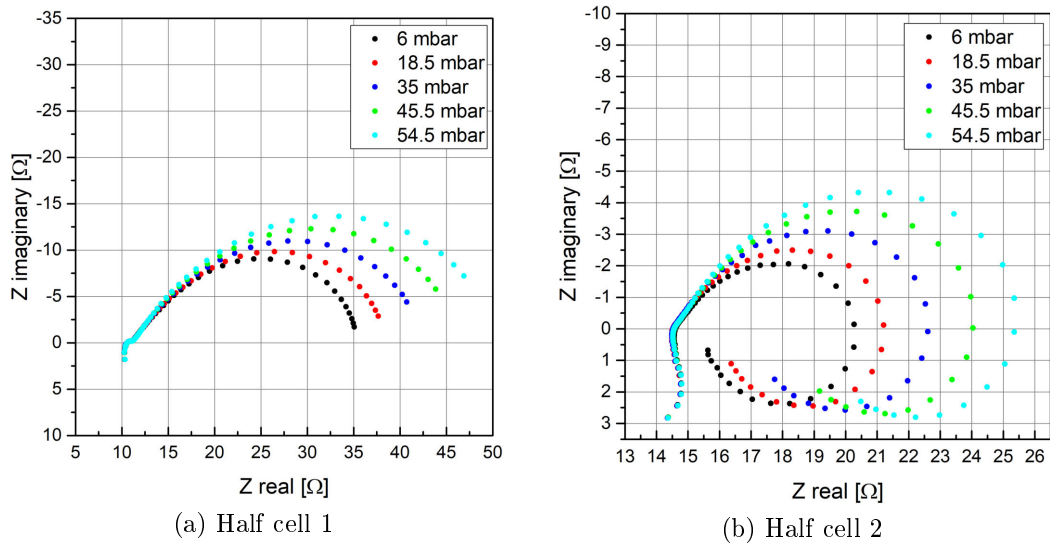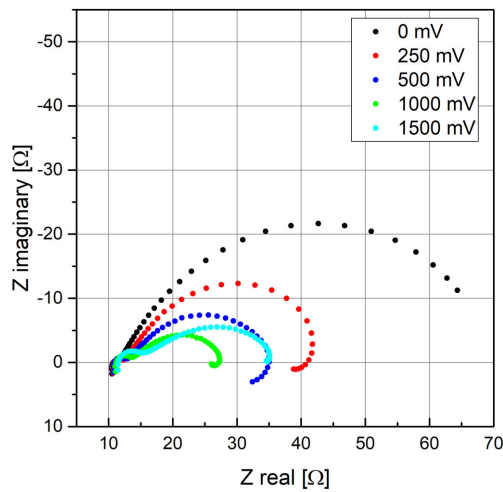
(a) Half cell 1

(b) Half cell 2

Figure 4.75: Impedance spectra of symmetric Ni/GDC three-electrode sample measured at 725°C set temperature with different hydrogen partial pressures

overpotential resulted in lower peak frequencies. However, the size of the artifacts was considerably smaller than at 625°C. Notably, the shape of the dominant feature of half cell 2 was a more or less pronounced semicircle over the whole bias range. For half cell 1, the feature was depressed at elevated bias voltages.

The spectra measured in different atmospheres were fitted with the transmission line equivalent circuit. With applied bias voltage, the fit with the transmission line did not yield satisfying results for all spectra. Therefore, some spectra had to be fitted with an R||CPE element instead. Generally, the quality of the equivalent circuit fit was questionable. The extracted parameters are presented in Figure 4.77. The electrode resistance in different atmospheres again increased with progressing time and was not influenced by different conditions. Both half cells had larger ASRs than when measured at 625°C, however the ASR of half cell 1 was considerably larger. With applied bias voltage, the scaling of the electrode resistance with effective overpotential was consistent for both half cells, with a maximum around -200 mV and a minimum around +200 mV effective overpotential. As the quality of the equivalent circuit fit was not satisfying, so was the extracted chemical capacitance. However, general trends were observable: increasing chemical capacitance with decreasing oxygen partial pressure until reaching a maximum around 10^{-21} bar and decreasing with lower pressures.
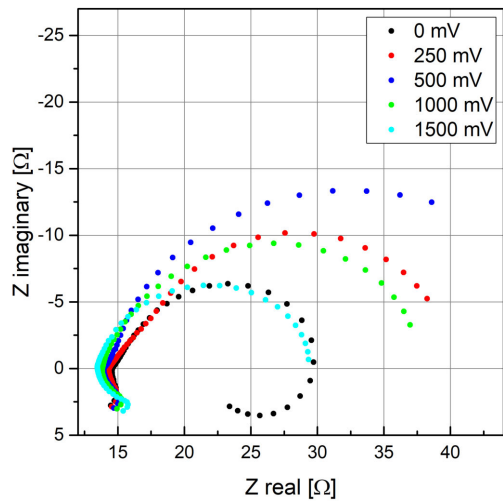
The current-voltage characteristics are depicted in Figure 4.78. Generally, the curves had a steeper course in the anodic regime than in the cathodic. At 625°C

110

(a) Half cell 1, anodic bias
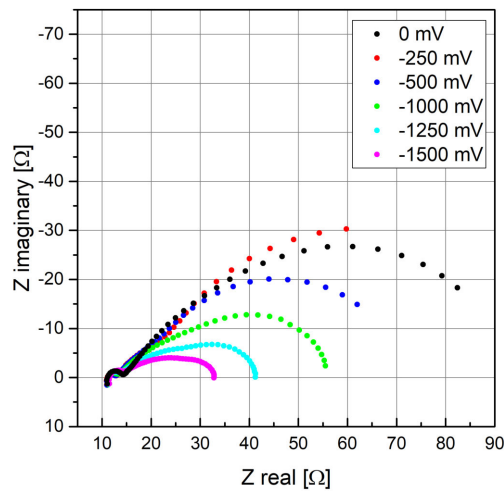
(b) Half cell 1, cathodic bias

(c) Half cell 2, anodic bias
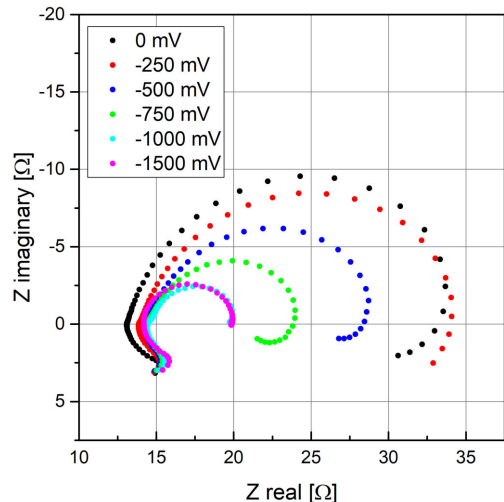
(d) Half cell 2, cathodic bias

Figure 4.76: Impedance spectra of symmetric Ni/GDC three-electrode sample measured at 725°C set temperature in 18.5 mbar H_2 and 25 mbar H_2O under different bias voltages. As the bias voltage is always applied to the WE (half cell 1), the effective overpotential of half cell 2 is positive for cathodic bias and vice versa.

and with positive effective overpotential, the curve of half cell 2 was defined by the vast low frequency artifacts. Analogue to previous samples, those resulted in the problem of different AC and DC electrolyte resistances. As the size of the artifacts at 725°C was considerably smaller, the course of the curve at this temperature

(a) Electrode resistance, p(O₂) cycles

(b) Electrode resistance, bias cycles

(c) Chemical capacitance
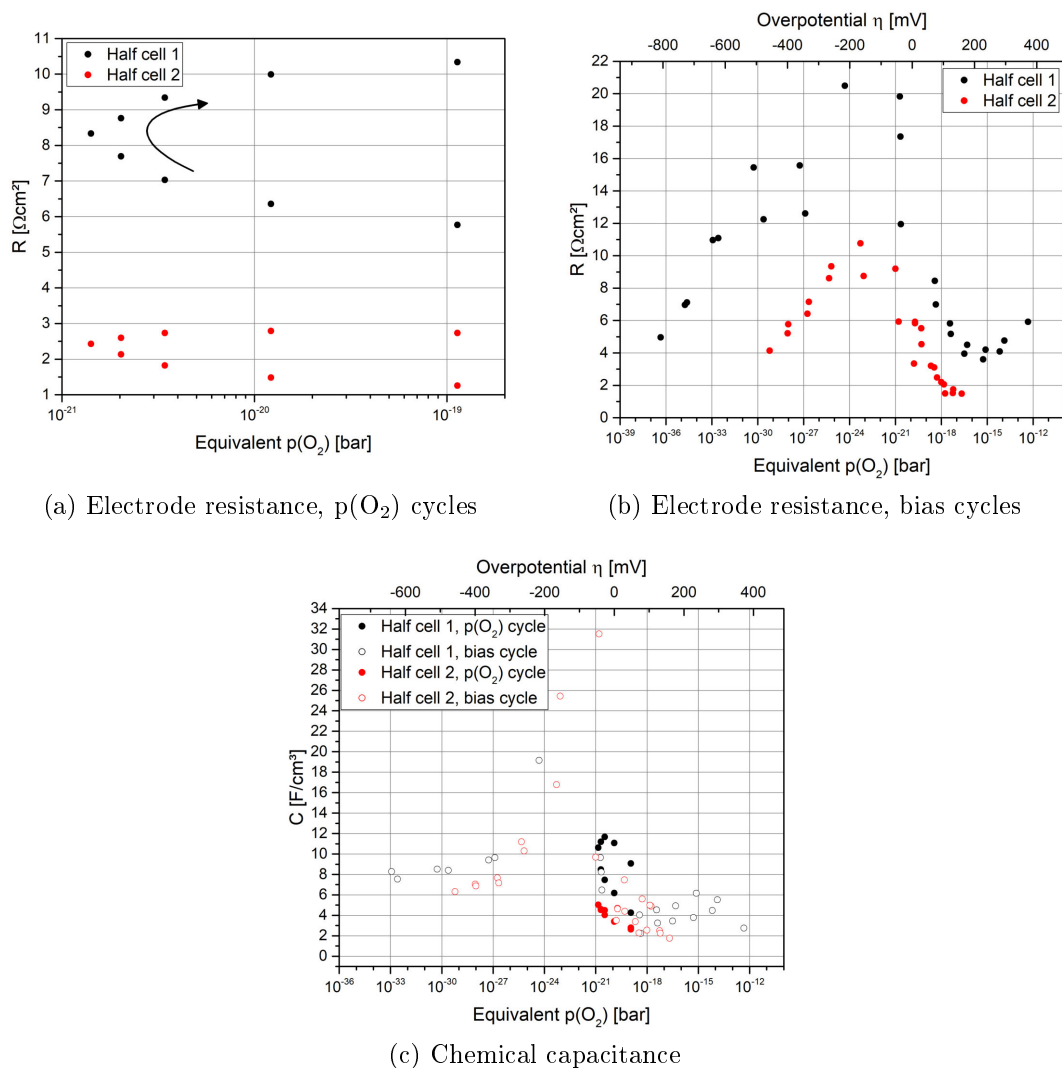
Figure 4.77: Resistance and chemical capacitance of symmetric Ni/GDC three-electrode sample obtained with p(O$_2$) and bias cycles at a set temperature of 725°C. Inset (a) and inset (b) depict the resistance from the p(O$_2$) and bias cycles, respectively. The arrow in inset (a) indicates the succession of measurements. Inset (c) shows a comparison of the chemical capacitance of the different cycles. Oxygen partial pressures with applied bias voltage were calculated from the effective overpotential of the respective electrode.

Figure 4.78: Current-voltage characteristic of the symmetric Ni/GDC three-electrode sample measured in 18.5 mbar H_2 and 25 mbar H_2O

was less impaired. For half cell 1, the curves at both temperatures were almost identical with a slightly steeper course in the anodic regime at 625°C.

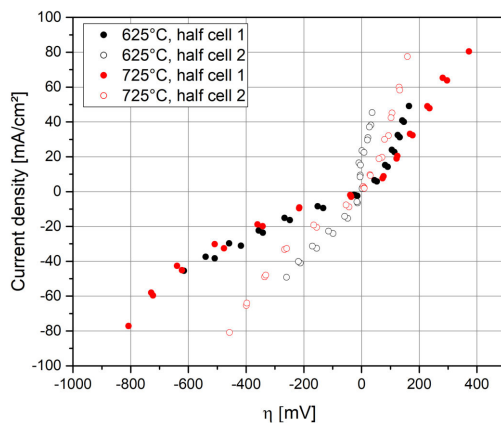The measurements on the symmetric Ni/GDC three-electrode sample yielded to some extent unexpected results. The presence of vast low frequency artifacts without applied bias was not expected as the electrodes were nominally identical. However, differences in the peak frequency of an order of magnitude and considerably larger ASRs with the respective counter electrode, fulfilled the requirements for the presence of artifacts that were found with earlier measurements. Apart from that, the ASR increased with increasing temperature which was not observed with any other sample. Possible reasons were strong degradation or the delamination of the electrode which was observed when the sample was removed.

4.2.7 Pedestal design

Lastly, a new three-electrode design was tested where the small WE was on an electrolyte pedestal surrounded by the RE, see Figure 4.79a. With this setup the equipotential surfaces within the pedestal should be plane parallel and equidistant, resulting in less artifacts. For that, NiO/GDC electrode paste was screen printed on the top and bottom of a 10 mm x 10 mm x 7 mm YSZ block. To ensure good electrical contact, NiO was brushed on the electrodes as a current collector. The sample was then sintered in reducing conditions (2.5% H_2 + H_2O) with the parameters given in Table 3.2. To fabricate the pedestal, a milling machine was used to mill a groove around the designated working electrode. Different heights of the pedestal and sizes of the working electrode were tested. However, due to the conical shape of the milling tool, a high pedestal resulted in smaller electrodes that were difficult to contact in the measuring setup. The combination that worked best

was a pedestal height of approximately 500 μm and a nominal electrode diameter of 1 mm. Figure 4.79b shows a microscope image of that electrode. Parts of the electrode were scraped off around the circumference due to the machining. As the milling program was not perfectly set (clean outer rim instead of clean inner rim), a portion of the electrode was also milled away.
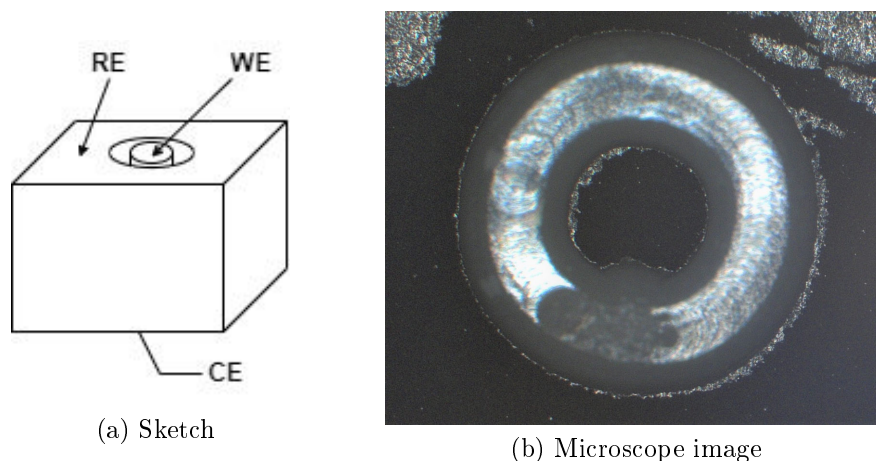

(a) Sketch

(b) Microscope image

Figure 4.79: Pedestal three-electrode sample

The sample was measured in a 4-point configuration without the trigger box. Therefore, only the spectra of the WE against the RE were recorded. The measurement was conducted with an excitation voltage of 0.1 V rms in 2.5% H_2 + H_2O at 650°C and 750°C set temperature. The spectra measured at 650°C set temperature are presented in Figure 4.80a-b. Due to the smaller WE, the electrolyte resistance and the electrode arc were much larger than for the wing samples. Under anodic bias, the spectra consisted of a dominant low frequency semicircle (peak frequency around 1 Hz) that decreased in size until a bias voltage of +400 mV. Applying higher bias voltage resulted in the presence of a high frequency shoulder that increased in size with increasing bias. Apart from that, the spectra showed the onset of a low frequency feature that was not fully included in the measured frequency range. Under moderate cathodic bias, the spectra had the transmission line shape with a 45° slope followed by a dominant low frequency feature. However, most spectra had a plateau shape that did not allow fitting with an equivalent circuit. The size of the electrode feature drastically decreased in size when applying -1000 mV. The spectra measured at 750°C set temperature are presented in Figure 4.80c-d and showed the same trends as those measured at 650°C. Starting with -400 mV, however, low frequency inductive artifacts were visible in the spectra.

If possible, the spectra were fitted with a series connection of an offset resistance and a single R||CPE element. The extracted parameters are presented in

(a) 650°C, anodic bias

(b) 650°C, cathodic bias

(c) 750°C, anodic bias

(d) 750°C, cathodic bias
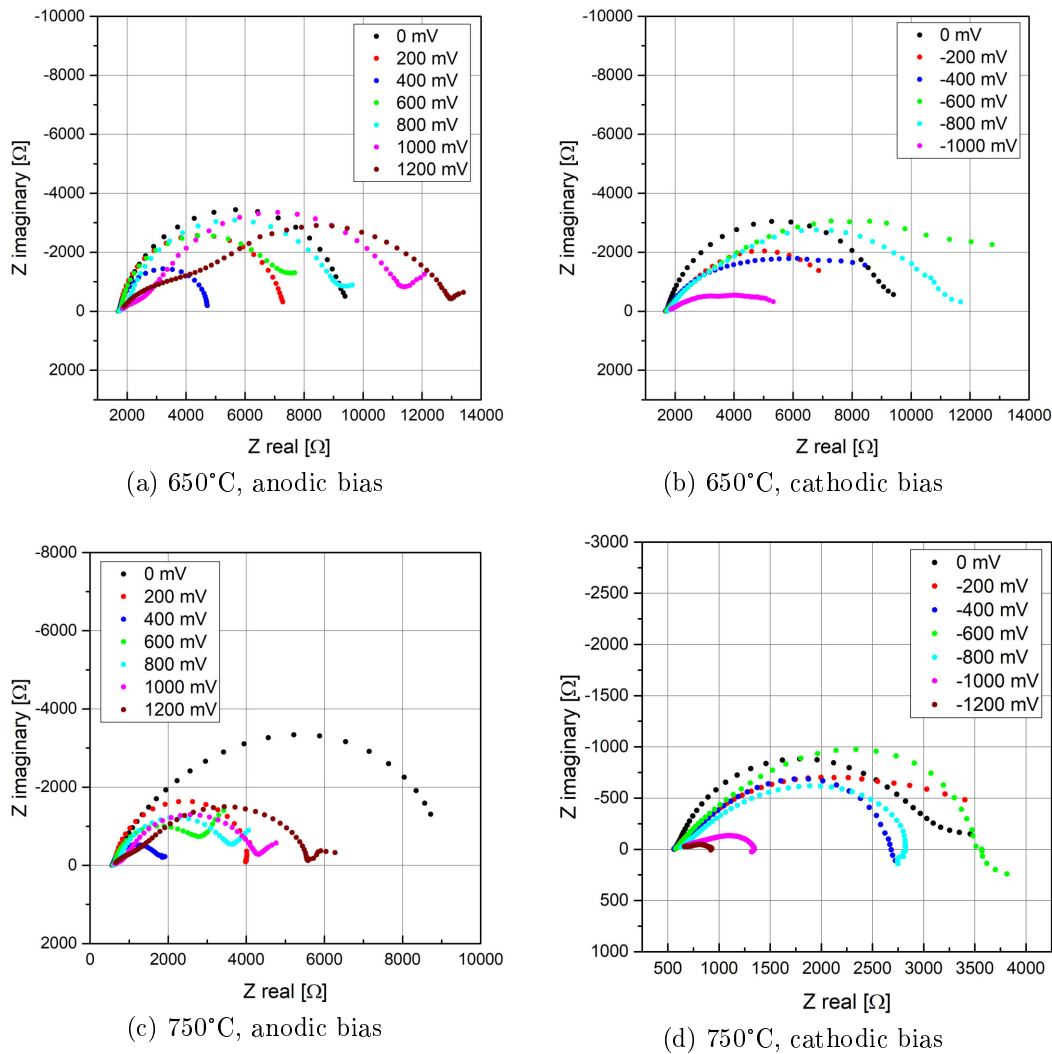
Figure 4.80: Impedance spectra of pedestal three-electrode sample with Ni/GDC electrodes measured under different bias voltages

Figure 4.81. The electrode resistance had a minimum around 250 mV effective overpotential and increased with increasing bias voltage. Lowering the bias, resulted in a sharp increase until reaching a maximum around -250 mV, followed by a decrease in the more cathodic regime. This behavior was also observed with the Ni/GDC wing sample, see Figure 4.77. However, the high electrode resistances were all measured while increasing the bias from the most negative bias voltage of -1200 mV. The chemical capacitance was rather constant under moderate anodic bias and slightly decreased under high positive bias. With negative applied bias

(a) Electrode resistance, 650°C

(b) Chemical capacitance, 650°C

(c) Electrode resistance, 750°C

(d) Chemical capacitance, 750°C
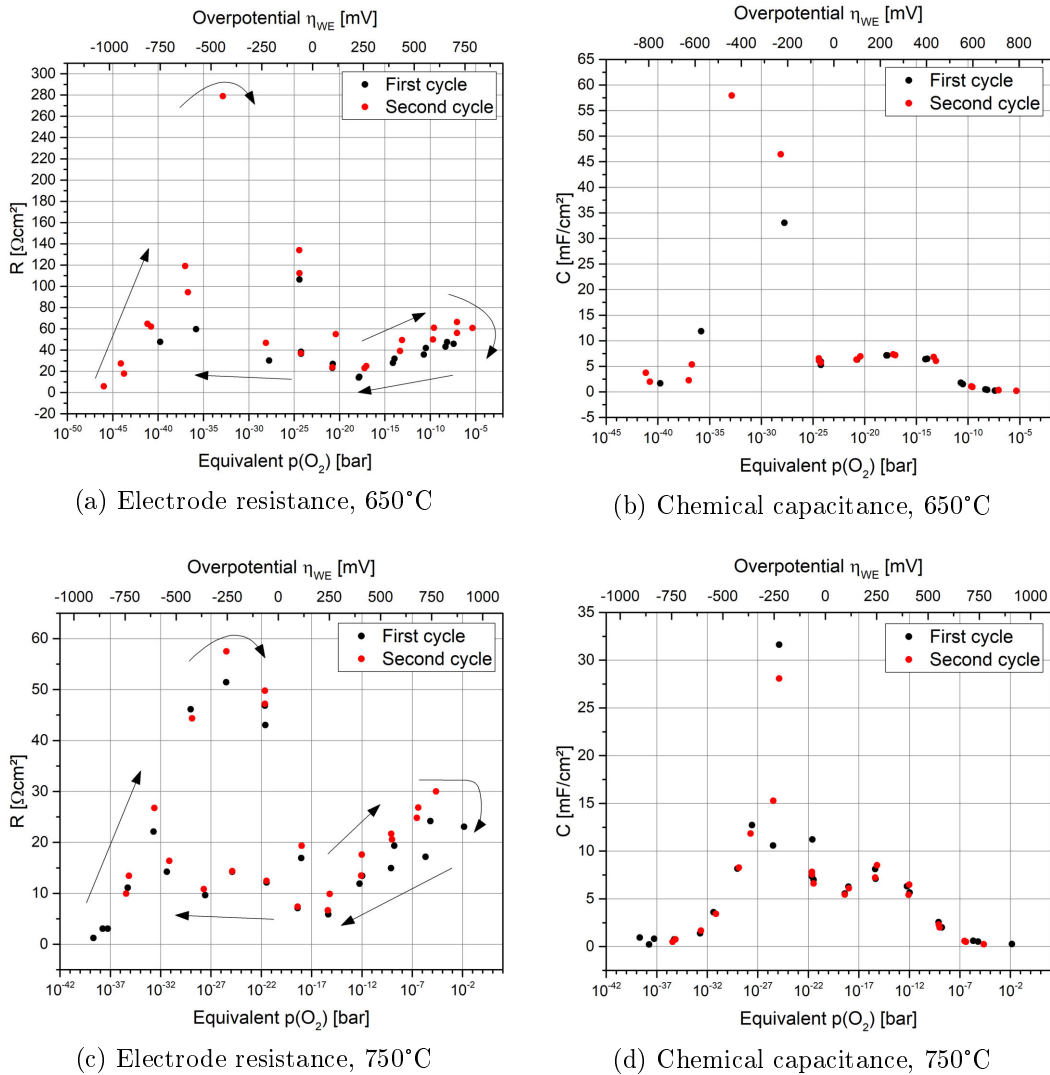
Figure 4.81: Resistance and chemical capacitance of pedestal three-electrode sample with Ni/GDC electrodes. Data was obtained with two bias cycles at both temperatures. The arrows are indicating the succession of the measurement. Oxygen partial pressures were calculated from the effective overpotential of the working electrode.

voltage, the chemical capacitance also had a maximum around -250 mV and decreased with more cathodic bias. Again, similar scaling was found with previous measurements.

The current-voltage characteristics are depicted in Figure 4.82. In the cathodic regime, the curves were flat over a wide bias range, but showed a drastic descend

at very high cathodic bias, corresponding to the sudden decrease of the electrode resistance. Apart from that, the changed behavior with descending and increasing bias was also visible as different courses for the curves at 750°C. In the anodic regime, the curves were slightly steeper than with cathodic bias.
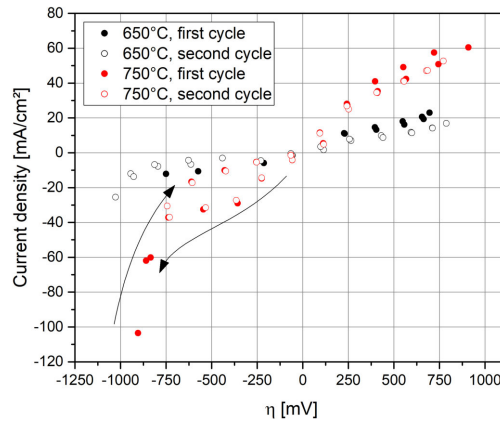
Figure 4.82: Current-voltage characteristic of the pedestal three-electrode sample with Ni/GDC electrodes. The arrows are indicating the succession of the measurement.

The measurements on the pedestal three-electrode sample yielded viable results that were in parts comparable to the measurements conducted on wing samples. As this was only a test sample, the machining was not perfected and influenced the performance of the electrodes (shape of electrode spectra, increased ASR compared to wing sample). Notably, only few and small inductive artifacts were visible in the spectra, indicating that this setup is a promising choice for three-electrode measurements. However, electrode materials or fabrication techniques need to be optimized in order to obtain meaningful results.

5 Conclusion and Outlook

In the course of this thesis, porous three-electrode samples in a newly developed "wing" geometry were produced and investigated with electrochemical impedance spectroscopy. The main goal was to explore under which conditions virtually artifact-free half cell spectra can be measured. To test the measurement setup and obtain reference results, first measurements were conducted on regular two-electrode samples with porous and thin film electrodes. The three-electrode samples were produced with symmetric and asymmetric electrode configurations and were measured in changing oxidizing and reducing atmospheres, as well as with applied bias voltage. To explore the optimal choice of working and counter electrode materials, a variety of materials was tested: porous LSF and GDC, as well as cermets of Pt/YSZ, Ni(O)/YSZ and Ni(O)/GDC. The following conclusions can be drawn:

- Generally, two artifact sources were relevant for the measurements. The coupling capacitance of the reference electrode measuring line to its grounded shield resulted in high frequency artifacts that were visible in almost all measured three-electrode spectra. Through the implementation of active shielding, however, the significance of these artifacts was reduced. This was especially needed for electrodes with high peak frequencies such as Ni/GDC, Ni/YSZ and Pt/YSZ. The other artifact source was a frequency dependent current distribution that resulted in artifacts in the frequency range of the respective counter electrode. These artifacts were possibly problematic as they could occur in the same frequency range as the electrode features and therefore heavily distort the spectra.

- The measurements with an asymmetric electrode setup yielded more consistent results than with symmetric samples. With symmetric samples, the electrodes should have equal properties when measured at open-circuit voltage. However, the measurements revealed that the peak frequencies of nominally identical electrodes differed by up to one order of magnitude. As a consequence, low frequency inductive artifacts were visible in the spectra of the half cell with higher peak frequencies even at open-circuit voltage. When applying bias voltage, intermediate frequency artifacts often distorted the spectra of the electrode with lower peak frequencies, preventing an equivalent circuit fit. With asymmetric samples, the electrode materials were

chosen in a way that the peak frequencies were well separated, even with applied bias voltage.

- In strongly reducing conditions with very low H_2O partial pressure, gas diffusion became relevant for Ni/YSZ electrodes and resulted in features in the frequency range of 1 Hz. As the electrode features of typical MIEC electrodes are also in this frequency range, conditions where gas diffusion limitation is crucial should be avoided, e.g. by measuring in pure $H_2 + H_2O$ at low pressure.

- Not only the frequency range, but also the size of artifacts resulting from a frequency dependent current distribution, was defined by the electrode feature of the counter electrode. When measuring samples with kinetically fast WEs and considerably slower CEs, the spectra often contained artifact features that were larger than the electrode features. This resulted in erroneous electrolyte offset resistances and impaired the equivalent circuit fits (especially with intermediate frequency artifacts). Hence, CEs with low electrode resistances are preferable.

- Meaningful results could be obtained from three-electrode measurements, even if artifacts were present in the spectra. If the artifacts were well separated from the electrode feature, they did not affect the electrode properties. As a result, fitting with the physically motivated transmission line equivalent circuit was possible for selected samples, like porous LSF, and extracted parameters were comparable to defect model calculations.

- The pedestal three-electrode setup turned out to be a promising choice for low artifact three-electrode measurements due to the relatively larger CE.

The combination of a MIEC electrode material with low peak frequencies and a cermet electrode with high peak frequencies (Pt/YSZ and Ni/YSZ in oxidizing and reducing atmospheres, respectively) was most suitable for meaningful three-electrode measurements. Even with applied bias voltage, the peak frequencies of the cermet electrodes were in the range of 10^3 Hz, whereas the peak frequencies of the MIEC electrode were at least two orders of magnitude below that. To prevent gas diffusion limitation, measurements can be conducted in a low pressure measuring setup.

Further investigation should be conducted on the pedestal design. Therefore, establishing a clean preparation routine is needed to produce electrodes that are not influenced by the machining. Measurements with different electrode combinations are required to reveal the full potential of this setup concerning the proneness to artifacts.

Bibliography

[1]   W. M. Organization. *Golbal Temperature for warmest years on record.* URL: https://public.wmo.int/en/media/news/2019-set-be-2nd-or-3rd-warmest-year-record (visited on 12/30/2019).

[2]   A. Züttel, A. Borgschulte, and L. Schlapbach. *Hydrogen as a Future Energy Carrier.* WILEY-VCH, 2008. DOI: 10.1002/9783527622894.

[3]   F. Gardner, M. Day, N. Brandon, M. Pashley, and M. Cassidy. "SOFC technology development at Rolls-Royce". In: *Journal of Power Sources* 86.1 (2000), pp. 122–129. DOI: https://doi.org/10.1016/S0378-7753(99)00428-0.

[4]   J. Larminie. *Fuel Cell Systems Explained.* 2. Edition. New York: J. Wiley, 2003. ISBN: 978-0-768-01259-0.

[5]   R. O'Hayre, S.-W. Cha, W. Colella, and F. B. Prinz. *Fuel Cell Fundamentals.* 3. Edition. New York: John Wiley and Sons, 2016. ISBN: 978-1-119-11415-4.

[6]   M. Hubert, J. Laurencin, P. Cloetens, B. Morel, D. Montinaro, and F. Lefebvre-Joud. "Impact of Nickel agglomeration on Solid Oxide Cell operated in fuel cell and electrolysis modes". In: *Journal of Power Sources* 397 (Sept. 2018), pp. 240–251. DOI: 10.1016/j.jpowsour.2018.06.097.

[7]   D. K. Niakolas. "Sulfur poisoning of Ni-based anodes for Solid Oxide Fuel Cells in H/C-based fuels". In: *Applied Catalysis A: General* 486 (Sept. 2014), pp. 123–142. DOI: 10.1016/j.apcata.2014.08.015.

[8]   H. Monzón and M. Laguna-Bercero. "Redox-cycling studies of anode-supported microtubular solid oxide fuel cells". In: *International Journal of Hydrogen Energy* 37.8 (Apr. 2012), pp. 7262–7270. DOI: 10.1016/j.ijhydene.2011.10.026.

[9]   I. Yasuda, K. Ogasawara, M. Hishinuma, T. Kawada, and M. Dokiya. "Oxygen tracer diffusion coefficient of $(La,Sr)MnO_{3\pm\delta}$". In: *Solid State Ionics* 86-88 (1996), pp. 1197–1201. DOI: 10.1016/0167-2738(96)00287-1.

[10] M. Patrakeev, I. Leonidov, V. Kozhevnikov, and K. Poeppelmeier. "p-Type electron transport in $La_{1-x}Sr_xFeO_{3-\delta}$ at high temperatures". In: *Journal of Solid State Chemistry* 178.3 (2005), pp. 921–927. DOI: https://doi.org/10.1016/j.jssc.2004.10.038.

[11] S. Kogler, A. Nenning, G. M. Rupp, A. K. Opitz, and J. Fleig. "Comparison of Electrochemical Properties of $La_{0.6}Sr_{0.4}FeO_{3-\delta}$ Thin Film Electrodes: Oxidizing vs. Reducing Conditions". In: *Journal of The Electrochemical Society* 162.3 (2015), F317–F326. DOI: 10.1149/2.0731503jes.

[12] F. W. Poulsen and N. van der Puil. "Phase relations and conductivity of Sr- and La-zirconates". In: *Solid State Ionics* 53-56 (1992), pp. 777–783. DOI: https://doi.org/10.1016/0167-2738(92)90254-M.

[13] A. Schmid, G. M. Rupp, and J. Fleig. "How To Get Mechanistic Information from Partial Pressure-Dependent Current–Voltage Measurements of Oxygen Exchange on Mixed Conducting Electrodes". In: *Chemistry of Materials* 30.13 (2018), pp. 4242–4252. DOI: 10.1021/acs.chemmater.8b00597.

[14] K. Eguchi, T. Setoguchi, T. Inoue, and H. Arai. "Electrical properties of ceria-based oxides and their application to solid oxide fuel cells". In: *Solid State Ionics* 52.1 (1992), pp. 165–172. DOI: 10.1016/0167-2738(92)90102-U.

[15] E. Ruiz-Trejo and J. Maier. "Electronic Transport in Single Crystals of Gd-Doped Ceria". In: *Journal of The Electrochemical Society* 154.6 (2007), B583–B587. DOI: 10.1149/1.2722530.

[16] P. Velicsanyi, M. Gerstl, A. Nenning, H. Hutter, J. Fleig, and A. K. Opitz. "The Effect of Mn Co-doping on the Electrochemical Properties of $Gd_{0.2}Ce_{0.8}O_{1.9-\delta}$/Pt Model-composite Electrodes". In: *ECS Transactions* 68.1 (July 17, 2015), pp. 1509–1516. DOI: 10.1149/06801.1509ecst.

[17] H. Finklea, X. Chen, K. Gerdes, S. Pakalapati, and I. Celik. "Analysis of SOFCs Using Reference Electrodes". In: *Journal of The Electrochemical Society* 160.9 (2013), F1055–F1066. DOI: 10.1149/2.093309jes.

[18] G. Fafilek. "The use of voltage probes in impedance spectroscopy". In: *Solid State Ionics* 176.25 (Aug. 15, 2005), pp. 2023–2029. DOI: 10.1016/j.ssi.2004.06.024.

[19] S. B. Adler. "Reference Electrode Placement in Thin Solid Electrolytes". In: *Journal of The Electrochemical Society* 149.5 (2002), E166–E172. DOI: 10.1149/1.1467368.

[20] M. Cimenti, A. C. Co, V. I. Birss, and J. M. Hill. "Distortions in Electrochemical Impedance Spectroscopy Measurements Using 3-Electrode Methods in SOFC. I – Effect of Cell Geometry". In: *Fuel Cells* 7.5 (2007), pp. 364–376. DOI: 10.1002/fuce.200700019.

[21]   M. Cimenti, V. I. Birss, and J. M. Hill. "Distortions in Electrochemical Impedance Spectroscopy Measurements Using 3-Electrode Methods in SOFC. II. Effect of Electrode Activity and Relaxation Times". In: *Fuel Cells* 7.5 (2007), pp. 377–391. DOI: 10.1002/fuce.200700020.

[22]   J. Winkler, P. V. Hendriksen, N. Bonanos, and M. Mogensen. "Geometric Requirements of Solid Electrolyte Cells with a Reference Electrode". In: *Journal of The Electrochemical Society* 145.4 (1998), pp. 1184–1192. DOI: 10.1149/1.1838436.

[23]   L. A. Dunyushkina, Y. Lu, and S. B. Adler. "Microelectrode Array for Isolation of Electrode Polarization on Planar Solid Electrolytes". In: *Journal of The Electrochemical Society* 152.8 (2005), A1668–A1676. DOI: 10.1149/1.1945729.

[24]   R. Schlesinger. "Modeling and evaluation of three-terminal impedance measurement configurations for solid oxide fuel cell electrodes". diploma thesis. Technische Universität Wien, 2018.

[25]   C. Breitkopf and K. Swider-Lyons. *Springer Handbook of Electrochemical Energy*. 1st ed. 2017. Berlin, Heidelberg: Springer, 2016. ISBN: 978-3-662-46657-5.

[26]   C. G. Zoski. *Handbook of Electrochemistry*. Amsterdam: Elsevier, 2007. ISBN: 978-0-444-51958-0.

[27]   S. P. Jiang and Y. Yan. *Materials for High-Temperature Fuel Cells*. New York: John Wiley and Sons, 2013. ISBN: 978-3-527-64428-5.

[28]   Z. Shao and M. O. Tadé. *Intermediate-Temperature Solid Oxide Fuel Cells - Materials and Applications*. 1st ed. 2016. Berlin, Heidelberg: Springer, 2016. ISBN: 978-3-662-52936-2.

[29]   M. Kuhn, S. Hashimoto, K. Sato, K. Yashiro, and J. Mizusaki. "Oxygen nonstoichiometry, thermo-chemical stability and lattice expansion of $La_{0.6}Sr_{0.4}FeO_{3-\delta}$". In: *Solid State Ionics* 195.1 (2011), pp. 7–15. DOI: https://doi.org/10.1016/j.ssi.2011.05.013.

[30]   J. Mizusaki, T. Sasamoto, W. R. Cannon, and H. K. Bowen. "Electronic Conductivity, Seebeck Coefficient, and Defect Structure of $LaFeO_3$". In: *Journal of the American Ceramic Society* 65.8 (1982), pp. 363–368. DOI: 10.1111/j.1151-2916.1982.tb10485.x.

[31]   A. Schmid, G. M. Rupp, and J. Fleig. "Voltage and partial pressure dependent defect chemistry in $(La,Sr)FeO_{3-\delta}$ thin films investigated by chemical capacitance measurements". In: *Physical Chemistry Chemical Physics* 20.17 (2018), pp. 12016–12026. DOI: 10.1039/C7CP07845E.

[32] W. C. Chueh and S. M. Haile. "Electrochemical studies of capacitance in cerium oxide thin films and its relationship to anionic and electronic defect densities". In: *Physical Chemistry Chemical Physics* 11.37 (2009), pp. 8144–8148. DOI: `10.1039/b910903j`.

[33] A. Buyukaksoy, V. Petrovsky, and F. Dogan. "Solid Oxide Fuel Cells with Symmetrical Pt-YSZ Electrodes Prepared by YSZ Infiltration". In: *Journal of The Electrochemical Society* 160.4 (2013), F482–F486. DOI: `10.1149/2.034306jes`.

[34] X. ChaoYang, L. XuChen, Y. Yan, W. TiZhuang, Z. ZhiMin, and Y. SuPing. "Preparation of nano-structured Pt–YSZ composite and its application in oxygen potentiometric sensor". In: *Applied Surface Science* 257.18 (2011), pp. 7952–7958. DOI: `https://doi.org/10.1016/j.apsusc.2011.04.005`.

[35] V. F. Lvovich. *Impedance spectroscopy: applications to electrochemical and dielectric phenomena*. Hoboken, New Jersey: John Wiley and Sons, 2012. ISBN: 978-0-470-62778-5.

[36] M. E. Orazem and B. Tribollet. *Electrochemical impedance spectroscopy*. 2nd ed. Hoboken, New Jersey: John Wiley and Sons, 2017. ISBN: 978-1-119-34122-2.

[37] E. Barsoukov and J. R. Macdonald, eds. *Impedance spectroscopy: theory, experiment, and applications*. 2nd ed. Hoboken, New Jersey: John Wiley and Sons, 2005. ISBN: 978-0-471-64749-2.

[38] T. Kawada, J. Suzuki, M. Sase, A. Kaimai, K. Yashiro, Y. Nigara, J. Mizusaki, K. Kawamura, and H. Yugami. "Determination of Oxygen Vacancy Concentration in a Thin Film of $La_{0.6}Sr_{0.4}CoO_3$ by an Electrochemical Method". In: *Journal of The Electrochemical Society* 149 (2002), E252–E259. DOI: `10.1149/1.1479728`.

[39] B. Hirschorn, M. E. Orazem, B. Tribollet, V. Vivier, I. Frateur, and M. Musiani. "Determination of effective capacitance and film thickness from constant-phase-element parameters". In: *Electrochimica Acta* 55.21 (Aug. 2010), pp. 6218–6227. DOI: `10.1016/j.electacta.2009.10.065`.

[40] S. B. Adler. "Electrode Kinetics of Porous Mixed-Conducting Oxygen Electrodes". In: *Journal of The Electrochemical Society* 143.11 (1996), pp. 3554–3564. DOI: `10.1149/1.1837252`.

[41] J. Jamnik and J. Maier. "Generalised equivalent circuits for mass and charge transport: chemical capacitance and its implications". In: *Physical Chemistry Chemical Physics* 3.9 (2001), pp. 1668–1678. DOI: `10.1039/b100180i`.

[42] A. Nenning, M. Gerstl, M. Bram, and A. K. Opitz. "Mechanistic Insight into Porous Electrode Impedance: An Example of Ni+YSZ Cermet Anodes". In: *ECS Transactions* 91.1 (July 10, 2019), pp. 479–490. DOI: `10.1149/09101.0479ecst`.

[43] G. Kostogloudis, G. Tsiniarakis, and C. Ftikos. "Chemical reactivity of perovskite oxide SOFC cathodes and yttria stabilized zirconia". In: *Solid State Ionics* 135.1 (2000), pp. 529–535. DOI: `https://doi.org/10.1016/S0167-2738(00)00433-1`.

[44] A. Mai, V. A. Haanappel, F. Tietz, and D. Stöver. "Ferrite-based perovskites as cathode materials for anode-supported solid oxide fuel cells: Part II. Influence of the CGO interlayer". In: *Solid State Ionics* 177.19 (2006), pp. 2103–2107. DOI: `https://doi.org/10.1016/j.ssi.2005.12.010`.

[45] L. Haar, J. S. Gallagher, and G. S. Kell. *BS/NRC steam tables*. Hemisphere Pub. Corp, 1984.

[46] S. Dierickx, J. Joos, A. Weber, and E. Ivers-Tiffée. "Advanced impedance modelling of Ni/8YSZ cermet anodes". In: *Electrochimica Acta* 265 (2018), pp. 736–750. DOI: `10.1016/j.electacta.2017.12.029`.

[47] O. Kwon and G. Choi. "Electrical conductivity of thick film YSZ". In: *Solid State Ionics* 177.35 (2006), pp. 3057–3062. DOI: `10.1016/j.ssi.2006.07.039`.

[48] K. Yashiro, S. Onuma, A. Kaimai, Y. Nigara, T. Kawada, J. Mizusaki, K. Kawamura, T. Horita, and H. Yokokawa. "Mass transport properties of $Ce_{0.9}Gd_{0.1}O_{2-\delta}$ at the surface and in the bulk". In: *Solid State Ionics* 152-153 (2002), pp. 469–476. DOI: `https://doi.org/10.1016/S0167-2738(02)00375-2`.

[49] N. I. of Standards and Technology. *NIST Chemistry WebBook*. URL: `https://webbook.nist.gov/chemistry/` (visited on 10/28/2019).

[50] S. Bishop, K. Duncan, and E. Wachsman. "Surface and bulk oxygen nonstoichiometry and bulk chemical expansion in gadolinium-doped cerium oxide". In: *Acta Materialia* 57.12 (July 2009), pp. 3596–3605. DOI: `10.1016/j.actamat.2009.04.017`.

[51] A. K. Opitz, A. Nenning, C. Rameshan, R. Rameshan, R. Blume, M. Hävecker, A. Knop-Gericke, G. Rupprechter, J. Fleig, and B. Klötzer. "Enhancing Electrochemical Water-Splitting Kinetics by Polarization-Driven Formation of Near-Surface Iron(0): An In Situ XPS Study on Perovskite-Type Electrodes". In: *Angewandte Chemie International Edition* 54.9 (Feb. 23, 2015), pp. 2628–2632. DOI: `10.1002/anie.201409527`.